ANALYSING POWER MEASUREMENTS OF COULOMB-NUCLEAR INTERFERENCE WITH POLARIZED PROTONS AT 185 GeV/c AND 200 GeV/c

by

Nural Akçurin

A thesis submitted in partial fulfillment
of the requirements for the Doctor
of Philosophy degree in Physics
in the Graduate College of
The University of Iowa

December 1990

Thesis supervisor: Associate Professor Yaşar Önel

Graduate College
The University of Iowa
Iowa City, Iowa

CERTIFICATE OF APPROVAL

PH.D. THESIS

This is to certify that the Ph.D. thesis of

Nural Akçurin

has been approved by the Examining Committee for the thesis requirement for the Doctor of Philosophy degree in Physics at the December 1990 graduation.

Thesis committee: _____
Thesis supervisor

_____
Member

_____
Member

_____
Member

_____
Member

Җиктереп пар ат, Казанга туп-туры киттем карап;
Чаптыра атларны кучер, суккалап та тарткалап.

Кич иде. Шатлык белән нурлар чәчеп ай ялтырый;
Искән әкрен җил белән яфрак, агачлар калтырый.

Һәр тараф тын. Уй миңа тик әллә ни жырлый, укый;
Нәрсәдәндер күз эленгән һәм тәмам баскан йокы.

Бер заман ачсам күзем, бер төрле яп-ят кыр күрәм;
Аһ, бу нинди айрылу? Гомремдә бер тапкыр күрәм.

Сау бул инде, хуш, бәхил бул, и минем торган җирем,
Мин болай, шулай итәм дип, төрле уй корган җирем.

Хуш, гомер иткән шәһәр! инде еракта калдыгыз;
Аһ! таныш йортлар, тәмам күздән дә сез югалдыгыз.

Эч поша, яна йөрәк, хәсрәт әчендә, уйда мин;
Ичмасам иптәш тә юк ич, тик икәү без: уй да мин.

Аһ, гөнаһым шомлыгы, бу кучеры бик тын тагын,
Җырламыйдыр бер матурның балдагын йә калфагын!

Әллә нәрсәм юк кеби; бер нәрсә юк, бер нәрсә ким;
Бар да бар, тик юк туганнар, мин ятим монда, ятим.

Бер тавыш килде колакка, яңгырады бер заман:
«Тор, шәкерт! Җиттек Казанга, алдымызда бит Казан».

Бу тавыш бик ачты күңлем, шатлыгымнан жан яна;
«Әйдә чап, кучер, Казанга! Атларың ку: на! на-на!»

Әйтә иртәнге намазга бик матур, моңлы азан;
И Казан! дәртле Казан! моңлы Казан! нурлы Казан!

ACKNOWLEDGMENTS

The E-704 collaboration was a multinational, multitalented and multipurpose experiment which provided me with an intense yet fruitful environment in which to explore, learn, and enjoy physics. Several people contributed to the work reported here. My advisor and friend, Yaşar Önel, made it possible for me to be a part of this project. Aldo Penzo, who possesses uncommon expertise and enthusiasm, was a constant source of inspiration and strength. Ludwig van Rossum provided the essential insight and experience needed for this experiment. Alain de Lesquen wrote the first analysis codes and was always there whenever I sought his help. Attilio Villari, George Brystricky, Franz Lehar, Gianni Pauletta, Anna-Maria Zanetti, Aaron Michalowicz, Keichi Kuroda, Gabriele Salvato, Fred Luehring and Dave Grosnick were all essential to the success of this measurement.

I owe many thanks also to Aki Yokosawa and all of the E-704 collaborators for their admirable efforts.

I would like to express my thanks to Larry Schroeder for allowing me infinite amount of computer time and disk space, to John Birkbeck for drawing some of the figures, to Jane Nachtman for helping with the analysis and to Alice Shank for advising me about the format of this thesis.

Without the support and understanding of my wife, Leslie, this thesis would not have become a reality. In that sense, this is as much a result of her sacrifices as of mine. I thank her deeply for her help.

My parents lovingly supported me in my work, even from the other side of the ocean, a challenge unto itself that can only be accomplished by mothers and fathers. There is no word that can express my gratitude for them.

ABSTRACT

The analysing power A_N of proton-proton scattering in the Coulomb-nuclear interference region has been measured using the 185 GeV/c and 200 GeV/c Fermilab polarized-proton beams. In the region of 3.0×10^{-3} to 5.0×10^{-2} $(\mathrm{GeV/c})^2$ four-momentum-transfer squared, the results are found to be consistent with theoretical prediction within statistical uncertainties. A polarimeter based on the interference between the hadronic non-flip amplitude and the electromagnetic spin-flip amplitude is shown to be promising at high energies due to the independence of the process from the beam energy. In addition, the contribution of the hadronic spin-flip amplitude is investigated.

TABLE OF CONTENTS

	Page
LIST OF TABLES	vii
LIST OF FIGURES	viii
CHAPTER	
I. INTRODUCTION	1
II. THEORY OF TWO-NUCLEON INTERACTION AND COULOMB-NUCLEAR INTERFERENCE	6
Introduction	6
The Spin-Scattering Matrix M	12
Helicity Representation	14
Coulomb-Nuclear Interference	17
III. POLARIZED PARTICLE BEAMS	27
Primary-Proton Beam	28
Polarized Proton Production	29
Polarized (Secondary) Proton Beam	31
Polarized Proton Beam Optics	32
Spin-Rotating Magnets (Snake Magnets)	34
Beam Tagging System	35
IV. EXPERIMENTAL SETUP	50
CNI Target (Trans-Stilbene)	50
Light Collection System of Targets	56
Target Veto Counters	57
Multi-Wire Proportional Chambers (MWPC)	57
Analysing Magnet BM-109	58
Gray Code Hodoscope	58
Data Acquisition System and Trigger	60
V. KINEMATICS OF COULOMB-NUCLEAR INTERFERENCE AND EXPERIMENTAL CONSIDERATIONS	76
Kinematics of Elastic *pp* Scattering at Small Angles	76
Experimental Method	80

Chapter Page

VI. ANALYSIS, RESULTS AND DISCUSSION 88

Data Analysis 88
Vertex Reconstruction 89
Selection of *pp* Elastic Events 90
Calculation of Asymmetries 93
Results and Discussions 97
Run Summary 100

REFERENCES 121

LIST OF TABLES

Table		Page
2.1.	The behavior of the rotation-invariants under the space reflection, time reversal and the Pauli exclusion transformations.	22
4.1.	Dimensions and locations of each target along the beam-line.	63
4.2.	The reduction in trigger rate as measured for individual veto counters.	63
4.3.	List of the multi-wire proportional chambers used for this measurement.	64
4.4.	Possible hit patterns and their binary equivalents for the GC for a given bin.	66

LIST OF FIGURES

Figure		Page
2.1.	Coordinate system in the center of mass frame.	23
2.2.	Schematic representation of left and right scattered particles.	24
2.3.	Plots of the differential cross-section and analysing power as a function of $\|t\|$ for the CNI process.	25
2.4	The t-dependence of pp elastic polarization in the Coulomb-nuclear interference region versus the pomeron anomalous moment, M [Kope89].	26
3.1.	Diagram of the MP primary beam-line.	37
3.2.	Λ hyperons are produced by the incident 800 GeV/c protons on a beryllium target.	38
3.3.	Correlation between the average proton polarization and the horizontal position at the intermediate focus for a 185 GeV/c beam.	39
3.4.	The calculated polarized-proton and -antiproton beam intensity per spill as a function of the beam momentum.	40
3.5.	The side view of the secondary beam elements.	41
3.6.	Side view of the production target and the primary beam dump area.	42
3.7.	Beam optics of the polarized proton beam-line.	43
3.8.	Schematic representation of the spin rotation from S (horizontal) to N (vertical) direction through the snake magnets.	44
3.9.	Schematic representation of the spin rotation from the S (horizontal) to the L (longitudinal) direction through the snake magnets.	45
3.10.	Conceptual layout of the beam tagging hodoscopes.	46
3.11.	Distribution of the raw-hit patterns in the ten beam hodoscopes.	47

Figure Page

3.12. Momentum distribution of the 185 GeV/c polarized proton beam as measured by the tagging system. 48

3.13. Polarization distribution of protons measured by the beam tagging system. 49

4.1. Top-view layout of the CNI polarimeter. 67

4.2. The fluorescence and PSD characteristics of trans-stilbene. 68

4.3. Atomic stopping numbers for hydrogen and carbon, and relative light outputs of trans-stilbene. 69

4.4. Cross-section of an individual target assembly, (a) aluminum disk where the target is attached, (b) bakelite tube, (c) lucite rod from which the target is suspended, (d) trans-stilbene target, (e) conical guide, (f) type XP2020 PMT, (g) CERN type base and (h) target table. 70

4.5. Veto counters around the CNI target assembly. 71

4.6. The magnetic field strength of BM-109 in the central region of the magnet gap. 72

4.7. Cross-section of one of the hodoscopes of the GC. 73

4.8. Simplified PSD trigger. 74

4.9. Schematics of the CNI trigger for the downstream part of the electronics. 75

5.1. Schematic representation of small angle elastic scattering before and after the impact. 84

5.2. The kinetic energy of the recoil proton as a function of four-momentum transfer for elastic small angle scattering. 85

5.3. The scattering angle θ_s of the forward proton as a function of four-momentum transfer for elastic small angle scattering at 200 GeV/c. . 86

5.4. The recoil angle θ_r of the target proton as a function of four-momentum transfer for elastic small angle scattering at 200 GeV/c. . 87

6.1. The general structure of the CNI off-line analysis code. 103

Figure Page

6.2. Z-vertex reconstruction of all events. 104

6.3. Z-vertex distribution of individual targets. 105

6.4. The superimposed z-vertex distribution of individual targets. 106

6.5. The correlation between the four-momentum transfer squared $|t|$ and the ADC slow component for target 3. 107

6.6. $(Z_{reconstructed} - Z_{measured}) \tan \theta_s$ distribution for each target. 108

6.7. The ADC slow component spectrum for target 6 as a function of t binning. 109

6.8. ADC slow component distribution of events for five different $|t|$-bins for target 3 and 4. 110

6.9. Linear fits of seven gaussian centroids for each target. 111

6.10. $(t_{measured} - t_{expected})$ distribution for each target. 112

6.11. The *butterfly* cut as observed at GC. 113

6.12. The analysing power, A_N, for pp elastic scattering in the Coulomb-nuclear interference region as a function of $|t|$. 114

6.13. $(t_{measured} - t_{expected})$ distributions as a function of ADC bins for target one. 115

6.14. t distribution for all of the events before and after the cuts. 116

6.15. The compilation of polarization data for pp elastic scattering as a function of $|t|$ up to 1.0 $(\mathrm{GeV/c})^2$ 117

6.16. The raw *space* asymmetry for each target as a function of t. 118

6.17. The raw *snake* asymmetry for each target as a function of t. 119

6.18. The raw *tagging* asymmetry for each target as a function of t. 120

CHAPTER I

INTRODUCTION

The idea of spin in quantum mechanics has no direct analog in classical physics. Pauli first suggested in 1925 that an electron has an additional quantum number which can take on only two values. He expected that this quantum number would be associated with the time coordinate in a relativistic theory. However, later in the same year, Gouldsmit and Uhlenbeck announced that this number was associated with the intrinsic angular momentum of an electron, called spin. This made an explanation of the fine structure of atomic spectra and the periodic table possible. Soon after this discovery, the quantum mechanical understanding of the Stern-Gerlach experiment also became apparent.

For about thirty years after the discovery of spin, study of this particular phenomenon was confined mainly to atomic and molecular physics. With the advent of particle beams, however, spin effects became one of the major areas of investigation in high energy particle physics. To this day it remains an intriguing and a surprising branch of study. Originally it was quite erroneously assumed that spin effects at higher energies would become negligible. Recent data from CERN [Ashm88] and SLAC [Algu76, Baum83] show that just the opposite is true. EMC (European Muon Collaboration) data on the spin-dependent proton structure function suggest that very little of the proton spin is due to the helicities of the constituent quarks. In non-relativistic quark models the bound state of three quarks constitute a proton and the algebraic sum of the quarks' spin gives rise to the spin of the proton. According to QCD (Quantum Chromodynamics) and

deep inelastic scattering data, the structure fuction of the proton is considerably different. The proton contains an infinite number of partons, i.e. quarks and gluons, which can all contribute to the proton's spin through their intrinsic spins or via their orbital angular momentum. If we write the sum rule as

$$\frac{1}{2}\sum_q \Delta q + \Delta G + \langle L_z \rangle = \frac{1}{2}, \tag{1.1}$$

then the quark and gluon helicities, Δq and $\Delta(G)$, are respectively defined as

$$\Delta q = \int_0^1 \Delta q(x) = \int_0^1 dx[q_\uparrow(x) + \bar{q}_\uparrow(x) - q_\downarrow(x) - \bar{q}_\downarrow(x)] \tag{1.2}$$

$$\Delta G = \int_0^1 \Delta G(x) = \int_0^1 dx[G_\uparrow(x) - G_\downarrow(x)]. \tag{1.3}$$

Where does the spin of the proton come from? There are many different views about this in particle physics literature. These vary from speculations that the perturbative QCD, EMC data and interpretation of the quark model are wrong, to more detailed arguments on the sum rules and scaling laws. Leaving these arguments aside for the time being, we will concentrate on a simpler yet important aspect of an experimental measurement – beam polarization as nature presents it.

In the following chapters one of the most essential and fundamental subjects of spin physics is studied, namely the measurement of the spin of a proton using a polarimeter based on the interference of Coulomb and nuclear forces in the low momentum transfer region, $\sim 2\times10^{-3}$ to $\sim 5\times10^{-2}$ $(\mathrm{GeV/c})^2$. This is an essential part of spin physics because it defines the initial state of the reactions and monitors the polarization of the beam for

other polarization measurements. This is also fundamental because it not only measures the polarization of the beam, but studies the interactions between electromagnetic and hadronic forces from the view of polarization phenomena.

Historically, the polarization measurements started with the polarized beams. Polarimeters for the lower polarized beam momenta, up to 12 GeV/c, based on pp elastic scattering, are reviewed in detail in spin physics literature [Robe78]. At higher beam momenta [Kuro82], however, such conventional ideas of measuring polarization do not work since the polarization (or analysing power) is very small at small $|t| \leq 0.2$ (GeV/c)^2, and the cross-section is too little at higher $|t| \geq 1.4$ (GeV/c)^2. Therefore, at Fermilab energies one needs to have a different mechanism for polarization measurement. The principal criteria for high energy polarimeters are

1. large analysing power A known to good accuracy ΔA,
2. large cross-section σ,
3. weak dependence of A on the beam momentum,
4. simplicity and reliability of setup.

The beam polarization, P_b, is measured via asymmetry in the number events, say particles with spins up and down, $N\uparrow$ and $N\downarrow$, respectively. The asymmetry ϵ is conventionally defined as

$$\epsilon = \frac{N\uparrow - N\downarrow}{N\uparrow + N\downarrow} = AP_b. \tag{1.4}$$

Then the accuracy of the beam polarization measurement, ΔP_b, is proportional to $1/A\sqrt{\sigma}$ and this, in turn, provides a figure of merit for polarimeters in general. We shall define the figure of merit as $A^2\sigma$.

In inclusive hadronic reactions, large asymmetries have been observed in the production of pions at BNL, CERN, Serpukhov and at our experiment E-704 at FNAL [Klem76, Apok89, Anti80, Bonne88]. For $pp \rightarrow \pi^{\pm}X$ at 6 and 12 GeV/c, π^- inclusive production asymmetry is about $25-35\%$ at small p_t, large x_F and in this momentum range the asymmetry is practically energy independent. For $pp \rightarrow \pi^0 X$ at $x_F = 0$ and $p_t \sim 2.0$ GeV/c at beam momenta of 24 GeV/c, asymmetry is also large: $\sim 25\%$. New measurements at E-704 (FNAL) indicate that the π^0 inclusive production asymmetry at $x_t \geq 0.4$ increases up to $25-35\%$, and does not depend on energy in the range of 13 to 200 GeV. These reactions, with factors of merit up to $\sim 1\,\mu$b, are potentially good and simple polarimeters. If one uses an internal hydrogen jet target, the inclusive π^0 production mechanism at $x_F = 0$ could be a choice polarimeter for accelerated polarized protons. One of the major drawbacks of the polarimeters based on the aforementioned mechanisms is that they are *relative* polarimeters and need to be calibrated against an *absolute* polarimeter.

One of the requirements for an ideal polarimeter (1) makes it imperative to search for a process that is electromagnetic (QED) in nature and thus calculable to a high degree of accuracy in contrast to strong interactions (QCD). One such process is Coulomb diffractive dissociation of incident proton into a πN system in the Coulomb field of nuclei. If one considers the reaction $pA \rightarrow \pi^0 pA$, it looks like a low energy photoproduction, $\gamma p \rightarrow \pi^0 p$, when viewed from the rest frame of the incident proton. A polarimeter based on this so-called Primakoff effect [Prim51] was constructed during the 1988-89 fixed target period at MP beamline at FNAL, and it measured the beam polarization to be $40 \pm 12\%$, consistent with the design value of the beamline [Yosh88, Care90]. The Primakoff polarimeter is an absolute polarimeter and it has a large factor of merit, $\sim 20\,\mu$b. While it is suitable for

fixed target experiments, its implementation for collider-type physics is difficult because of the heavy targets required.

The Coulomb-Nuclear interference (CNI) polarimeter is the subject of this thesis and it will be discussed in detail in the following chapters. In the next chapter, a general discussion of two-nucleon elastic scattering is presented. The phenomenon of Coulomb-Nuclear interference in *pp* elastic collisions is also treated there in some detail from a theoretical point of view. Chapter III is dedicated to the MP9 (FNAL) polarized proton beam-line. The production of polarized protons (anti-protons) from Λ ($\bar{\Lambda}$) hyperon decay, and the manipulation of proton spin with the Snake magnet are explained. Chapter IV contains descriptions of the experimental set-up and individual components, e.g. targets, vetos, hodoscopes, muti-wire proportional chambers (MWPC), etc. The following chapter, Chapter V, is concerned with the kinematics of elastic *pp* scattering at small angles and the essential criteria that must be observed for the measurement of asymmetries. Detailed discussions of critical experimental parameters are developed and are applied to the E-704 CNI polarimeter in this chapter. Chapter VI summarizes the procedure of analysis of polarimeter data and the obtained results for the CNI run in 1990 at FNAL.

CHAPTER II

THEORY OF TWO-NUCLEON INTERACTION AND COULOMB-NUCLEAR INTERFERENCE

There are a number of published works on the formalism of nucleon-nucleon scattering [Hosh68, Byst78, Mora68] and more specifically on the Coulomb-nuclear interference phenomena. The first pioneering work was published in 1948 by Schwinger [Schw48]. He pointed out that the polarization of fast neutrons was possible by the spin-orbit interaction arising from the motion of neutron magnetic moment in the nuclear Coulomb field. Regardless of the small magnitude of this interaction, complete ($\sim$ 100%) polarization was shown to be possible in the case of fast neutrons at very small scattering angles due to the long-range nature of the electromagnetic interactions. Several authors [Kope74, Butt78, Beh58, Loch67, Solo66, Garr56, West68] also showed that a small but considerable asymmetry was expected in $p \uparrow p$ elastic scattering at small four-momentum squared $|t| \approx 0.003$ (GeV/c)^2 which arises from the interference between the hadronic non-flip amplitude and the electromagnetic spin-flip amplitude. In this chapter, theoretical aspects of two-nucleon scattering and the Coulomb-nuclear interferenece phenomena are discussed in depth.

Introduction

The scattering of two nucleons can be described by scattering amplitude in the form of a matrix in spin space [Wolf52]. In this formalism, the scattering state wave function is written as a vector,

$$\Psi^{(n)} = e^{i\mathbf{k}_i\cdot\mathbf{r}}\chi^{(n)} + M\chi^{(n)}\frac{e^{ikr}}{r}. \tag{2.1}$$

$\chi^{(n)}$ is a four-component initial state column vector in one of the possible spin states n, and M is a 4×4 spin-scattering matrix of the two-nucleon system which acts on $\chi^{(n)}$. M depends on the initial and final momenta in the center of mass system, $\mathbf{p}_i$ and $\mathbf{p}_f$, respectively, and on the Pauli spin operators of the two nucleons, $\sigma^{(1)}$ and $\sigma^{(2)}$. M serves essentially as the scattering amplitude $f(\theta, \phi)$ for the process. Introduction of the unit vectors (Equation 2.2) that define a rectilinear Cartesian coordinate system provides a physical reference frame.

$$\hat{\mathbf{l}} = \frac{\mathbf{p}_i + \mathbf{p}_f}{|\mathbf{p}_i + \mathbf{p}_f|}, \qquad \hat{\mathbf{m}} = \frac{\mathbf{p}_f - \mathbf{p}_i}{|\mathbf{p}_f - \mathbf{p}_i|}, \qquad \hat{\mathbf{n}} = \frac{\mathbf{p}_i \times \mathbf{p}_f}{|\mathbf{p}_i \times \mathbf{p}_f|}. \tag{2.2}$$

If the scattering is considered in the non-relativistic regime (Figure 2.1), the incident nucleon scatters in $\hat{\mathbf{l}}$ and the target nucleon recoils in $-\hat{\mathbf{m}}$ direction in the laboratory frame. The unit vector $\hat{\mathbf{n}}$ is perpendicular to the scattering plane.

In general, any polarization state of two spin-1/2 particles can be described as a mixture of pure spin states. The ultimate problem, however, is finding out the final polarization state and the intensity as a function of scattering angle if the inital polarization state is defined. The final spin expectation values can be represented as $< \sigma_\alpha{}^{(1)}\sigma_\beta{}^{(2)} >_{final}$, $(\alpha, \beta) = 0, 1, 2, 3$, where $\sigma_0 = 1$ corresponds to a measurement where the spin component is unknown. A polarization state can thus be specified entirely by the average values of 16 observables associated with the spins of the two particles. This can be shown as follows; consider a density matrix ρ for an incoherent mixture of pure spin states, e.g. particle beams,

$$\rho_{ij} = \sum_n P_n \chi_i{}^{(n)} \chi_j{}^{(n)\dagger} \tag{2.3}$$

where P_n is the relative probability of finding the system in state $\chi^{(n)}$, and $\chi^{(n)\dagger}$ is the adjoint row vector. The subscripts i and j correspond to the respective components of the state vectors. The summation implies the sum over the spin states of individual beam particles. Thus, the average value $< S^\mu >$ of any spin operator S^μ can be calculated.

$$\begin{aligned} < S^\mu > &= \frac{\sum_n P_n < \chi^{(n)} | S^\mu | \chi^{(n)} >}{\sum_{\alpha n} P_n < \chi^{(n)} | \chi^{(n)} >} \\ &= \frac{\sum_n \sum_{i,j} P_n \chi_i{}^{(n)\dagger} S_{ij}{}^\mu \chi_j{}^{(n)}}{\sum_n \sum_i P_n \chi_i{}^{(n)\dagger} \chi_i{}^{(n)}} \\ &= \frac{Tr(\rho S^\mu)}{Tr(\rho)}. \end{aligned} \tag{2.4}$$

The density matrix ρ is a Hermitian 4×4 matrix and can be fixed by providing 16 real numbers which may be average values of a complete set of 16 Hermitian operators S^μ in spin space with $S^\mu \equiv \sigma_\alpha{}^{(1)} \sigma_\beta{}^{(2)}, \mu = (\alpha, \beta) = 1, 2, ..., 16$. A set of operators is called complete if they satisfy the orthagonality condition, i.e.,

$$Tr(S^\mu S^\nu) = 4\delta_{\mu\nu}. \tag{2.5}$$

These operators, for instance, $1, \sigma_{1x}, \sigma_{1y}, \sigma_{1z}, \sigma_{2x}, \sigma_{2y}, \sigma_{2z}$ and the 9 products of one of the Pauli spin operators for particle 1 with those of particle 2, form such a set of operators. Therefore, any matrix can be expressed linearly in S^μ, including the density matrix ρ,

$$\rho = \frac{1}{4} \sum_\mu S^\mu Tr(\rho S^\mu) = \frac{1}{4} Tr(\rho) \sum_\mu < S^\mu > S^\mu. \tag{2.6}$$

The ultimate aim, as mentioned earlier, is to produce a relationship between incoming and outgoing polarization states by providing averages $< S^\mu >_{final}$ in terms of $< S^\mu >_{initial}$. By the definition of the spin-scattering matrix M, the density matrix ρ_f for the final polarization state at any angle can be written as

$$\rho_f = \sum_n P_{ni} M \chi_i{}^{(n)} \chi_i{}^{(n)\dagger} M^\dagger = M \rho_i M^\dagger, \tag{2.7}$$

and equation (2.4) in this case becomes

$$< S^\mu >_f = \frac{Tr(M \rho_i M^\dagger S^\mu)}{Tr(M \rho_i M^\dagger)}. \tag{2.8}$$

The initial polarization state is completely defined by the expectation value $< S^\mu >_i$ of S^μ as defined by equation (2.4) and can be expressed as

$$\begin{aligned} \rho_i &= \sum_{i=1}^{16} a_\mu S^\mu \\ a_\mu &= \frac{Tr(\rho_i S^\mu)}{Tr(S^\mu S^\mu)} \\ &= \frac{1}{4} Tr(\rho_i) < S^\mu >_i \end{aligned} \tag{2.9}$$

By substituting the above equation into equation (2.8), we have the sought relation between the incident and the final polarization states.

$$I < S^\mu >_f = \frac{1}{4} \sum_\nu < S^\nu >_i Tr(M S^\nu M^\dagger S^\mu) \tag{2.10}$$

where

$$
\begin{aligned}
I &= \frac{1}{4}\sum_{\nu=1}^{16} < S^{\nu} >_i Tr(MS^{\nu}M^{\dagger}) \\
&= \frac{Tr(M\rho_i M^{\dagger})}{Tr(\rho_i)} \\
&= \frac{Tr(\rho_f)}{Tr(\rho_i)}
\end{aligned}
\tag{2.11}
$$

and I is the differential cross-section at a given angle.

In the case of a polarized beam and an unpolarized target – the situation at hand for the CNI polarimeter – we have the following:

$$
I = \frac{1}{4}Tr(MM^{\dagger}) + \frac{1}{4} < \sigma_1 >_i Tr(M\sigma_1 M^{\dagger}) \tag{2.12}
$$

where the first term on the right is the scattering cross-section for the unpolarized beam and the second term is the contribution to the cross-section due to the initial beam polarization.

The following relation holds on the basis of time invariance of matrix M, as will be shown in the next section.

$$
Tr(M\sigma^{(i)}M^{\dagger}) = Tr(MM^{\dagger}\sigma^{(i)}), \qquad i = (1,2) \tag{2.13}
$$

Using this relation, equation (2.12) reduces to

$$
I = I_o(1 + P_i P \cos\Phi), \tag{2.14}
$$

where $P_i = |< \sigma^{(i)} >_i|$ is the polarization of the incident particles and P is the analysing power of the target. Analysing power is a dynamical parameter, $-1 \leq P \leq 1$, for a given

scattering which depends on the energy and the scattering angle θ. In more physical terms, it is a measure of how much a given reaction is spin-dependent, or how well a target can analyse the incident beam polarization. Φ is the angle between $< \sigma >_i$ and $\hat{\mathbf{n}}$ (see figure 2.2). Equation (2.14) is the principal relation in polarization analysis. In CNI, or any polarimeter, the purpose is to measure the polarization of the beam, P_i. If we consider that the initial polarization $< \sigma >_i$ is in $\hat{\mathbf{n}}$ direction, figure 2.2 shows the typical scattering geometry for the left and right scattered particles. In a special case, if the incident particle is scattered on the xy-plane due left(right) with respect to $\mathbf{p}_i$, the angle Φ between $< \sigma >_i$ and $\hat{\mathbf{n}}$ is equal to $0(\pi)$. Therefore the equation (2.14) simplifies to

$$\begin{aligned} \sigma_L &\equiv I(\theta, \phi) = I_o(\theta)(1 + P_i P) \\ \sigma_R &\equiv I(\theta, \phi + \pi) = I_o(\theta)(1 - P_i P) \end{aligned} \tag{2.15}$$

where (θ, ϕ) is in the center of mass frame with the polar axis along $\mathbf{p}_i$. Asymmetry, ϵ, then, in two-particle elastic scattering can be defined as

$$\epsilon = \frac{\sigma_L - \sigma_R}{\sigma_L + \sigma_R} = P_i P. \tag{2.16}$$

If the analysing power P is known then it is possible to calculate the beam polarization P_i from the measured asymmetry, ϵ. Note that the analysing power is conventionally represented by A as previously discussed in Chapter I (see equation (1.4)). From now on, this convention will be adhered to.

The Spin-Scattering Matrix M

The most general form of spin-scattering matrix M can be written as

$$\begin{aligned} M = a + c\,(\sigma^{(1)} + \sigma^{(2)}) \cdot \hat{\mathbf{n}} + m\,(\sigma^{(1)} \cdot \hat{\mathbf{n}})(\sigma^{(2)} \cdot \hat{\mathbf{n}}) \\ + g\,\{(\sigma^{(1)} \cdot \hat{\mathbf{l}})(\sigma^{(2)} \cdot \hat{\mathbf{l}}) + (\sigma^{(1)} \cdot \hat{\mathbf{m}})(\sigma^{(2)} \cdot \hat{\mathbf{m}})\} \\ + h\,\{(\sigma^{(1)} \cdot \hat{\mathbf{l}})(\sigma^{(2)} \cdot \hat{\mathbf{l}}) - (\sigma^{(1)} \cdot \hat{\mathbf{m}})(\sigma^{(2)} \cdot \hat{\mathbf{m}})\}. \end{aligned} \tag{2.17}$$

The coefficients a, c, m (not to be confused by $\hat{\mathbf{m}}$), g and h are complex numbers and functions of the energy and scattering angle.

The matrix M is a scalar and thus invariant under space rotations, reflections and time reversal. Rotation invariance or conservation of angular momentum requires that the resulting expression be a scalar. There are 17 such combinations one can construct with the spin and coordinate vectors (see Table 2.1). Only 16 of these 17 combinations are independent since $\sigma^{(1)} \cdot \sigma^{(2)}$ can be expressed in terms of the others.

Space reflection or conservation of parity demands that the expression remain unchanged if the vectors change sign and the axial vectors do not. $\hat{\mathbf{l}}$ and $\hat{\mathbf{m}}$ are vectors but $\hat{\mathbf{n}}$ is an axial vector since it is a cross-product. Similarly the spin vectors are axial because they can be thought of as cross-products of coordinate and momentum vectors. So the transformation for space reflection invariance can be represented as

$$\sigma \to \sigma, \quad \hat{\mathbf{n}} \to \hat{\mathbf{n}}, \quad \hat{\mathbf{l}} \to -\hat{\mathbf{l}}, \quad \hat{\mathbf{m}} \to -\hat{\mathbf{m}}. \tag{2.18}$$

Time invariance requires that if the direction of time is reversed the relevant expressions remain unchanged. This means that the signs of momenta change due to velocity. Consequently the sign change in momenta changes the signs of spin vectors. The time invariance transformation is then

$$\sigma \to -\sigma, \quad \hat{\mathbf{n}} \to -\hat{\mathbf{n}}, \quad \hat{\mathbf{l}} \to -\hat{\mathbf{l}}, \quad \hat{\mathbf{m}} \to \hat{\mathbf{m}}. \tag{2.19}$$

If we have identical particles in the scattering process, as we do in CNI, then the Pauli exclusion principle requires that the expressions remain unaltered under the interchange of particles (1) and (2). This transformation only effects the spin vectors, i.e.,

$$\sigma^{(1)} \leftrightarrow \sigma^{(2)}. \tag{2.20}$$

From Table 2.1 we observe that after the conservation requirements the number of independent expressions reduces from 16 to 6. The Pauli exclusion principle eliminates one more. For pp scattering the final number of expressions is five, whereas for np scattering it is 6. If charge independence (pp vs np) is required from the matrix M, then M has to be considered in isospin space. This makes it possible to describe both of these processes with only five amplitudes, i.e. equation (2.17). In this case, the spin-scattering matrix is represented as the sum of two isospin states.

$$M = M_0 P_0 + M_1 P_1 \tag{2.21}$$

P_T $(T = 0, 1)$ is the projection operator for total isospin T states such that

$$P_0 = \frac{1}{4}\{(1 - (\tau^{(1)} \cdot \tau^{(2)})\}, \quad P_1 = \frac{1}{4}\{(3 + (\tau^{(1)} \cdot \tau^{(2)})\}. \tag{2.22}$$

In equation (2.21) M_0 and M_1 are expressed in the same fashion as in equation (2.17). For different combinations of nucleon-nucleon scattering, the matrix M takes the following forms:

$$
\begin{aligned}
M(pp \rightarrow pp) &= M(nn \rightarrow nn) = M_1 \\
M(np \rightarrow np) &= \frac{1}{2}(M_1 + M_0) \\
M(np \rightarrow pn) &= \frac{1}{2}(M_1 - M_0)
\end{aligned}
\tag{2.23}
$$

The arguments presented thus far apply to non-relativistic processes. It can be shown [Stap56] that if relativistic corrections are added the formalism for the most part remains valid.

Helicity Representation

Helicity representation is perhaps the most common formalism employed in the study of polarization phenomena in high energy physics today. What follows is a brief presentation of this formalism which is used extensively in the next section. In the helicity representation of scattering processes, the states are identified with the component of the spin vector along the particle's momentum [Jaco59]. The helicity quantum number λ, helicity for short, is $+\frac{1}{2}(-\frac{1}{2})$ if the spin vector is parallel (anti-parallel) to the direction of motion of the nucleon. The elements of the spin-scattering matrix M are written by

$$
< \lambda_1{}'\lambda_2{}'|M|\lambda_1\lambda_2 > \tag{2.24}
$$

and they are called helicity amplitudes. $\lambda_1{}'$ and $\lambda_2{}'$ are the helicities of the outgoing nucleons and λ_1 and λ_2 are those of incoming ones. The corresponding five amplitudes (see equation (2.17)) in the helicity representation are expressed as follows:

$$
\begin{aligned}
\phi_1 &= <+, \quad +|M|+, \quad +>, \quad \text{non-flip} \\
\phi_2 &= <+, \quad +|M|-, \quad ->, \quad \text{double-flip} \\
\phi_3 &= <+, \quad -|M|+, \quad ->, \quad \text{non-flip} \\
\phi_4 &= <+, \quad -|M|-, \quad +>, \quad \text{double-flip} \\
\phi_5 &= <+, \quad +|M|+, \quad ->, \quad \text{single-flip}
\end{aligned}
\tag{2.25}
$$

where $+ = +\frac{1}{2}$ and $- = -\frac{1}{2}$. The amplitudes ϕ_i are related to the coefficients a, c, m, g and h of the M matrix. If we take the z-axis along the direction of the incident nucleons, the initial helicity states ${\chi_{\lambda_1}}^{(1)}$ and ${\chi_{\lambda_2}}^{(2)}$ for each nucleon can be written as

$$
{\chi_{1/2}}^{(1)} = {\chi_{-1/2}}^{(2)} = \begin{pmatrix} 1 \\ 0 \end{pmatrix}, \quad {\chi_{-1/2}}^{(1)} = {\chi_{1/2}}^{(2)} = \begin{pmatrix} 0 \\ 1 \end{pmatrix} \tag{2.26}
$$

and the final helicity states are

$$
\begin{aligned}
{\chi_{1/2}}^{(1)} = {\chi_{-1/2}}^{(2)} &= \begin{pmatrix} \cos(\theta/2) \\ \sin(\theta/2) \end{pmatrix} \\
{\chi_{-1/2}}^{(1)} = {\chi_{1/2}}^{(2)} &= \begin{pmatrix} -\sin(\theta/2) \\ \cos(\theta/2) \end{pmatrix}.
\end{aligned}
\tag{2.27}
$$

The angle θ is the scattering angle in the center of mass frame (Figure 2.1). The amplitudes are calculated by using equation (2.17), and the coordinate-defining unit vectors are as indicated in equation (2.28) below.

$$
\hat{\mathbf{n}} = (0,1,0), \quad \hat{\mathbf{m}} = (\cos(\theta/2), 0, -\sin(\theta/2)), \quad \hat{\mathbf{l}} = (\sin(\theta/2), 0, \cos(\theta/2)) \tag{2.28}
$$

The result for each of the helicity amplitudes is

$$
\begin{aligned}
\phi_1 - \phi_2 &= a - m - 2g \\
\phi_1 + \phi_2 &= (a+m)\cos(\theta) + 2ic\sin(\theta) - 2h \\
\phi_3 + \phi_4 &= a - m + 2g \\
\phi_3 - \phi_4 &= (a+m)\cos(\theta) + 2ic\sin(\theta) + 2h \\
\phi_5 &= -\frac{1}{2}(a+m)\sin(\theta) + ic\cos(\theta).
\end{aligned}
\tag{2.29}
$$

The inverse relations can also be calculated, i.e., the coefficients a, c, m, g and h in terms of ϕ_i (see [Hosh68]). These helicity amplitudes are related to the physical observables in the following way,

1. spin-averaged total cross-section,

$$
\begin{aligned}
\sigma^{TOT} &= \frac{2\pi}{k}\, Im\,\{\phi_1(0) + \phi_3(0)\} \\
&= \frac{1}{2}\{\sigma^{TOT}(\rightarrow,\leftarrow) + 2\sigma^{TOT}(\rightarrow,\rightarrow)\}
\end{aligned}
\tag{2.30}
$$

2. difference between total cross-section for anti-parallel and parallel longitudinal spin states,

$$
\begin{aligned}
\Delta\sigma_L &= \frac{4\pi}{k}\, Im\,\{\phi_1(0) - \phi_3(0)\} \\
&= \{\sigma^{TOT}(\rightarrow,\leftarrow) - \sigma^{TOT}(\rightarrow,\rightarrow)\}
\end{aligned}
\tag{2.31}
$$

3. difference between total cross-section for anti-parallel and parallel transverse spin states,

$$
\begin{aligned}
\Delta\sigma_T &= -\frac{4\pi}{k}\, Im\,\{\phi_2(0)\} \\
&= \{\sigma^{TOT}(\uparrow,\downarrow) - \sigma^{TOT}(\uparrow,\uparrow)\}
\end{aligned}
\tag{2.32}
$$

4. asymmetry parameter, A_N, in pp elastic collisions,

$$A_N \frac{d\sigma}{dt} = -Im\{(\phi_1 + \phi_2 + \phi_3 - \phi_4)\,\phi_5{}^*\}. \tag{2.33}$$

where $\frac{d\sigma}{dt}$ is the spin-averaged differential cross-section for pp scattering. In terms of the helicity amplitudes it is written as

$$\frac{d\sigma}{dt} = \frac{\pi}{2k^2}\left[|\phi_1|^2 + |\phi_2|^2 + |\phi_3|^2 + |\phi_4|^2 + 4|\phi_5|^2\right]. \tag{2.34}$$

A_N at small-angle elastic $p \uparrow p$ scattering is about ~4.6% at $|t| \sim 0.003\,(\mathrm{GeV/c})^2$ and arises from the interference between the hadronic non-flip amplitude and the electromagnetic spin-flip amplidute. This phenomenon is discussed below.

Coulomb-Nuclear Interference

If the higher order electromagnetic terms are neglected and under the hypothesis of the additivity of the hadronic and electromagnetic amplitudes, ($\phi_i = \phi_i{}^h + \phi_i{}^{em}$), the differential cross-section can be expressed as

$$\frac{d\sigma}{dt} = \frac{d\sigma^h}{dt} + \frac{d\sigma^e}{dt} + \frac{d\sigma^i}{dt} \tag{2.35}$$

where the superscripts indicate hadronic, electromagnetic and interference contributions to the differential cross-section. More explicitely equation (2.35) can be express as

$$\frac{d\sigma}{dt} = \frac{4\alpha^2\pi}{t^2} + \frac{\sigma_{TOT}^2}{16\pi}\left(1+\rho^2\right)e^{bt} + Interference \tag{2.36}$$

where α is the fine structure constant, ρ is the ratio of real to imaginary parts of the scattering amplitudes and b is the nuclear slope parameter.

The electromagnetic amplitudes are written in the following form, keeping the leading terms only at high energy and small momentum transfer $|t|$, $(s \gg m^2 \gg |t|)$,

$$\phi_1^e = \phi_3^e \approx \frac{\alpha\sqrt{s}}{t}, \tag{2.37}$$

$$\phi_2^e = -\phi_4^e \approx \frac{\alpha\sqrt{s}}{4m^2}(\mu - 1)^2 \qquad (\mu = 2.79), \tag{2.38}$$

$$\phi_5^e = -\frac{\alpha\sqrt{s}}{|t|^{1/2}}\,\frac{\mu - 1}{2m}. \tag{2.39}$$

The first and third handronic amplitudes are equal to each other $(\phi_1^h = \phi_3^h)$, and all other amplitudes are assumed to be either very small or zero.

The contribution of the different components to the total polarization is written as the sum of hadronic, electromagnetic and the interference parts.

$$P\frac{d\sigma}{dt} = (P\frac{d\sigma}{dt})^h + (P\frac{d\sigma}{dt})^e + (P\frac{d\sigma}{dt})^i \tag{2.40}$$

In equation (2.35) the interference term originates from the nuclear non-flip amplitude and the coulombic charge-charge interaction. Whereas in equation (2.40), the interference comes from the nuclear non-flip amplitude and the charge-magnetic moment interaction giving a electromagnetic spin-flip amplitude [Kope74]. If we calculate the polarization that arises from the Coulomb-nuclear interference in terms of the helicity amplitudes and keeping the spin-flip hadronic amplitude we have

$$
\begin{aligned}
P\frac{d\sigma}{dt} = & \left(P\frac{d\sigma}{dt}\right)^h \\
& + \frac{\pi}{k^2}\left[Im\,\phi_5^h \cdot Re\left(\phi_1^c + \phi_2^c + \phi_3^c - \phi_4^c\right)\right] \\
& - \frac{\pi}{k^2}\left[Re\,\phi_5^c \cdot Im\left(\phi_1^h + \phi_2^h + \phi_3^h - \phi_4^h\right)\right].
\end{aligned}
\tag{2.41}
$$

By substituting the amplitudes in the above equation and making use of equations (2.30) and (2.32) we have,

$$
\begin{aligned}
P\frac{d\sigma}{dt} = & \left(P\frac{d\sigma}{dt}\right)^h \\
& + \frac{2\pi}{k^2}\left[\frac{\alpha\sqrt{s}}{t}\left(1 + \frac{(\mu-1)^2}{4m^2}t\right) Im\,\phi_5^h\right] \\
& + \frac{\pi}{k^2}\left[\frac{\alpha\sqrt{s}}{|t|^{1/2}}\frac{\mu-1}{2m}\frac{k}{2\pi}\left(\sigma_{TOT} - \frac{\Delta\sigma_T}{2}\right)\right].
\end{aligned}
\tag{2.42}
$$

At high energy we make the assumptions that $s \gg 4m^2$ and $\frac{\mu-1}{2m}^2 t \ll 1$ and equation (2.42) simplifies to

$$
P\frac{d\sigma}{dt} = \left(P\frac{d\sigma}{dt}\right)^h + |t|^{-1/2}\left[\frac{8\pi\alpha}{\sqrt{s}|t|^{1/2}} Im\,\phi_h^5 + \alpha\frac{\mu-1}{2m}\left(\sigma_{TOT} - \frac{\Delta\sigma_T}{2}\right)\right]. \tag{2.43}
$$

Now, going back to equation (2.36) and substituting equation (2.43) we have

$$
\begin{aligned}
P\left[\frac{4\pi\alpha^2}{t^2} + \frac{\sigma_{TOT}^2}{16\pi}\left(1+\rho^2\right)e^{bt}\right] = & P\frac{\sigma_{TOT}^2}{16\pi}\left(1+\rho^2\right)e^{bt} \\
& + |t|^{-1/2}\left[\frac{8\pi\alpha}{\sqrt{s|t|}} Im\,\phi_5^h + \alpha\frac{\mu-1}{2m}\left(\sigma_{TOT} - \frac{\Delta\sigma_T}{2}\right)\right]
\end{aligned}
\tag{2.44}
$$

For large s and $1+\rho^2 \approx 1$ and $\exp(bt) \approx 1$ then the polarization due to Coulomb-nuclear interference is written

$$
\begin{aligned}
P^i &= \frac{P_{\otimes}\sigma_{TOT}^2 t^2 + \frac{\alpha(\mu-1)}{2m}\sigma_{TOT}\left(1-\frac{\Delta\sigma_T}{2\sigma_{TOT}}\right)16\pi|t|^{3/2}}{64\pi^2\alpha^2+\sigma_{TOT}^2 t^2} \\
&= \frac{\sigma_{TOT}|t|^{3/2}}{64\pi^2\alpha^2+\sigma_{TOT}^2 t^2}\left[P_{\otimes}\sigma_{TOT}|t|^{1/2}+\frac{\alpha(\mu-1)}{2m}\left(1-\frac{\Delta\sigma_T}{2\sigma_{TOT}}\right)\right]
\end{aligned}
\tag{2.45}
$$

Following the conventinoal substitutions and assuming zero hadronic spin-flip amplitude, the polarization in the Coulomb-nuclear interference region is written as [Butt78],

$$
P(t) = P^h(t)\frac{1}{1+(\frac{d\sigma}{dt}/\frac{d\sigma^h}{dt})} + P^i(t). \tag{2.46}
$$

$$
P^i(t) = P^i(t_p)\frac{4z^{3/2}}{3z^2+1} \tag{2.47}
$$

where $z = t/t_p$ and $t_p = 3(8\pi\alpha/\sigma_{TOT}) \approx 3.12\times10^{-3}(\mathrm{GeV/c})^2$. The maximum polarization is

$$
P^i(t_p) \approx \frac{\sqrt{3}}{4}(\mu-1)\frac{\sqrt{t_p}}{m} \approx 0.046 \tag{2.48}
$$

where μ is the anamolous magnetic moment of proton and m is the proton's mass. $P^h(t)$, on the other hand, behaves like [Ratn76]

$$
P^h(t) \approx \sqrt{\frac{t}{s}} \tag{2.49}
$$

and the interference term dominates for $|t| \leq 6\times10^{-3}(\mathrm{GeV/c})^2$.

Figure 2.3 shows the differential cross-section and the theoretical prediction for the analysing power as a function of the four-momentum-transfer squared. Although the maximum polarization is only ~4.6%, the forward cross-section is relatively large, ~70 mbarns. This makes such an interference measurement possible.

If, however, the hadronic spin-flip amplitude is other than zero, the picture described above is modified [Kope89]. The polarization measurements, similar to the one described in this work, at 100, 200 and 300 GeV/c [Fide81,Snyd78], indicate flattening of polarization at high energies and at higher t values. If the proton wave-function contains a dynamically enhanced diquark then the spin-flip term appears, i.e. implying pomeron spin-flip. Figure 2.4 shows the $|t|$ dependence of pp elastic polarization in the Coulomb-nuclear interference region versus the pomeron anamolous magnetic moment, M. If $M = 0$, then one has the theoretical prediction as indicated by the thick line. If, on the other hand, M is nonzero, the polarization predictions change depending on the sign of the anamolous magnetic moment of pomeron.

Table 2.1 The behavior of the rotation-invariants under the space reflection, time reversal and the Pauli exclusion transformations. $A = \sigma^{(1)} \cdot \sigma^{(2)}$, $\mathbf{B} = \sigma^{(1)} + \sigma^{(2)}$, $\mathbf{C} = \sigma^{(1)} - \sigma^{(2)}$, $\mathbf{D} = \sigma^{(1)} \times \sigma^{(2)}$ and $E = \sigma_i{}^{(1)}\sigma_j{}^{(2)} + \sigma_j{}^{(1)}\sigma_i{}^{(2)}$.

Rotation Invariant	Space Reflection	Time Reversal	Exclusion Principle
$\mathbf{1}$	yes	yes	yes
$\mathbf{A}$	yes	yes	yes
$\mathbf{B} \cdot \hat{\mathbf{m}}$	no	no	yes
$\mathbf{B} \cdot \hat{\mathbf{n}}$	yes	yes	yes
$\mathbf{B} \cdot \hat{\mathbf{l}}$	no	yes	yes
$\mathbf{C} \cdot \hat{\mathbf{m}}$	no	no	no
$\mathbf{C} \cdot \hat{\mathbf{n}}$	yes	yes	no
$\mathbf{C} \cdot \hat{\mathbf{l}}$	no	yes	no
$\mathbf{D} \cdot \hat{\mathbf{m}}$	no	yes	no
$\mathbf{D} \cdot \hat{\mathbf{n}}$	yes	no	no
$\mathbf{D} \cdot \hat{\mathbf{l}}$	no	no	no
$\mathbf{E}\,(m_i m_j)$	yes	yes	yes
$\mathbf{E}\,(n_i n_j)$	yes	yes	yes
$\mathbf{E}\,(l_i l_j)$	yes	yes	yes
$\mathbf{E}\,(m_i l_j + m_j l_i)$	yes	no	yes
$\mathbf{E}\,(m_i n_j + m_j n_i)$	no	no	yes
$\mathbf{E}\,(l_i n_j + l_j n_i)$	no	yes	yes

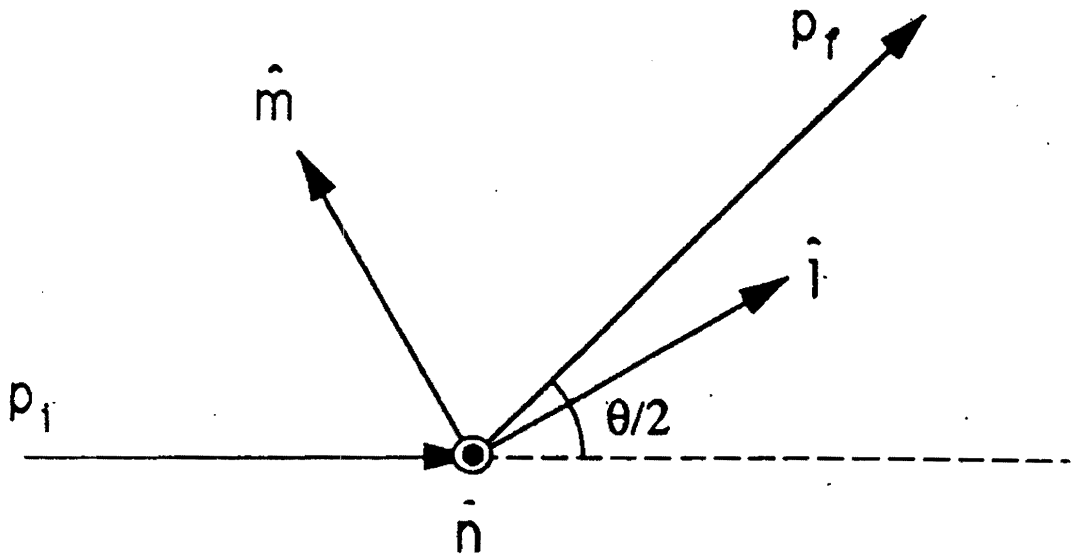

Figure 2.1 Coordinate system in the center of mass frame. $\hat{\mathbf{n}} = \frac{\mathbf{p}_i \times \mathbf{p}_f}{|\mathbf{p}_i \times \mathbf{p}_f|}$ is pointing out of the page.

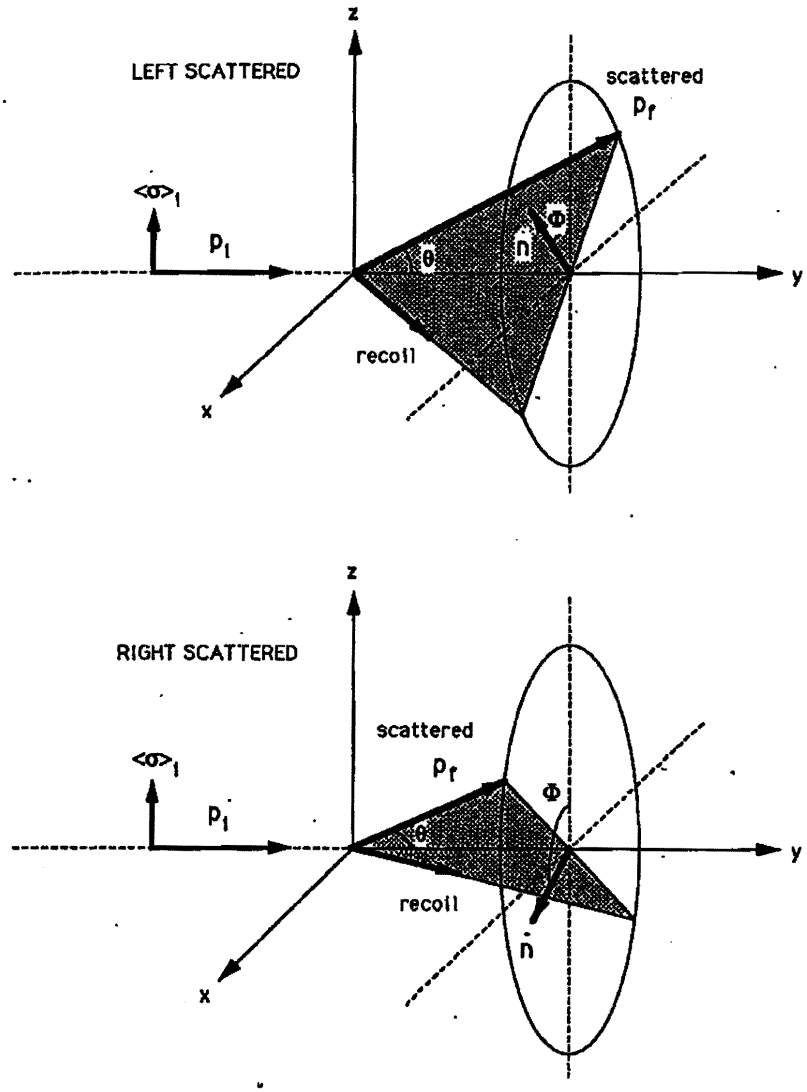

Figure 2.2 Schematic representation of left and right scattered particles. The shaded area is the scattering plane. The polarization direction is indicated as $< \sigma >_i$.

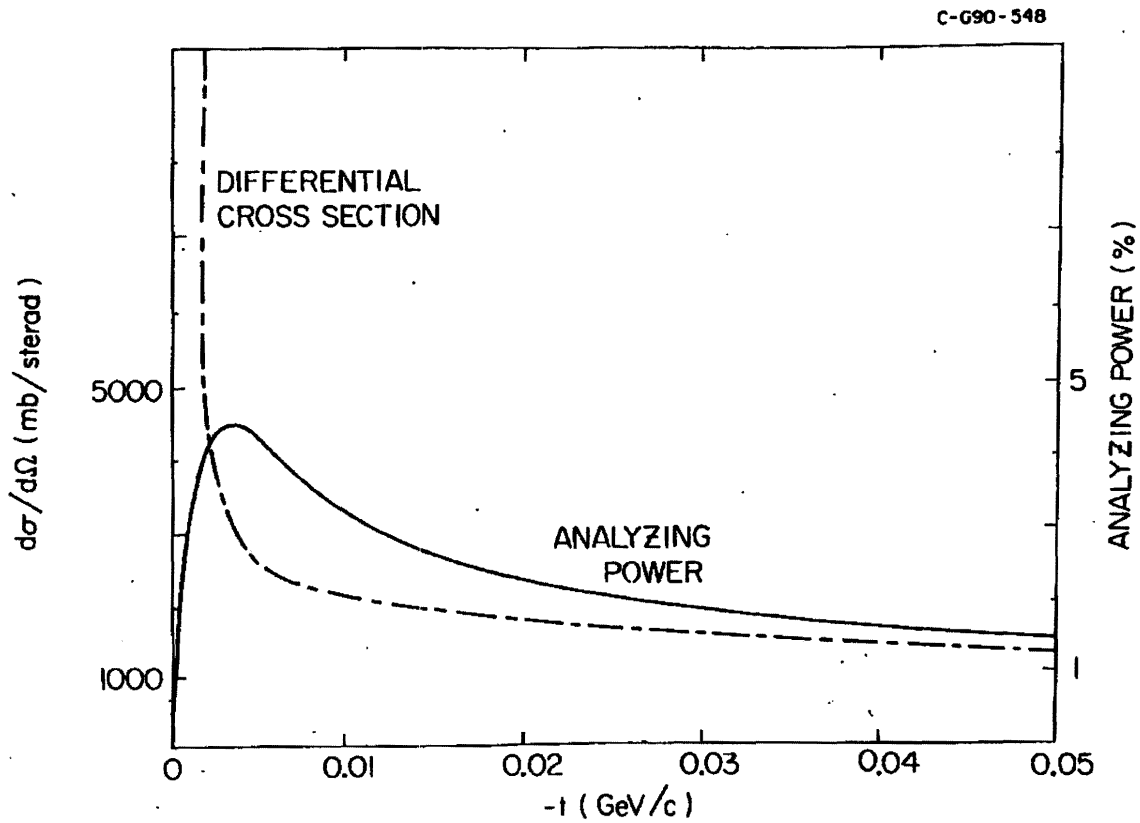

Figure 2.3 Plots of the differential cross-section and analysing power as a function of $|t|$ for the CNI process.

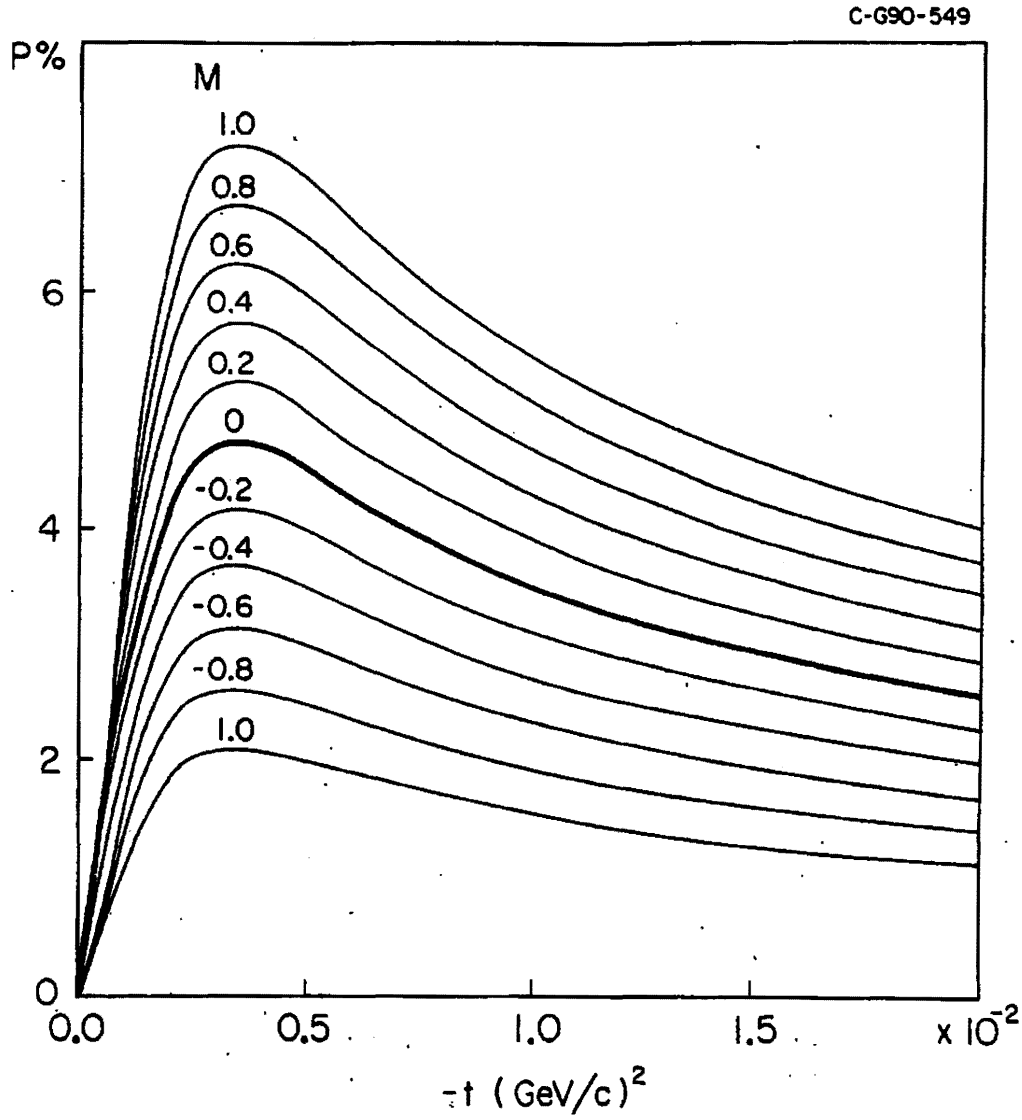

Figure 2.4 The t-dependence of pp elastic polarization in the Coulomb-nuclear interference region versus the pomeron anomalous moment, M [Kope89].

CHAPTER III

POLARIZED PARTICLE BEAMS

Study of spin effects in high energy particle physics started almost three decades ago and the first acceleration of polarized particles became possible with the advent of polarized ion sources. Zero Gradient Synchrotron (ZGS) at the Argonne National Laboratory achieved at first 6 GeV/c, and later 12.75 GeV/c polarized proton energies in the 1970's [Yoko80]. Alternating Gradient Synchrotron (AGS) at the Brookhaven National Laboratory recently produced 22 GeV/c polarized protons by avoiding (*jumping*) the depolarizing resonances. The number of so-called depolarizing resonances increases in direct proportion with the beam energy, e.g., at 20 TeV SSC there will be 36,000 depolarizing resonances which, in effect, render the conventional polarization techniques inadequate. At the Cooler Ring of the Indiana University Cyclotron Facility (IUCF) a recent test of the Siberian Snake concept, which was first proposed by Y. S. Derbenev and A. M. Kondratenko [Derb77] in 1974, showed that it is possible to remove the depolarizing resonances by precessing the spin 180° about a horizontal axis [Kris89]. Among a handful of other alternatives, the production of high energy polarized protons from the decays of hyperons was studied at Serpukhov and CERN [Over69]. It is this particular idea which makes the polarization of protons at Fermilab possible at the MP beam line.

The production of polarized proton and antiprotons is carried out in several distinct stages at Fermilab. Initially the high energy protons from the Tevatron are extracted into the primary beam line and transported onto a production target and then, via a secondary

beamline, the polarized protons from the decay of Λ hyperons are transported down to the experimental hall. In the sections that follow, each stage is treated separately [Mala83, Gros89].

Primary-Proton Beam

Figure 3.1 shows the details of the primary beam-line. The 800 GeV/c protons from the Tevatron are split into two beam-lines, Meson Center (MC) and Meson Polarized (MP). It is not possible for both beam-lines to operate simultaneously with the primary beams from the Tevatron. However, it is possible to run diagnostics tests during the periods when the MC beam-line is receiving the primary protons from the Tevatron. This is accomplished by inserting a 0.2 radiation-length aluminum target in the intersection area of MP and MC beam-lines. This produces a parasitic test beam of 30 GeV/c and a flux of 10^4 particles per spill. The test beam consists of approximately 20% positrons and makes the tuning and testing of the detectors possible without sacrificing valuable beam time.

Two sets of cryogenic dipole magnets bend the primary-proton beam and a set of quadrupole magnets focuses the beam prior to the beryllium production target. After the beam is extracted into the MP line, the size of the proton beam at the production target is 0.8 mm (rms) in the horizontal, and 2.0 mm (rms) in the vertical direction. The primary protons travel 415 m from the MC-MP beam split to the production target with varying intensities from 0.3 to 2×10^{12} during a 20-second spill. The Tevatron has a cycle time of about one minute with a duty factor of approximately 33%.

In order to monitor the performance of the beam transport, four segmented-wire ion chambers (SWIC) are installed in front of the two cryogenic dipole-magnet sets, one before the quadrupole-magnet set, and the fourth in front of the production target. These

chambers provide a visual output to the beam monitors located in the control room, thereby enabling the experimenters to overview the physical location of the beam.

Polarized Proton Production

The polarized protons are produced via parity-nonconserving decay of Λ hyperons. Upon impact of the 800 GeV/c primary proton beam onto the beryllium production target, many unpolarized Λ hyperons are created. In the rest frame of the unpolarized Λ, the decay of $\Lambda \rightarrow p + \pi^-$ occurs isotropically and the decay-proton is 64% polarized with the spin direction along the proton momentum [Cron63]. However, the paths of decay-protons can be traced back to the plane of production target in the laboratory frame. Protons with components of their momentum transverse to the Λ direction appear to come from a virtual source as shown in Figure 3.2. For a fixed Λ decay distance, protons with the same transverse spin component originate from the same point of the virtual source, regardless of the direction of Λ. As illustrated in Figure 3.2, for a Λ decay distance of fixed length, the protons with spin *up* come from the virtual source in the bottom and the protons with spin *down* come from the virtual source above the production target. Thus the transverse spin component of the proton is correlated to its projected position at the virtual source.

The transverse position of the virtual source depends on the decay distance, i.e. the point of Λ decay, and on the angle at which the polarized proton is produced *. The virtual source of the polarized protons is then imaged with the beam optics in order to optimize the virtual source configuration, which in turn makes possible a precise polarization selection. There are two main criteria for a good determination of polarization:

---

* The maximum proton laboratory decay angle is $\theta_{max} = \cos^{-1}(-\beta/\beta_\Lambda) = 96.1°$, where βc is the velocity of proton in the Λ rest frame and $\beta_\Lambda c$ is the velocity of Λ in the laboratory frame. The decay angle is measured in the Λ rest frame between the proton direction and the Λ direction in the laboratory.

1. The beryllium target is 1.5 mm wide, 5.0 mm high and 30.0 cm long (0.74 radiation length). These dimensions are chosen so that they are small compared to the size of the virtual source.
2. The decay length d of Λ must be well-defined such that Λ's that decay in the region of 9-30 m range are accepted. It is in this range that one-half of the lambda hyperons decay into p's and π^-'s.

The particle polarization is then determined from the correlation between the position of the virtual source and the proton momentum direction. The proton momentum direction is then correlated to the proton polarization direction. Figure 3.3 was generated by a computer simulation of the beam line where the average particle polarization is plotted as a function of the horizontal position at the intermediate beam focus for a 185 GeV/c proton. It is in this position that the tagging of momentum and polarization is performed for each individual beam particle. The particle tagging measures only the horizontal component of the transverse proton polarization. This makes it possible to use protons with both signs of polarization simultaneously, which is a considerable advantage over many other polarized particle beams.

The polarized antiprotons are created in a way analogous to that of the protons. In this case, the decay of $\bar{\Lambda}$ produces polarized antiprotons with antiparallel polarization to their momentum direction in the $\bar{\Lambda}$'s rest frame. Similar to the polarized proton case, the antiproton beam polarization is found using the relation between the antiproton momentum direction and the virtual-source position on the production target plane.

Figure 3.4 shows the results of computer simulations of the total polarized proton and antiproton intensities per spill as a function of the polarized beam momentum, and also the intensities for the tagged portion that have an average beam polarization of 45%.

Polarized (Secondary) Proton Beam

The design criteria behind the MP beam line (Figure 3.5) were:

1. that the beam provide a clean sample of protons from the decays of Λ in a narrow momentum band and have a small phase space. In order to meet these conditions a reduction of beam particles by a factor of 10^5 was necessary.
2. that the beam line must be flexible enough to determine and manipulate the proton spin direction.

As shown in Figure 3.5, two dipole magnets eliminate the unwanted charged particles from the beam right after the production target. Each dipole magnet is 3.5 m in length; the first dipole has a 2.86 cm gap with 2.2 T magnetic field strength, and the second has a smaller gap of 1.59 cm with a field of 2.4 T. The total bend for a 800 GeV/c primary proton beam through these magnets is about 6 milliradians. Non-interacting primary protons are bent downwards into a beam dump. Charged particles produced at the target are also bent down away from the acceptance to a brass absorber insert. Furthermore, the charged particles that are produced too close (less than 9 m from the target) by Λ decay are swept away from the beam (Figure 3.6). The brass insert located between 6.55 m and 9.14 m (inside the second dipole) from the target acts as a collimator for the neutral particles while allowing the passage of the primary beam. The neutrals are primarily neutrons, gammas and lambdas with a flux of 10^{11} particles per spill. The hole in the brass insert, with a diameter of 1.27 cm, reduces the number of neutron interactions which may simulate the Λ decays downstream. The insert extends 91 cm from the endplate of the second dipole in order to collimate the charged particles that are produced within the insert away from the acceptance. Following the second dipole, a 53 m long vacuum pipe minimizes the beam-air interaction.

The primary beam iron dump starts at 18 m and extends to 21 m. At the upstream side of the dump, the primary beam strikes approximately 8 cm below the center of the hole for the neutrals. This design was studied extensively to ascertain that the muon background and hadron contamination to the beam is minimal.

The Λ decay region starts at 9 m and ends at 30 m. As the neutral beam is dumped into the dump, the protons are bent down and partially momentum selected such that the particles have $\pm 30\%$ of the 185 GeV/c beam momentum value while at the same time reducing the beam flux to 10^9 per spill. The neutral dump consists of two brass blocks ($7.5\,\mathrm{cm} \times 29\,\mathrm{cm} \times 2\,\mathrm{m}$) and two concrete blocks of 2 m length situated downstream of the brass blocks. The neutral dump is positioned at 70 m from the production target.

At this point, the polarized protons from lambda decays can be steered down to the experimental hall, approximately 260 m downstream, and can be momentum and polarization-tagged in the process.

Polarized Proton Beam Optics

Figure 3.7 illustrates the essential principles of the secondary polarized beam optics. Each quadrupole magnet doublet is represented by a lens. The focal lengths for f_1 and f_2 are approximately 32 m and 48 m, respectively. The rays that originate from the virtual source become parallel between the first two lenses, and are then focused to a point at the intermediate focus. Symmetrically, they become parallel between the third and the fourth lens, and at the end are focused to form the final image. There are several underlying criteria in the design and construction of this type of transport system.

1. Focusing is performed both as point-to-point and parallel-to-parallel focusing in each plane in order to introduce no net spin precession throughout the transport

system. In other words, the correlation between the polarization state of a given particle and its position on the virtual source plane is preserved.

2. To minimize abberations on the beam optics, the quadruople magnet lengths and beam-momentum bandpass are kept minimal.
3. Figure 3.7 must be applied separately to both the vertical and horizontal planes. The focal lengths and magnifications are different for the two planes because the focusing quadrupole magnets must be used in doublets of opposite polarity.

In the design stage of the beam-line, the program TRANSPORT [Brow77] was used to study the quadrupole and dipole magnet strengths and drift lengths. The beam transport program TURTLE [Care71] was used to understand the beam properties. These widely used programs were modified to incorporate the precession of particle spin in the quadrupole magnets.

The bending and focusing of the beam are decoupled from each other as much as possible (Figure 3.5). The bending magnets occur in achromatic sets of four, entirely contained between two quadrupole doublets. Any dispacement or angular deflection due to the bend in the beam is restored by three subsequent bends. Each set of four bending dipoles produces no net momentum dispersion or spin precession. Two effects of dipole magnets, edge focusing and magnetic-field nonuniformities could possibly distort the image from quadrupole focusing. Both of these effects are small for this beam line.

There are two sets of four bending magnets in the beam line. The first set bends the particles around the neutral dump area. The second, located at the intermediate focus (160 m), is used for the momentum measurement of the beam. The two sets of quadrupole magnets focus the beam at the intermediate focus and the second doublet focuses the beam in the experimental area at the target location (320 m). The position of the intermediate focus depends on the beam momentum. For 185 GeV/c protons and

typical magnetic fields for the magnets it is at 160 m. If the momentum of the beam is higher, then the intermediate focus shifts downstream.

The polarization of the proton is measured throughout the beam line as it is essential to know the proton spin in any given reference frame. In the formalism used [Barg57], the spin direction of the proton is defined only in the particle's rest frame. Several coordinate transformations are needed to determine the spin direction. For instance, the proton momentum direction which is described in the Λ rest frame is transformed to the proton's rest frame and, in this frame, the proton spin direction is correlated to the direction of its momentum. By another transformation, the average spin of a given phase space is related to a position in the laboratory frame.

Spin-Rotating Magnets (Snake Magnets)

The purpose of this set of magnets, located just before the experimental targets, is to change the polarization state of the particle from one to another. In order to cancel out systematic errors, one needs to reverse the polarization state of the incoming proton periodically and, in addition, one needs to be able to change the spin state from horizontal (S) to vertical (N) or longitudinal (L) for various measurements. The guiding principle of the snake is the noncommutivity of orthogonal directions.

MP Snake consists of 12 dipole magnets (1.38 T) and each precesses the proton spin by 45°. To change the spin state from horizontal to normal (S to N), eight of twelve magnets are used (1, 2, 4 and 11 not used) (Figure 3.8). For the L type of spin state all twelve magnets are powered (Figure 3.9).

In the N type of beam, reversing the spin direction by 180° requires only four of eight magnets flip the field directions, whereas in the L type all the snake dipoles need to

change field directions. Changing the magnetic field directions from one to another takes about 2 minutes and this is performed every 10 machine spills.

The performance of the snake was verified to be satisfactory by observing the displacements of the beam particles at 50 m downstream from the snake magnet in S to N configuration. When the magnets were on or were reversed, a shift of less then 0.5 mm was observed in x-direction. This indicates that the magnets are relatively well matched and that there is no net bend in the system. Some of these effects will be discussed in Chapter VI.

Beam Tagging System

The beam tagging system is an integral part of the many measurements that are performed in this experiment. It measures the momentum and the polarization of each beam particle and sends this information downstream on fast cables to individual experiments in the experimental area. These signals are used to form pretriggers and triggers.

Figure 3.10 shows schematically the layout of the setup. The particle momentum is tagged vertically, and the particle polarization is tagged horizontally, and figure 3.11 shows the hit patterns in ten of the beam hodoscopes in the tagging system. These plots are routinely used to check for dead or weak channels and the follow-up electronics. Figures 3.11 and 3.12 show the proton momentum and polarization as measured by the tagging system. A total of 30 bins cover the full $\pm$ 9%momentum bite with an estimated resolution of approximately 1.5% (rms). In the polarization plot, number of particles vs polarization value, the central peak is the distribution of particles with a small percentage of polarization. Protons with polarization values +35% to +65% are designated to be *positive* and, symmetrically, protons with polarization values of –35% to –65% are designated to be *negative*. Beam tagging generally operated with typical beam rates of 0.3 to 1×10^6

beam particles per second. At higher rates of 2×10^7 particles per second, the accidental rate of beam trigger scintillators increased by 2%.

A study of the beam tagging system as a function of the beam rate showed that some particles were not properly tagged. This takes place if

1. a second beam particle enters the system within 80 ns required by the tagging electronics,
2. more than one particle is contained in the 18 ns accelerator micro-bucket,
3. charged secondary particles are produced from beam-hodoscope interaction,
4. the particle has a momentum outside the $\pm$ 9% momentum bite and
5. the tagging system is busy sampling the previous event.

The first two of these factors are independent of the beam intensity. The charged secondary particles account for $\sim$ 19% loss of events due to multiple hits. The beam tagging dead-time contributes $\sim$ 10% loss of beam events. During the CNI data-taking period, the beam intensity at the MP6SEM was 9.8×10^{11}, and at MP9SC1 it was 1.7×10^7 protons per spill.

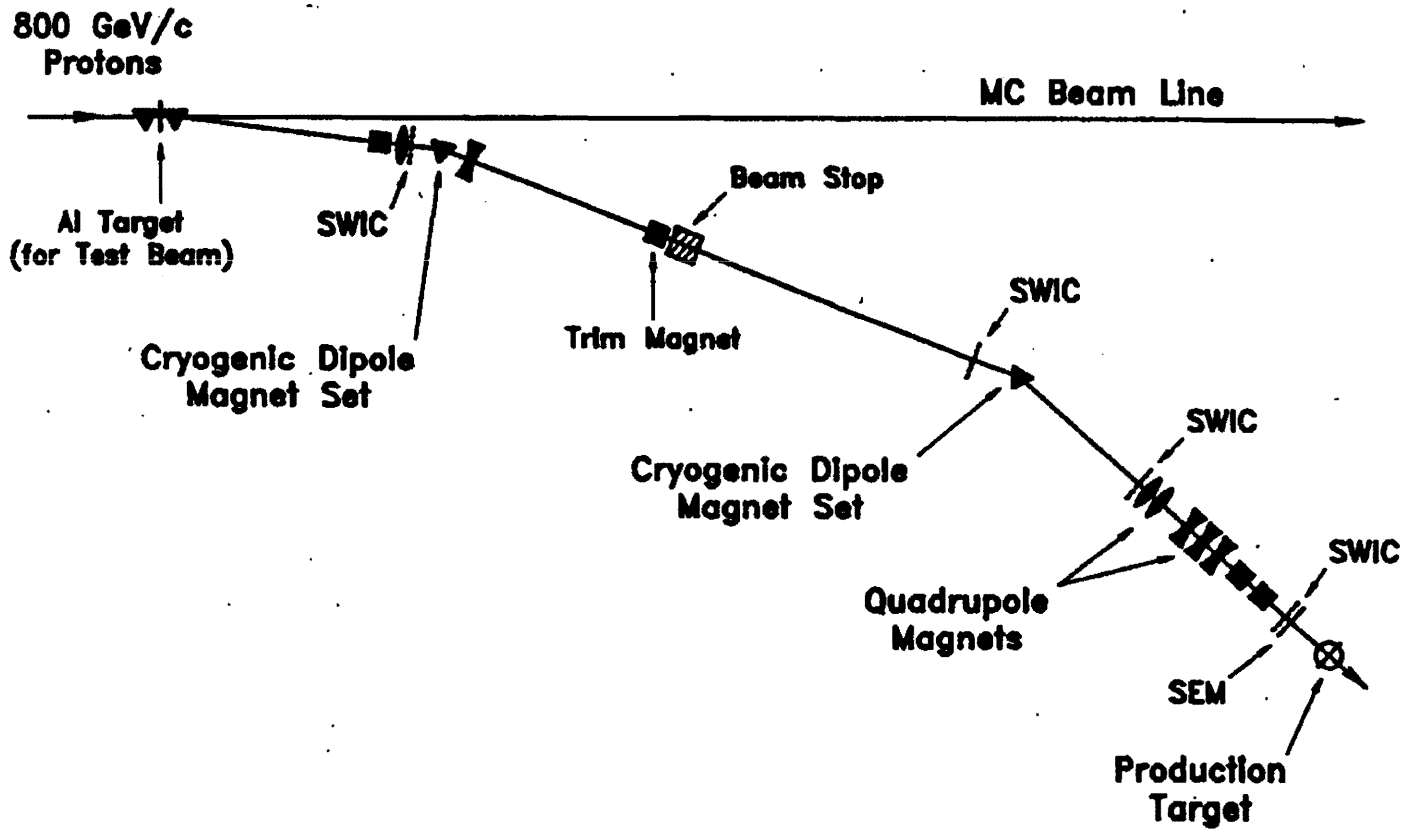

Figure 3.1 Diagram of the MP primary beam-line. At the split where the Al target is positioned, the MP beam-line branches off from the MC beam-line. Shown are the two sets of cryogenic dipole magnets, segmented wire ion chambers (SWICs), secondary emission monitor (SEM) and finally the beryllium production target (not to scale).

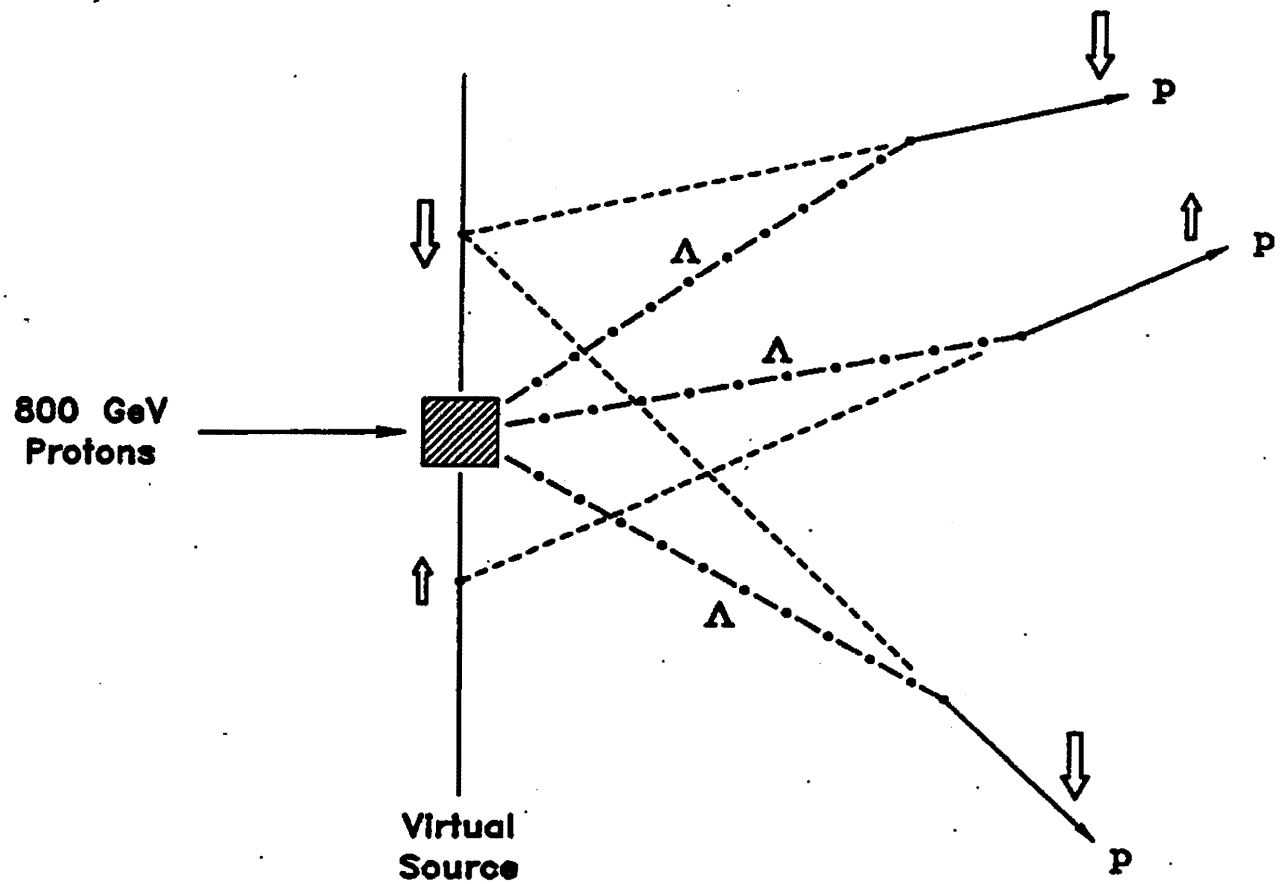

Figure 3.2 Λ hyperons are produced by the incident 800 GeV/c protons on a beryllium target. Lambdas decay into protons and negatively charged pions (not shown). The transverse spin component of the proton is correlated to its projected position at the virtual source. Arrows indicate the relative magnitude of the proton's polarization.

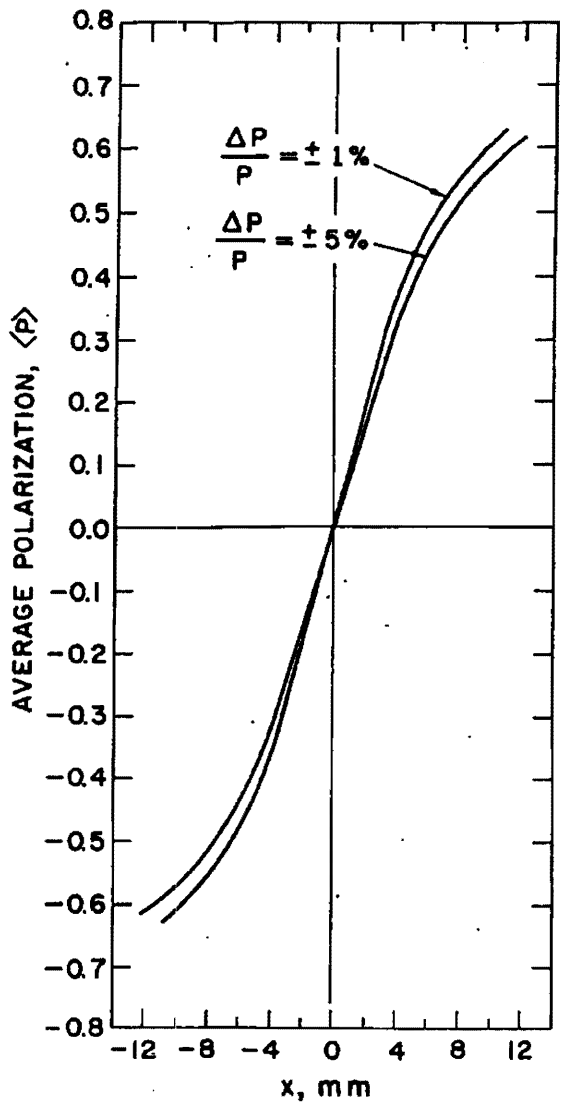

Figure 3.3 Correlation between the average proton polarization and the horizontal position at the intermediate focus for a 185 GeV/c beam.

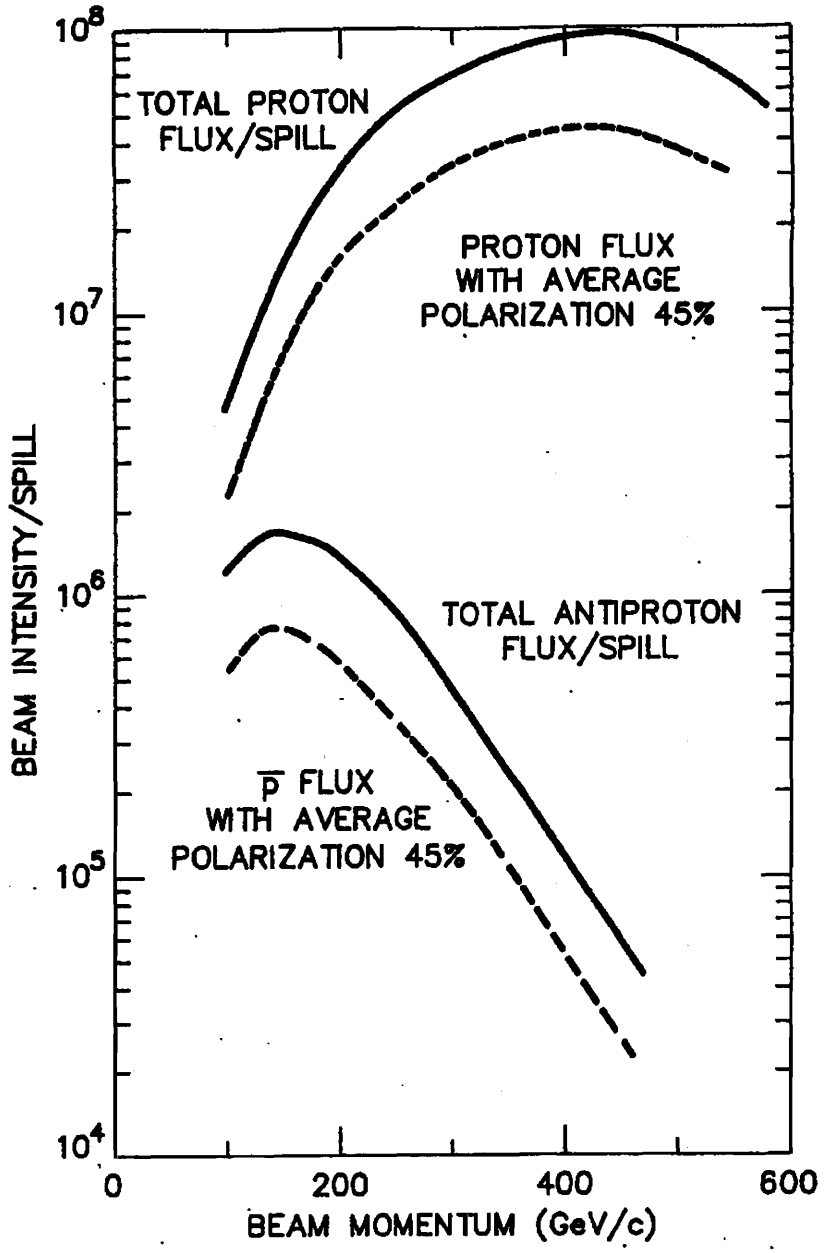

Figure 3.4 The calculated polarized-proton and -antiproton beam intensity per spill as a function of the beam momentum. The incident primary beam momentum is 800 GeV/c and the adjustable collimator is assumed to be fully open.

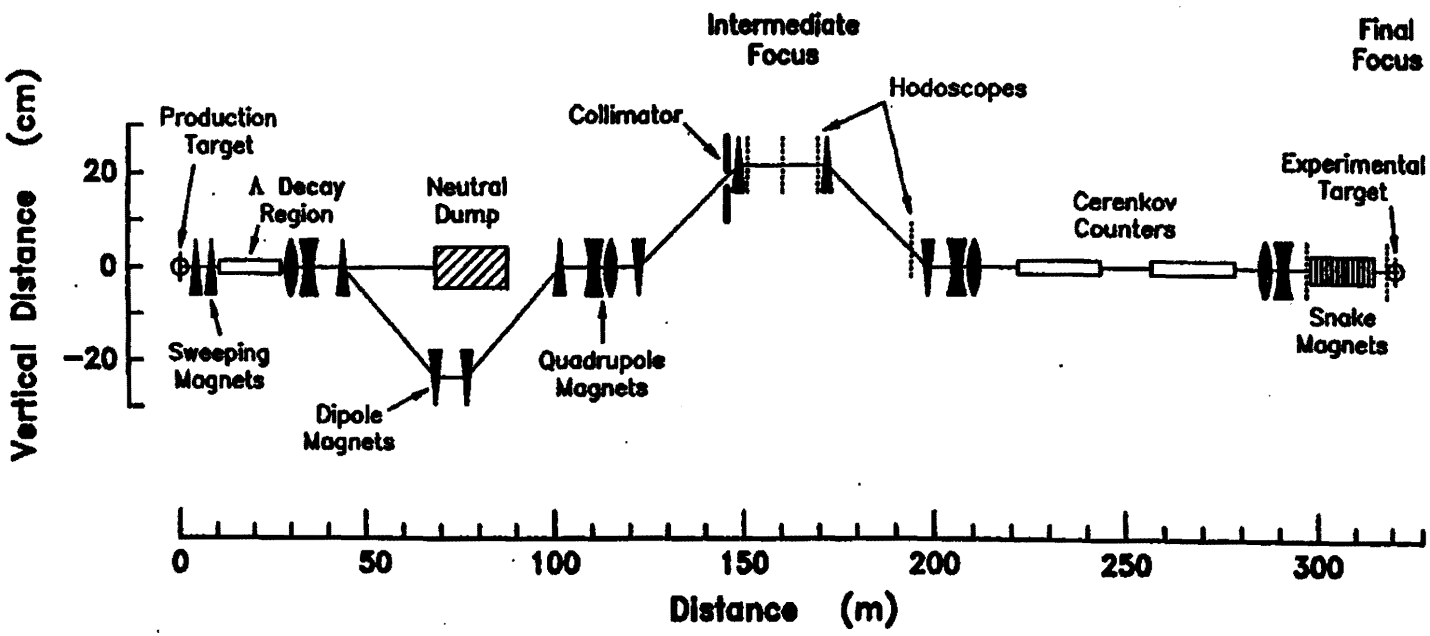

Figure 3.5 The side view of the secondary beam elements. The secondary beam-line consists of production target, neutral particle dump, adjustable collimator, beam tagging region, snake magnets, Cerenkov counters and experimental target(s).

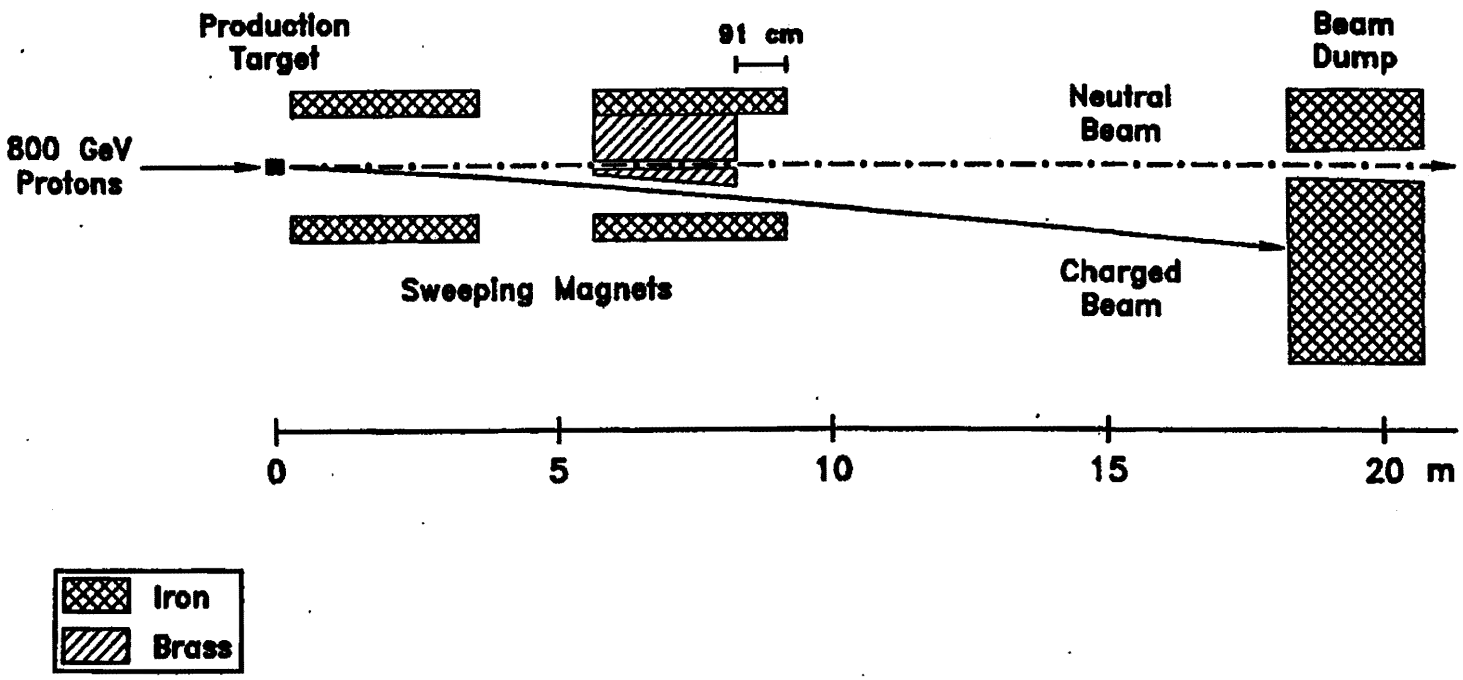

Figure 3.6 Side view of the production target and the primary beam dump area. The separation of the neutral and charged particles is accomplished by two dipole magnets. A collimator inside the second magnet determines the size of the neutral beam. The side view of the elements is not to scale.

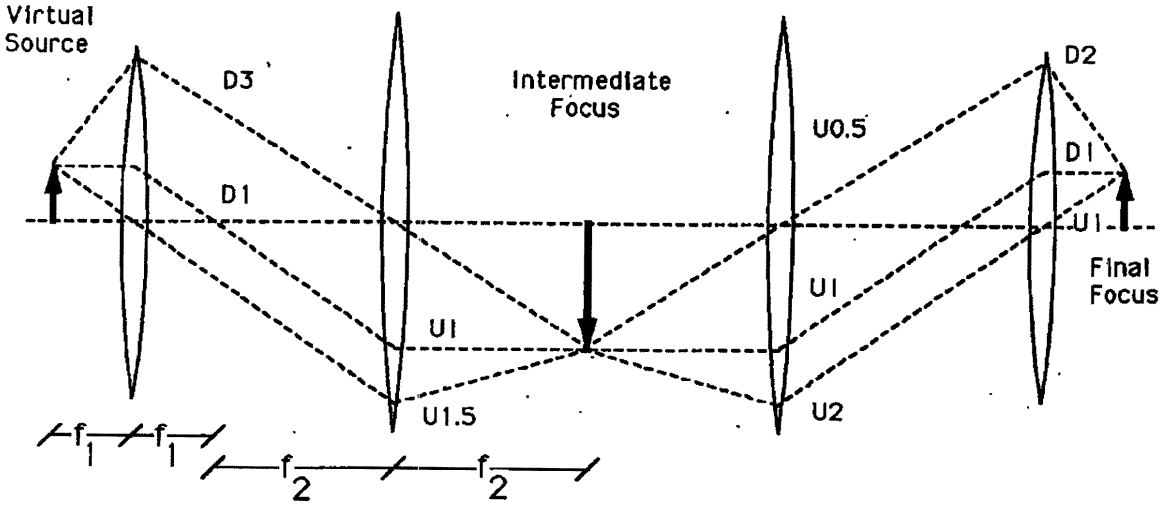

Figure 3.7 Beam optics of the polarized proton beam-line. D1 indicates one unit of downward bending field integral, U1.5 indicates 1.5 units of upward bending field integral, etc. The spin-precessing integrals add up to zero and this, in a general way, demonstrates that polarization is preserved at the nominal beam momentum.

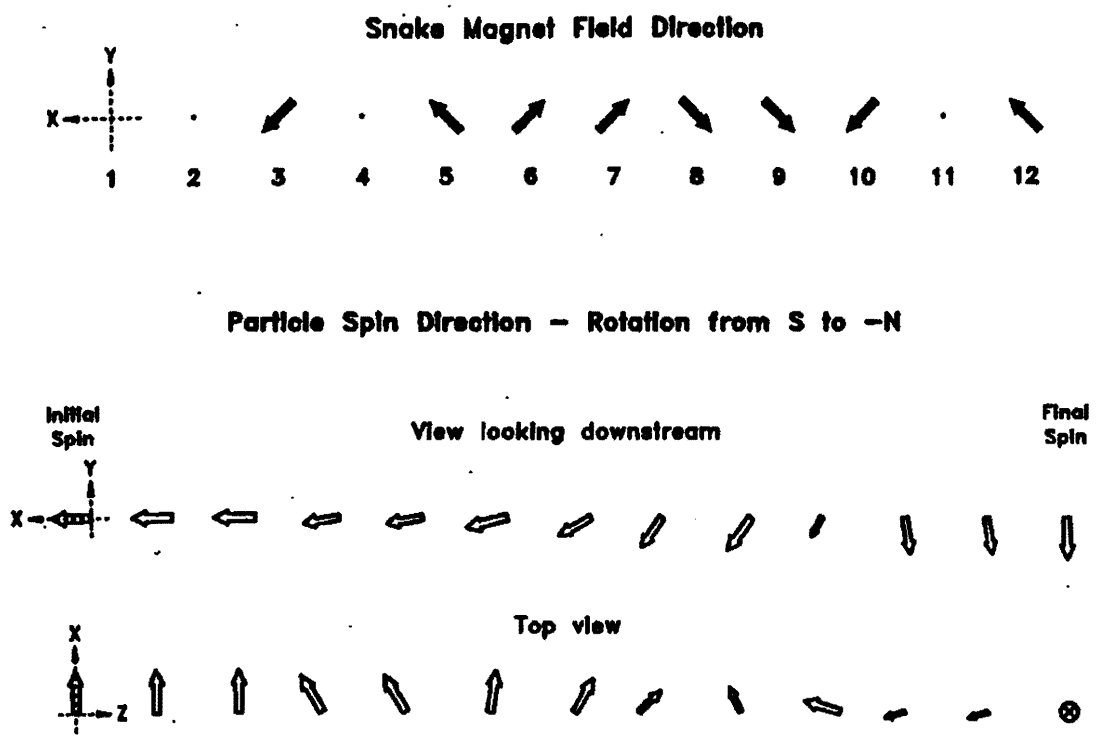

Figure 3.8 Schematic representation of the spin rotation from S (horizontal) to N (vertical) direction through the snake magnets. The first line shows the magnetic field direction in each of the dipoles (dots represent that the field is off). The second line shows the particle spin direction looking downstream, and the third line is the view of the spin direction from the top.

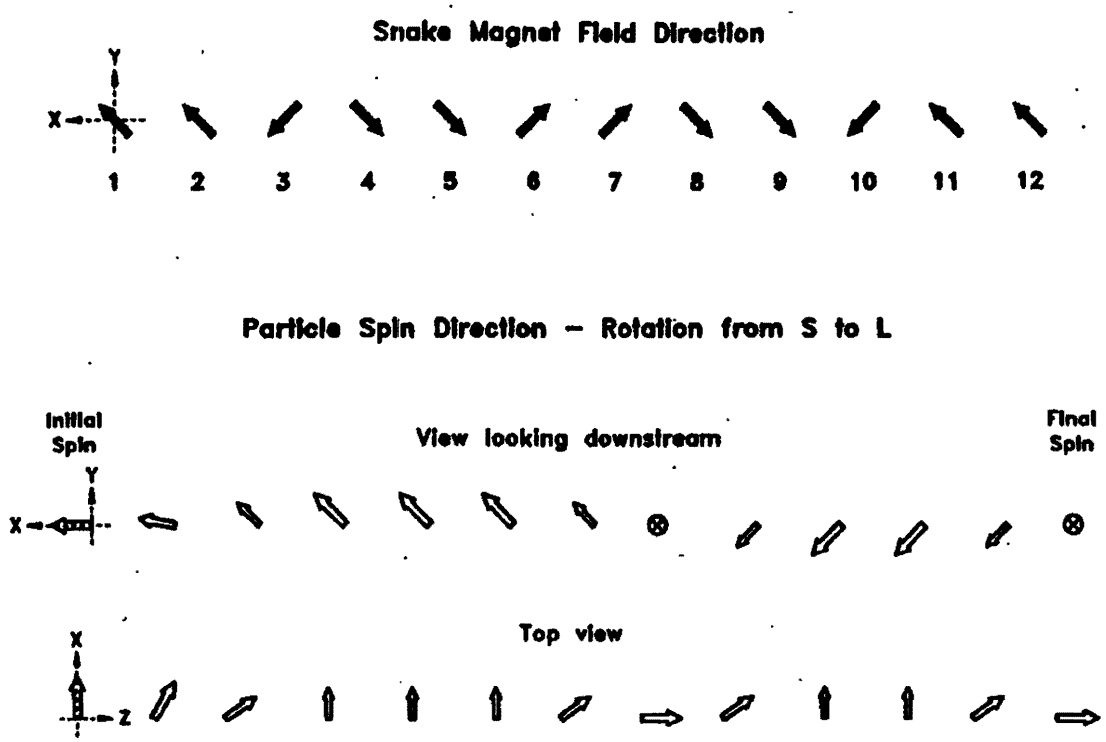

Figure 3.9 Schematic representation of the spin rotation from the S (horizontal) to the L (longitudinal) direction through the snake magnets. See Figure 3.8.

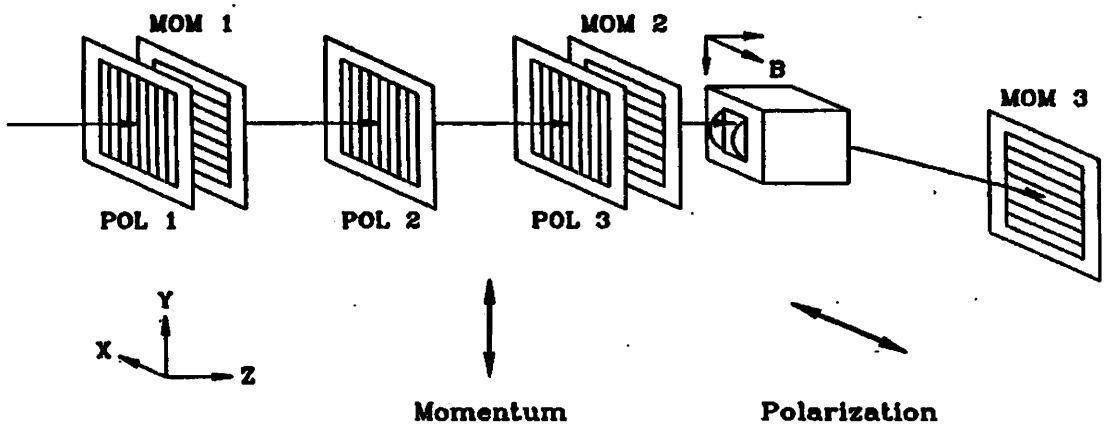

Figure 3.10 Conceptual layout of the beam tagging hodoscopes. The particle momentum is measured in the vertical direction and the particle's polarization is determined from the momentum and the horizontal position.

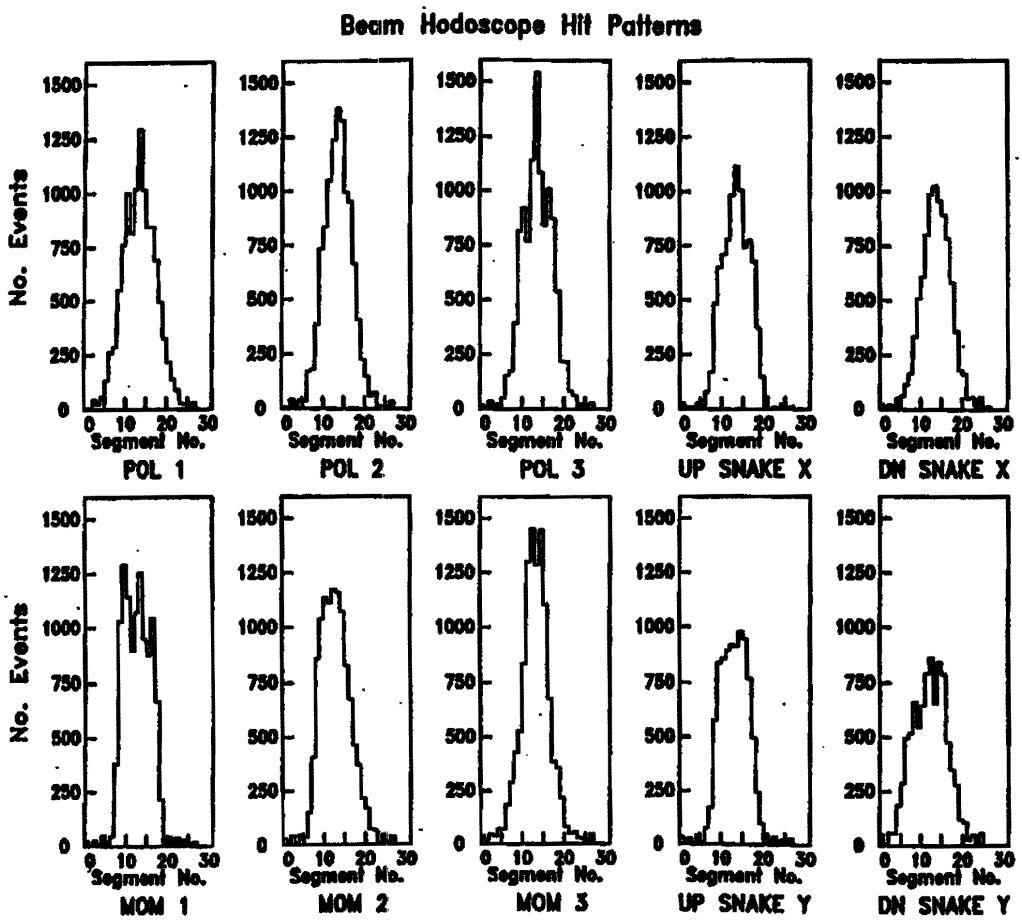

Figure 3.11 Distribution of the raw-hit patterns in the ten beam hodoscopes.

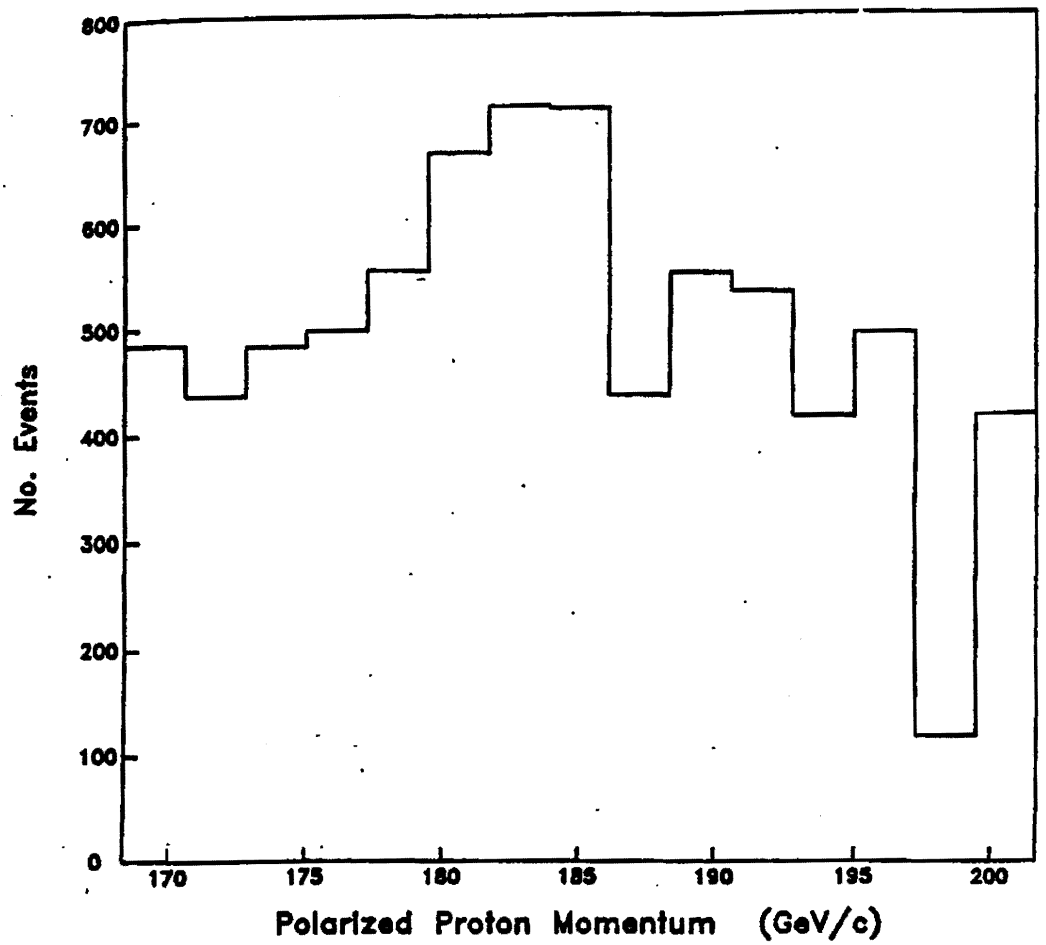

Figure 3.12 Momentum distribution of the 185 GeV/c polarized proton beam as measured by the tagging system. The beam hodoscopes give discrete positions that lead to bin-to-bin variations.

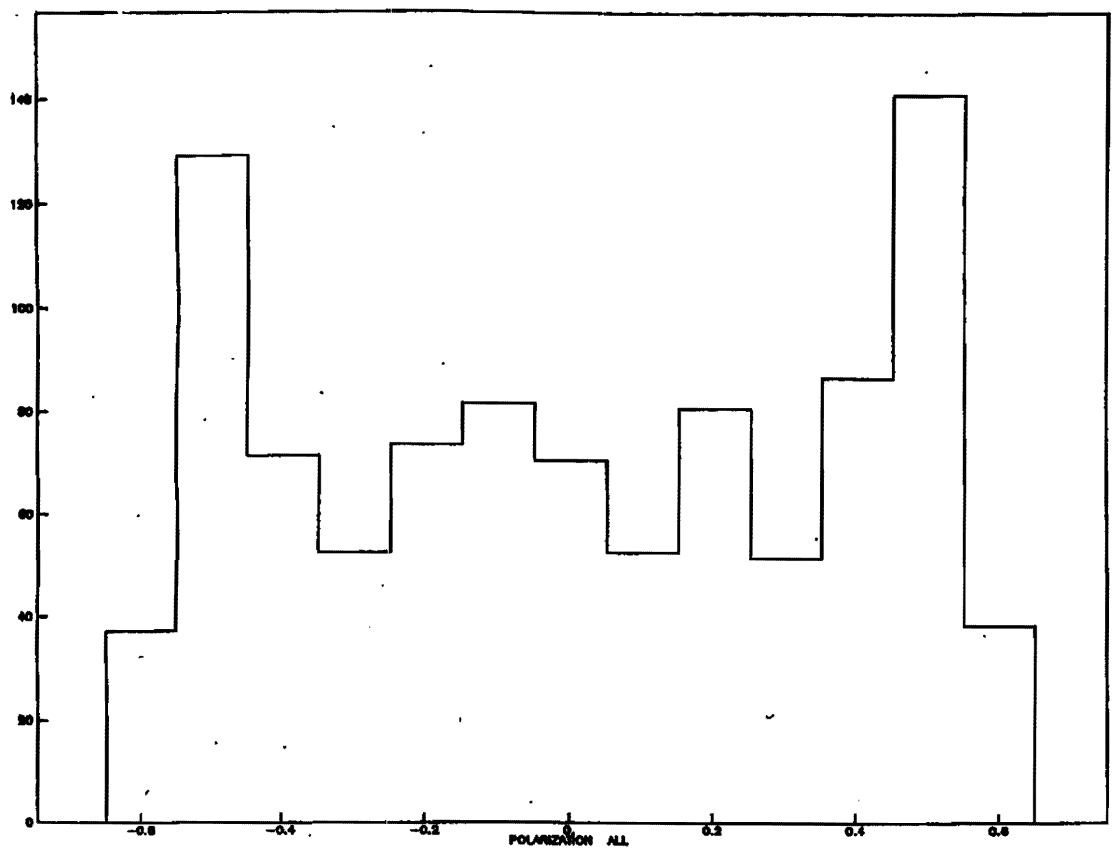

Figure 3.13 Polarization distribution of protons measured by the beam tagging system.

CHAPTER IV

EXPERIMENTAL SETUP

Figure 4.1 shows the top-view of the CNI polarimeter. Polarized protons from Λ decay strike the active targets after the spins of the protons are rotated from the L state to the N state by the spin-rotation magnets. Beam hodoscopes, beam chambers, before and after the spin-rotation magnets, and a pair of multi-strip silicon detectors before the targets track the incident beam. The scattered track after the active targets is detected by a series of MWPCs (PC1, PC2, BK3, PC4', PC5", PC5' and PC5) up to the analysing magnet, which is located at $z = 15.04$ m. The deflected track by the analysing magnet is measured by yet another set of MWPCs (PC6, PC7, PC7', PC13 and PC14) and the Gray-Code hodoscope ($z = 46.20$ m). In order to center the deflected beam in the middle of the GC hodoscope, PC13, PC14 and the GC were mounted on a remote-controlled movable pedestal. The deflection from the undeflected beam axis was about 12.98 cm at the GC when the magnet was operating at 2500 amperes.

CNI Target (Trans-Stilbene)

The CNI target ensemble consists of 6 trans-stilbene (diphenyl-ethlylene, $C_{14}\ H_{12}$) crystals (Table 4.1). The choice of trans-stilbene targets for this type of measurement was based on previous experiences [Akch89, Azai83, Azai87] in elastic scattering experiments and its pulse shape discrimination characteristics, as explained in some detail below. Trans-stilbene is a transparent and brittle organic crystal that can be grown as a single block, e.g. the Bridgeman technique, and then sliced into thin slabs. Targets 1–5 were

grown and cut in Saclay, France and Target 6 came from Trieste, Italy. Trans-stilbene has the following properties; molecular weight, 180.24 gr/mole; density, 1.164 gm/cm^3; 0.0467×10^{24} hydrogen atoms/cm^3 and 0.0545×10^{24} carbon atoms/cm^3.

The centers of the targets were aligned on an optical bench with their light collective assembly to ± 0.5 mm in y- and x-directions with respect to each other. The alignment procedure was checked and repeated in the beamline after the installation of the entire target assembly with respect to the beam center.

The targets are oriented normally to the beam direction in order to minimize the amount of energy deposited by through-going (minimally ionizing) protons and to maximize the probability of detecting the protons that recoil (heavily ionizing) at angles of about 90°. The difference in pulse shapes between the through-going and the recoil proton, which deposits all of its energy in the target, is the principal idea of the discrimination between the two cases. This constitutes the first selection criterium in the first level trigger. There are, however, practical difficulties associated with this idea. The energy distribution of the through-going particles obey the asymmetric Landau distribution. This distribution has a long *tail* in the higher energy end which extends somewhat into the energy range where energy distribution of the recoil protons starts. In order to minimize this effect and provide a large pulse for triggering over threshold, one needs to choose an *active* scintillating target that posesses pulse-shape discrimination (PSD) characteristics, i.e. the time dependence of luminescence depends on the ionization density of the incident track and the energy of the through-going particle.

In general one has to consider the following points in choosing an organic scintillating crystal for an active target:

1. the scintillation emission spectrum and the transmission of this spectrum through the scintillator material,

2. the absolute scintillation efficiency, the response resolution and the associated energy resolution,
3. the fast timing characteristics, time resolution and parameters that describe the *prompt* and *delayed* components,
4. PSD characteristics, including the relative intensities of the different components,
5. the directional dependence of scintillation response.

Figure 4.2.a shows the fluorescence spectra of trans-stilbene for a 1 cm^3 crystal [Birk54]. The spectrum extends from 365 nm to 470 nm, with a mean wavelength at about 400 nm, and the maximum fluorescence takes place at 410 nm. The spectra that are shown are measured under a set of different conditions: (b) reflection from a thick crystal, (c) transmission through a 1 cm crystal, and (d) short wavelength limit mark for the transmission spectrum of trans-stilbene. The molecular fluorescence spectrum where (b) overlaps with (d) is removed from the transmitted spectrum. It is in this overlap region, due to absorption and re-emission processes, that the quantum efficiency of the crystal is less than that of the molecule, and the mean lifetime of the fluorescence is longer than that of the molecular emission.

The response of the organic scintillators to the ionizing particles is a non-linear function of the particle's energy and is smaller for the more heavily ionizing particles when different types of particles are compared at a given energy. A semi-empirical formula was developed by Birks in 1951 to describe this phenomenon [Birk51]. Later, several improvements were made to this relationship to incorporate multi-component scintillators [Chou52], quenching by second-order processes, such as double de-exitation, or interaction of excited molecules, etc. [Blac53, Wrig53]. In the discussion that follows, we consider the original formula by Birks:

$$\frac{dL}{dx} = \frac{AdE/dx}{(1 + kBdE/dx)} \tag{4.1}$$

where dL/dx represents the scintillation photon emitted per unit length and BdE/dx is the density of quenching centers produced per unit distance by the incident particle. The specific fluorescence is reduced by a factor $(1 + kBdE/dx)$ due to the quenching process characterised by the parameter k. In the case of trans-stilbene, k is the unimolecular quenching parameter. A is the absolute scintillation efficiency of the crystal and dE/dx is, of course, the specific energy loss of the trans-stilbene.

If one makes a change of variables such that $S = L/A$, one avoids dependence on the measurement units of L. Thus,

$$\frac{dS}{dE} = \frac{1}{A}\frac{dL}{dE} = \frac{1}{(1 + kBdE/dx)}. \tag{4.2}$$

For electrons $\geq 125\,\text{keV}$, $dE/dx \approx 0$. So, $\frac{dS}{dE} = 1$ and $S = E_{electron}$. For protons of a few MeV, however, dE/dx cannot be neglected and this forces one to consider the quenching effects in calibration of the pulse amplitudes. Equation (4.2) can be numerically integrated to find S. However, dE/dx, the specific energy losses of trans-stilbene are required to perform this integration and such measurements were done by several authors [Hirs48, Whal58]. The following formula is used to compute the specific energy losses for protons [Crau70];

$$\frac{dE}{dx} = \frac{4\pi e^4}{m_e v^2}(n_H B_H + n_C B_C). \tag{4.3}$$

e is the electron charge; m_e is the mass of electron; v is the recoil proton velocity; B_H and B_C are the atomic stopping numbers for hydrogen and carbon, respectively. n_H and n_C

are the number of hydrogen and carbon atoms per gram, respectively. The quantities B_H and B_C are uncertain $\pm 10\,\%$ in the recoil energy range of .1 to 15 MeV. This uncertainty increases up to $\pm 25\,\%$ at higher energies, $\sim$ 30 MeV. Figure 4.3 shows the results of this integration for two values of kB.

In the Coulomb-Nuclear interference region, one measures the momentum transfer $|t|$ from the incident particle to the proton in the scintillator by reconstructing the track of the scattered proton. The kinetic energy of the recoil proton can be expressed as $T = |t|/2m_{proton}$. Thus, it is possible to make a correlation between the two experimentally independent quantities, i.e. the kinetic energy expected and the pulse amplitude recorded for the same event by the ADC's. It is difficult to rely on the measurement of the effective recoil energy due to the uncertainties in the atomic stopping numbers for hydrogen and carbon alone. However, this criterion, in principle, provides a tool for carbon background supression since $T_{carbon} \approx 1/12\, T_{hydrogen}$. This idea is discussed further in Chapter VI.

Figure 4.2.b schematically represents fast timing characteristics of a scintillating material with PSD properties. The total light output from the crystal can be parametrized as a simple sum of the fast and slow components, i.e.,

$$L(t) = L_f \exp(-t/\tau_f) + L_s \exp(-t/\tau_s). \tag{4.4}$$

τ_f and τ_s are the decay time constants and, L_f and L_s are the fitted coefficients for the fast and slow components, respectively. In principle it is possible to add more terms to account for different processes in the scintillation of the cystal, however equation (4.4) is sufficiently accurate for our purposes. The fast decay time constant, τ_f, is measured to be 4-6 ns and the slow decay time constant is $\geq$ 275 ns [Boll61, Kuch68]. By setting the

prompt and delayed gate widths according to the decay times, one can construct a PSD trigger as explained in the last section of this chapter.

Unfortunately directional dependence of scintillation response is not a well-studied phenomenon due to difficulties in uniquely defining the lattice axes of organic cystals and the non-linear response of the crystals to the radiation. Coon [Coon58] has observed significant variation in pulse height with direction in trans-stilbene. 14 MeV neutrons were incident on a trans-stilbene crystal 1/2 inch in diameter and 1/2 inch long. The angle between the cylindirical axis and the direction of the neutron beam was held constant and the azimuthal angle was varied by rotating the crystal around the symmetry axis. The observed pulse heights varied as much as 15%. Similar measurements on three other trans-stilbene crystals showed the same effect. Brooks et al. [Broo74] studied the same effect on several organic crystals. They define pulse height anisotropy A_L as

$$A_L = 2\frac{(L_2 - L_1)}{L_2 + L_1} \tag{4.5}$$

where L_1 and L_2 are the minimum and maximum observed values of $L(\theta, \phi)$. The PSD anisotropy A_S is defined by the following equation:

$$A_S = \frac{2\,(S_2 - S_1)}{(S_1 + S_2 - 2S_\gamma)}. \tag{4.6}$$

S_1 and S_2 are the proton PSD amplitudes at the orientations corresponding to the pulse heights L_1 and L_2 and S_γ is the gamma-ray PSD amplitude, that is the median value of the Compton electron group in the projected S spectra. So A_L is a measure of directional variation of the pulse height relative to the average pulse height and A_S is a measure of the directional variation of the PSD amplitude relative to the PSD separation of protons and

electrons. For 8 MeV neutrons, $A_L = 0.22$ and $A_S = 0.12$; and for 21.6 MeV neutrons $A_L = 0.09$ and $A_S = 0.29$ were measured. The similar measurements were made with protons at 1 and 3 MeV and the PSD anisotropy was found to be less than that of 8 MeV neutrons.

Light Collection System of Targets

Special light collection hoods were designed and built to optimize the collection of light emitted by the trans-stilbene targets (Figure 4.4). Each of the six targets had its own such unit. Individual targets were viewed by an XP2020 type photomultiplier with CERN type base and the targets were optically air-coupled. The design criteria were the following;

1. the best possible light collection efficiency,
2. minimum mass along the beam, except for the targets themselves, to minimize unwanted spurious interactions,
3. flexibility and modularity in design such that insertion and/or replacement of targets, PMT's and bases could be accomplished with acceptable reproducibility and speed without resurveying.

The crystals, with a thin lucite ring around them, were suspended from the top of the hoods with a thin ~1.8 cm long lucite rod. Typical distance from the center of the crystals to the photocathode of the PMT's was ~11.4 cm. The hood itself consisted of a 0.7 mm thin bakelite tube with 5 cm diameter holes cut out in the direction of beam. The holes were covered with an extremely thin, light-tight black sheet of PVC. A removeable disk to hold the targets was attached on top of the hood. On the bottom, a conical aluminum piece was made to guide the fluorescence light to the photocathode. The entire assembly fit together solidly and the tolerances of individual pieces were made and

measured to be within 100 microns. Inside the light collection assembly, several coats of barium sulfate was applied for effective light collection (Kodak White Reflective Coating, CAT No: 118-1759). This reflector is specified by the manufacturer to exhibit efficiencies above 98.9% at 400 nm, the mean fluorescence wavelength of trans-stilbene. We found that this particular reflector was 2-3 times more effective than the conventional aluminum foil in terms of pulse amplitudes at the PMT voltages of interest.

Target Veto Counters

The entire target ensemble was surrounded by 11 lead-scintillator sandwich veto counters to eliminate wide angle scattering and production processes (Figure 4.5). During the testing period prior to data-taking, the most effective veto counter was found to be the forward one, V11, reducing the trigger rate by 11.5% (Table 4.2). V11 was positioned normally to the beam direction, with a 4.7 cm hole in the middle of the counter which was centered around the beam. The size of the counter served to veto all events originating from the general target area except the events close to the beam.

Multi-Wire Proportional Chambers (MWPC)

For this measurement, 42 planes of multi-wire proportional chambers and 2 planes of multi-strip silicon detector (MSD) were used (Table 4.3). The MSDs (5 cm $\times$ 5 cm) had 100 micron strips and were located before the targets at $z = -171.8$ cm. All of the chambers were operated with the *magic gas* mixture. The typical mixing ratios for individual gases were 120 cc/min argon to the methylal bubbler at 0° C, 270 cc/min argon, 90 cc/min isobutane and 100 cc/min argon balanced with 2 % freon. The vapor pressure of methylal at 0° C was calculated to be $\sim$ 120 mm Hg. The input pressures of each individual gas component to the gas-mixing rack was about 0.70–0.75 bar. The smaller chambers were

flushed at $\sim$ 3 liters/hour and the larger chambers were flushed at rates of 7–15 liters/hour. The overall efficiency of the planes were typically 60% to 97% during data-taking.

Analysing Magnet BM-109

An analysing magnet (BM-109) was used to analyse the momentum of the particles. It was centered around $z = 15.00$ m and operated at 2500 amperes during data-taking. The magnet gap is 24" $\times$ 21" in x and y directions, respectively. The magnetic field was mapped using a Hall probe in the gap area along the beam direction. $\int B_y dz$ was calculated along the grid lines and found to be smooth in the central regions of the magnet [Nguy90]. Figure 4.6 shows the magnetic field strengths of the analysing magnet in four closely packed central regions. The magnetic field has a flat-top at 13.78 KGauss and remains constant along the beam direction throughout the magnet gap. The analysing magnet has a momentum kick of $\sim$ 0.4 GeV/c.

Gray Code Hodoscope

The Gray Code (GC) hodoscope was built by the Saclay group for the CNI and $\Delta\sigma_L$ measurements for E-704 [Arig85]. It consists essentially of two identical hodoscopes with vertical and horizontal scintillator strips, determining x- and y-coordinates of the transmitted particles, respectively. It is segmented into $2^5 = 32$ bins, each 5 mm wide (Figure 4.7). Each hodoscope is subdivided into *direct* and *inverse* sections, and each is viewed by a set of 5 PMTs. Two counters (16 cm $\times$ 16 cm) are placed immediately before and after the hodoscope.

One of the distinct features of the GC is that a straight track which is parallel to the beam axis traverses one and only one counter of each of the 10 complementary pairs, generating a 5-bit address, thus uniquely defining the particle's track in space. Naturally, due to the incoming particles' angle and gaps in the hodoscope, some fraction

of events will generate direct and inverse addresses that are not compatible; i.e. one or more direct/inverse pairs of bits will be *empty* or *double* or both. In this case, one or both of the direct/inverse addresses are spurious. In the fine-binned segments, $A - \bar{A}$, incompatibility (empty or double) may be acceptable because the ambiguity is between two adjacent bins of 5 mm strips. One can assign the border as the coordinate without much loss in the geometric resolution. If, however, such an incompatibility takes place for the rest of the larger segments, then the event must be rejected. Generally speaking, incompatible coding for the empty events is typically caused by gaps in the adjacent counters, PMT and electronics inefficiencies, etc. Whereas for double coding, the possible sources for inconsistent coding are overlap of the adjacent counters, oblique incidence of track, multiple tracks, interactions emitting charged particles, δ-rays, etc [Ross90].

Like binary code, the Gray code is based on the base-2 system. There are literally infinite number of Gray codes but the commonly used one is the non-weighted reflected Gray code used here. Although it has been employed for centuries, the first useful industrial application of it was realized by Frank Gray, from Bell Telephone Laboratories, in transmitting signals by pulse code modulation. The advantage this type of a code has over others is that only one bit changes from one number to the next, may it be increasing or decreasing. Because of this, error checking in rapid transmissions or coding is much more effective. Gray code can easily be generated from other codes. For example, given a binary number, one would shift the bits towards the right side, discard the least significant bit and add (exclusive **OR** operation) the binary number to it such that, $1+1=0, 1+0=1, 0+1=1, 0+0=0$. Apart from Gray code's use in transmission of signals, communications, computing and analog to digital conversion, there have been,

historically, many curious applications of this code, e.g. the celebrated Chinese ring puzzle. Table 4.4 shows the possible hit patterns and their binary equivalents for a given bin for the GC hodoscope.

Data Acquisition System and Trigger

The data acquisition system of all the experiments at E-704 is based on the CAMAC standard. Data from CAMAC crates (parallel and/or serial) are transferred via a Jorway interface to a PDP/11 computer, written on a 9-track magnetic tape and simultaneously transferred to a VAX workstation via the DR-11W data-link for on-line analysis. On-line monitoring of the experiment with the workstation proved to be highly efficient and valuable. When a *good* event is registered by the electronics, an interrupt (master trigger) is sent to the PDP/11 and the computer service is requested. Once the computer is finished with the tasks, it sends back a *reset* signal to the data acquisition electronics enabling the system for the next event. Event rates of $\sim$ 2000 per spill saturated PDP/11 and it was not possible to collect data at higher rates than this. During the final days of data-taking, live times of $\sim$ 50% were achieved by fine-tuning the electronics.

The trigger for the CNI polarimeter consists of two major parts. The first part, by exploiting the PSD characteristics of the active trans-stilbene targets, generates a GT* signal whenever there is a recoil candidate in one of the six targets. The second part, initiated by the GT*, signal checks the scattering and azimuthal angles of the event by using the GC and makes a decision based on the information loaded on the memory units (MLUs).

Figure 4.8 shows the simplified scheme of the first PSD part. Two signals from the same target arrive at the rack and one of them, after generating a gate at the high-impedence discriminator, is sent to ADCs downstream. The other signal is used to make

a decision for the recoil events. The signal is amplified and split into fast and slow parts. The fast part of the signal is gated by 30 ns and integrated, similarly, the slow part of the same signal is gated by 50 ns and integrated. The fast signal is inverted and summed with the slow part within the gate that is generated by the first pulse. If there is a recoil event at one of the targets, i.e. the large slow component, the gated sum module triggers a discriminator and the discriminator, in turn, triggers the rest of the system downstream. It typically takes 185 ns to make a PSD decision. The ADC's for the total and the slow components (130 ns gate width) are free running and the gate for the slow component is 35 ns delayed with respect to the total. If there is a good event, i.e. master trigger, then the ADCs are read and cleared.

The second part of the trigger (Figure 4.9) makes use of several signals that are combinations of different criteria [Leuh90]. They are;

GT* : (Good Target) a recoil candidate detected at one of the targets ($\sim$ 185ns),

SNK AND: (Snake And) at least one hit in four snake hodoscopes, no events in target defining veto counters, and no event in the second of the beam Cherenkov counters, $\overline{C_2}$, ($\sim$ 220ns),

GCTB: (Gray Code Transmitted Beam) transmitted beam at the GC ($\sim$ 262ns),

USB: (Usable Snake Beam) SNK AND $* \overline{C_1}$ and no more than two hits in snake hodoscopes ($\sim$ 250ns),

$TB * \bar{E}$: (Transmitted Beam and not Early) current particle is separated from preceding particle by at least 60 ns ($\sim$ 210ns),

$TB * \bar{E} * \bar{S}$: (Transmitted Beam, not Early and not Sampling) $TB * \bar{E}$ and tagging electronics is not latched to read out the tagging information ($\sim$ 255ns),

$TB * \bar{E} * \bar{L}$: (Transmitted Beam, not Early and not Late) $TB * \bar{E}$ and following particle is 60 ns later ($\sim$ 280ns),

GH: (Good Hit) a single hit in five hodoscopes (~ 320ns),

GOOD MOM: (Good Momentum) event within a momentum bit ± 9% (~ 365ns),

SNAKE GOOD HIT: USB and one and only one hit in snake hodoscopes (~ 300ns),

SBF: (Signal Bon Faisceau) one particle in accelerator bucket (~ 280ns).

The times indicated above and below in parantheses are the times that it takes for the signals to be formed with respect to a particle at $z = 0$. The elements of CNI polarimeter logic are constructed from the above signals in the following way (see Figure 4.9),

CNI 12: (GT*) * (SNK AND) * (GCTB), (~ 322ns),

CNI 13: (USB) * (TB $*\bar{E}*\bar{S}$), (~ 385ns),

CNI 14: (CNI 12) * (CNI 13), (~ 393ns),

CNI 15: (GH) * (TB $*\bar{E}*\bar{L}$), (~ 430ns),

CNI 16: (SBF) * (CNI 13), (~ 550ns),

CNI 17: (Master Trigger) = (MLU) * (CNI 19) * (GT LATCHED), (~ 830ns),

CNI 18: (CNI 12) * ($\overline{\text{CNI17}}$), (~ 845ns).

CNI 19: (GOOD MOM) * (CNI 15) * (CNI 16) * (SNAKE GOOD HIT), (~ 560ns).

MLU logic is designed such that it projects the undeflected beam track onto the GC and checks if the event meets the scattering requirements for θ and ϕ. MLUs are loaded with a *butterfly* cut (see Figure 6.11) to eliminate the up and down scattered particles and a 1.1 cm × 1.1 cm square is cut out in the center to eliminate the straight-through beam particles, thus only accepting particles that scatter left and right of the beam.

Table 4.1 Dimensions and locations of each target along the beam-line.

Target No	Thickness (mm)	Diameter (cm)	Z–Location (cm)	H.V. (kV)
1	2.0	3.0	−60.12	−2.30
2	2.0	3.0	−20.12	−2.23
3	3.0	3.0	19.88	−2.30
4	3.0	3.0	39.88	−2.25
5	5.0	3.0	59.88	−2.33
6	6.2	4.0	79.88	−2.20

Table 4.2 The reduction in trigger rate as measured for individual veto counters. Veto counters 1–8 are type XP2020 and 9–11 are EMI type PMTs.

Veto No	Reduction (%)	H.V. (kV)
1	3.9	−2.40
2	3.9	−2.35
3	5.4	−2.40
4	4.7	−2.40
5	3.0	−2.50
6	5.0	−2.40
7	3.2	−2.40
8	2.7	−2.30
9	5.4	−2.00
10	5.9	−2.00
11	11.5	−1.85

Table 4.3 List of the multi-wire proportional chambers used for this measurement. The identification names of each chamber, read-out electronics types, effective size (all chambers are the same size in x and y directions), wire spacings and the z locations along the beam-line are tabulated.

Name	Type	Size(cm)	Pitch(mm)	Z-Location(cm)
BK 1 Y	PCOS	9.60	1.0	−2414.3
BK 1 X	PCOS	9.60	1.0	−2413.1
BPC1 Y	RMH	9.60	1.0	−2352.8
BPC1 X	RMH	9.60	1.0	−2351.8
BPC2 Y	RMH	9.60	1.0	−513.8
BPC2 X	RMH	9.60	1.0	−512.8
BK 2 Y	PCOS	9.60	1.0	−216.3
BK 2 X	PCOS	9.60	1.0	−215.1
BPC3 Y	RMH	9.60	1.0	−197.3
BPC3 X	RMH	9.60	1.0	−196.8
PC1 V	RMH	9.60	1.0	245.7
PC1 Y	RMH	9.60	1.0	249.2
PC1 X	RMH	9.60	1.0	250.2
PC1 U	RMH	9.60	1.0	253.7
PC2 V	RMH	19.20	1.0	600.0
PC2 Y	RMH	19.20	1.0	603.5
PC2 X	RMH	19.20	1.0	604.5
PC2 U	RMH	19.20	1.0	608.0
BK 3 Y	PCOS	19.20	2.0	900.0
BK 3 X	PCOS	19.20	2.0	900.9
PC4' Y	RMH	51.20	2.0	1244.5
PC4' X	RMH	51.20	2.0	1246.5
PC5' Y	RMH	9.60	1.0	1310.5
PC5' X	RMH	9.60	1.0	1311.5
PC5" Y	RMH	19.20	2.0	1320.0
PC5" X	RMH	19.20	2.0	1321.0
PC5 V	RMH	51.20	2.0	1351.0
PC5 Y	RMH	51.20	2.0	1356.4
PC5 X	RMH	51.20	2.0	1358.8
PC5 U	RMH	51.20	2.0	1364.2

Table 4.3 Continued.

Name	Type	Size(cm)	Pitch(mm)	Z-Location(cm)
PC6 V	RMH	64.00	2.0	1648.1
PC6 Y	RMH	64.00	2.0	1653.5
PC6 X	RMH	64.00	2.0	1655.9
PC6 U	RMH	64.00	2.0	1661.3
PC7 Y	RMH	51.20	2.0	1744.5
PC7 X	RMH	51.20	2.0	1746.9
PC7' Y	RMH	51.20	2.0	1759.4
PC7' X	RMH	51.20	2.0	1761.9
PC13 T	PCOS	51.20	2.0	4549.0
PC13 U	PCOS	51.20	2.0	4551.4
PC14 Y	RMH	51.20	2.0	4587.0
PC14 X	RMH	51.20	2.0	4589.4

Table 4.4 Possible hit patterns and their binary equivalents for the GC for a given bin. The last two columns show direct and inverse address coding.

Bin No	Binary Code	Gray Code Direct	Gray Code Inverse
Counter		*EDCBA*	*EDCBA*
0	00000	00000	11111
1	00001	00001	11110
2	00010	00011	11100
3	00011	00010	11101
4	00100	00110	11001
5	00101	00111	11000
6	00110	00101	11010
7	00111	00100	11011
8	01000	01100	10011
9	01001	01101	10010
10	01010	01111	10000
11	01011	01110	10001
12	01100	01010	10101
13	01101	01011	10100
14	01110	01001	10110
15	01111	01000	10111
16	10000	11000	00111
17	10001	11001	00110
18	10010	11011	00100
19	10011	11010	00101
20	10100	11110	00001
21	10101	11111	00000
22	10110	11101	00010
23	10111	11100	00011
24	11000	10100	01011
25	11001	10101	01010
26	11010	10111	01000
27	11011	10110	01001
28	11100	10010	01101
29	11101	10011	01100
30	11110	10001	01110
31	11111	10000	01111

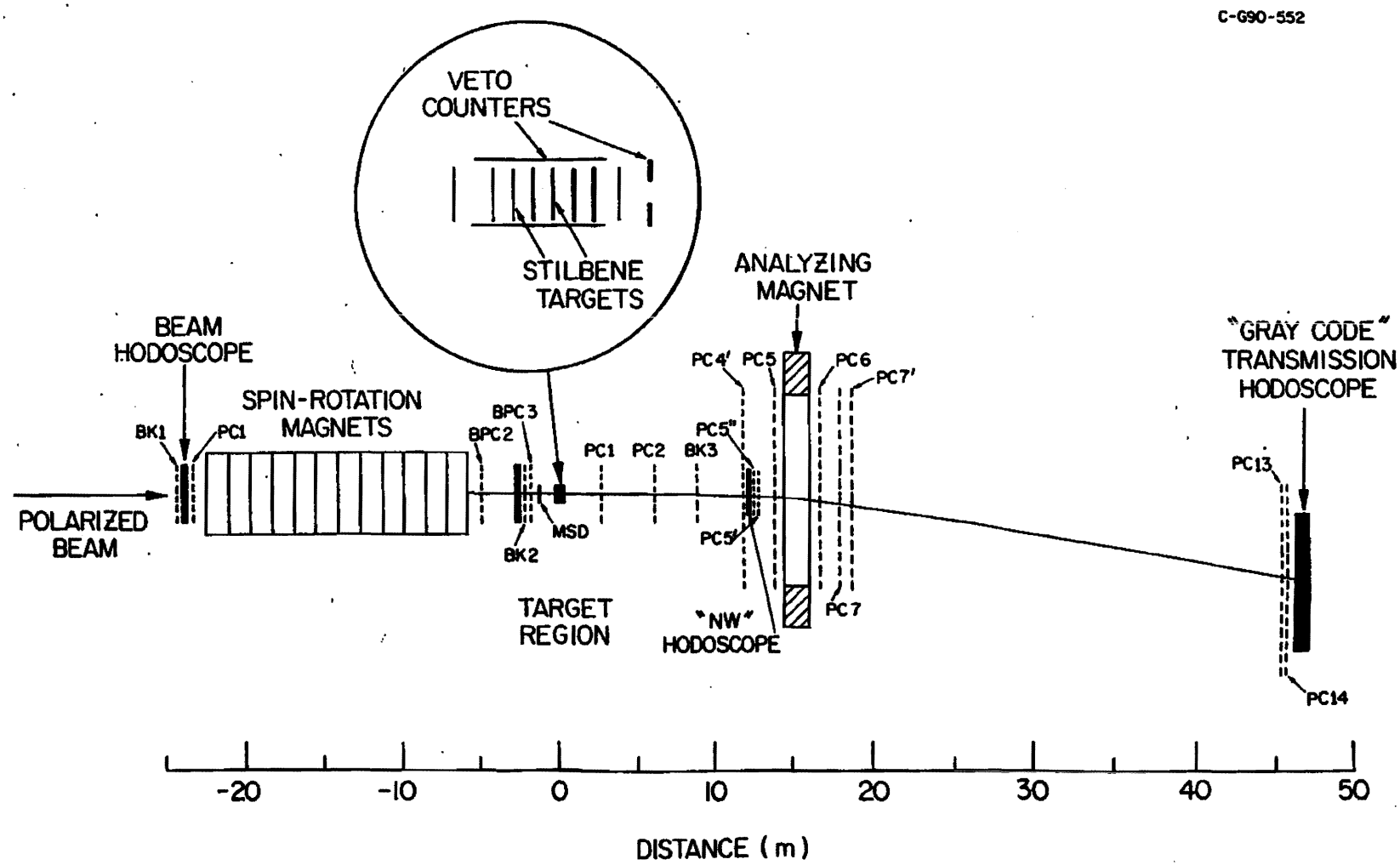

Figure 4.1 Top-view layout of the CNI polarimeter. The dimensions transverse to the beam are not to scale.

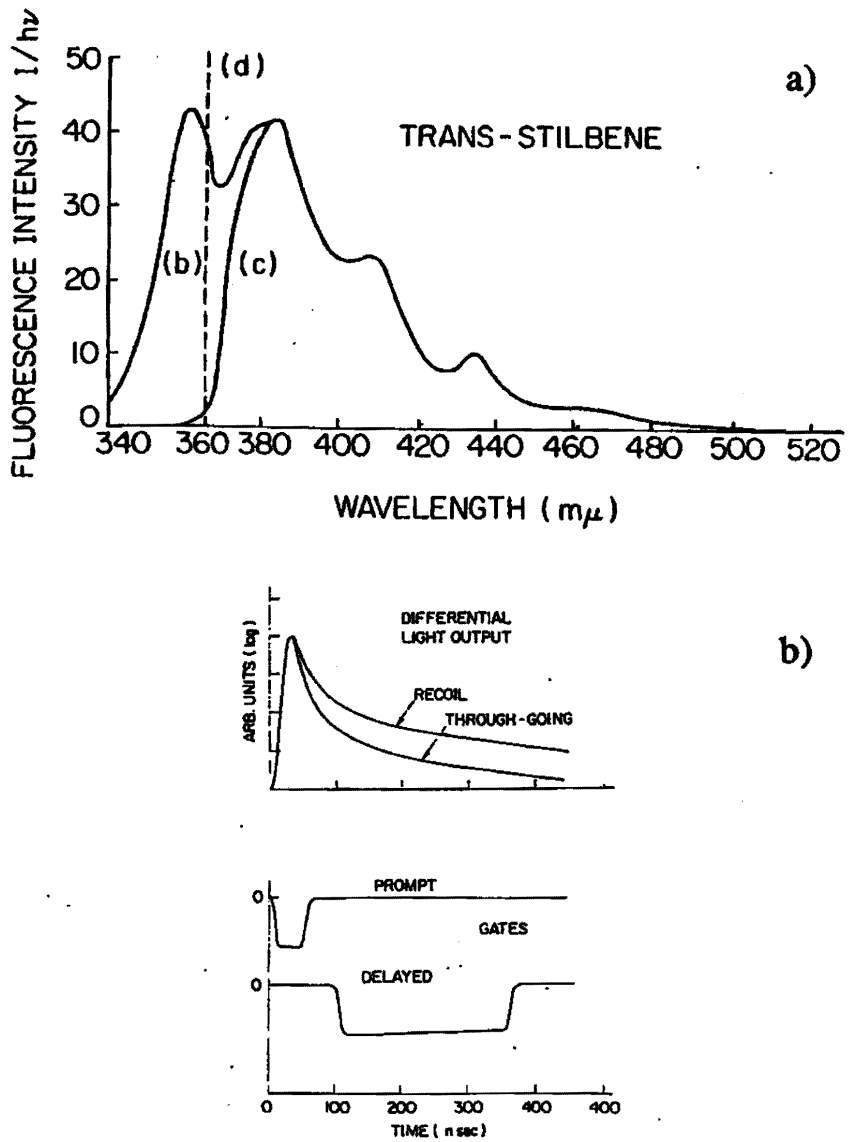

Figure 4.2 The fluorescence and PSD characteristics of trans-stilbene. a) The fluorescence spectra of trans-stilbene for 1 cm^3 crystal [Birk54]. The spectra that are shown are measured under a set of different conditions: (b) reflection from a thick crystal, (c) transmission through a 1 cm crystal, and (d) short wave-length limit mark for the transmission spectrum of trans-stilbene. The molecular fluorescence spectrum where (b) overlaps with (d) is removed from the transmitted spectrum. b) PSD charactersictics of trans-stilbene. The recoil particles generate a pulse with longer and higher tails compared to the minimally-ionizing particles. By choosing appropriate gates, this characteristic of the crystal is exploited to distinguish recoils from beam particles.

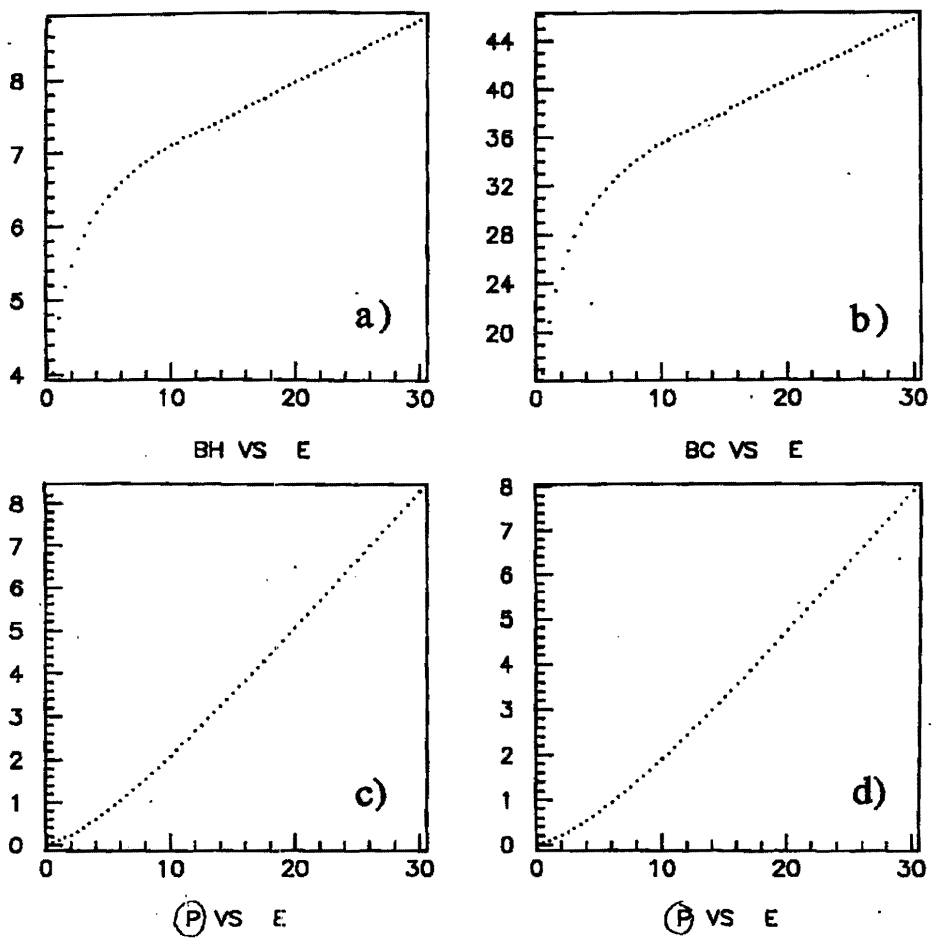

Figure 4.3 Atomic stopping numbers for hydrogen and carbon, and relative light outputs of trans-stilbene. a) Atomic stopping number for hydrogen and b) for carbon as a function of recoil energy [Hirs48]. c) Relative light output for $kB = 0.010$ and d) for $kB = 0.012\text{gr}/(\text{cm}^2\text{MeV})$ (see equation (4.2)).

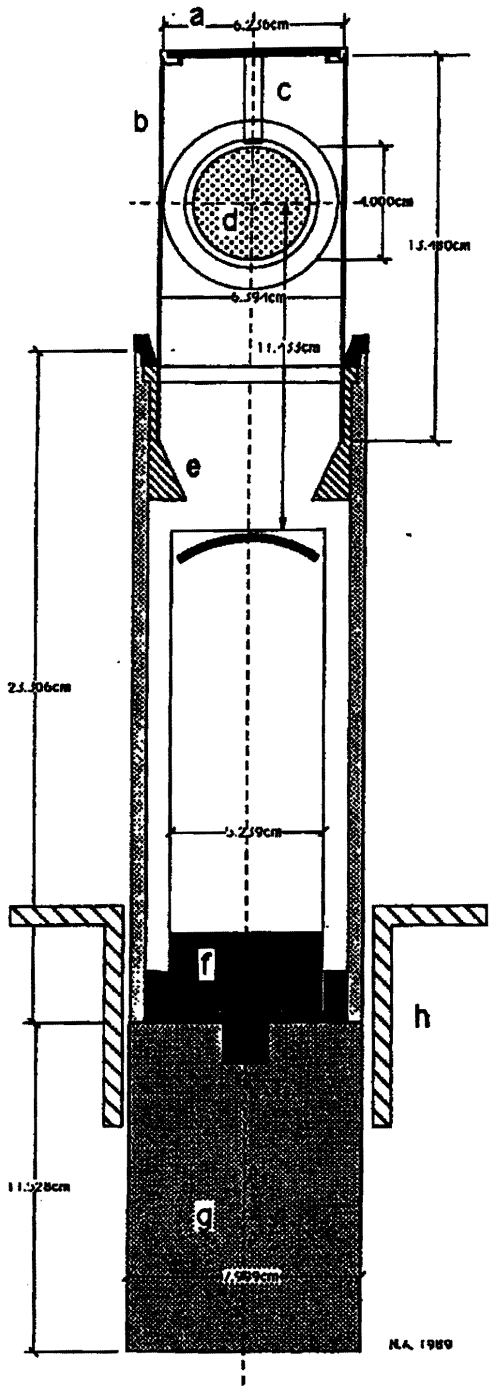

Figure 4.4 Cross-section of an individual target assembly, (a) aluminum disk where the target is attached, (b) bakelite tube, (c) lucite rod from which the target is suspended, (d) trans-stilbene target, (e) conical guide, (f) type XP2020 PMT, (g) CERN type base and (h) target table. Beam direction is into paper.

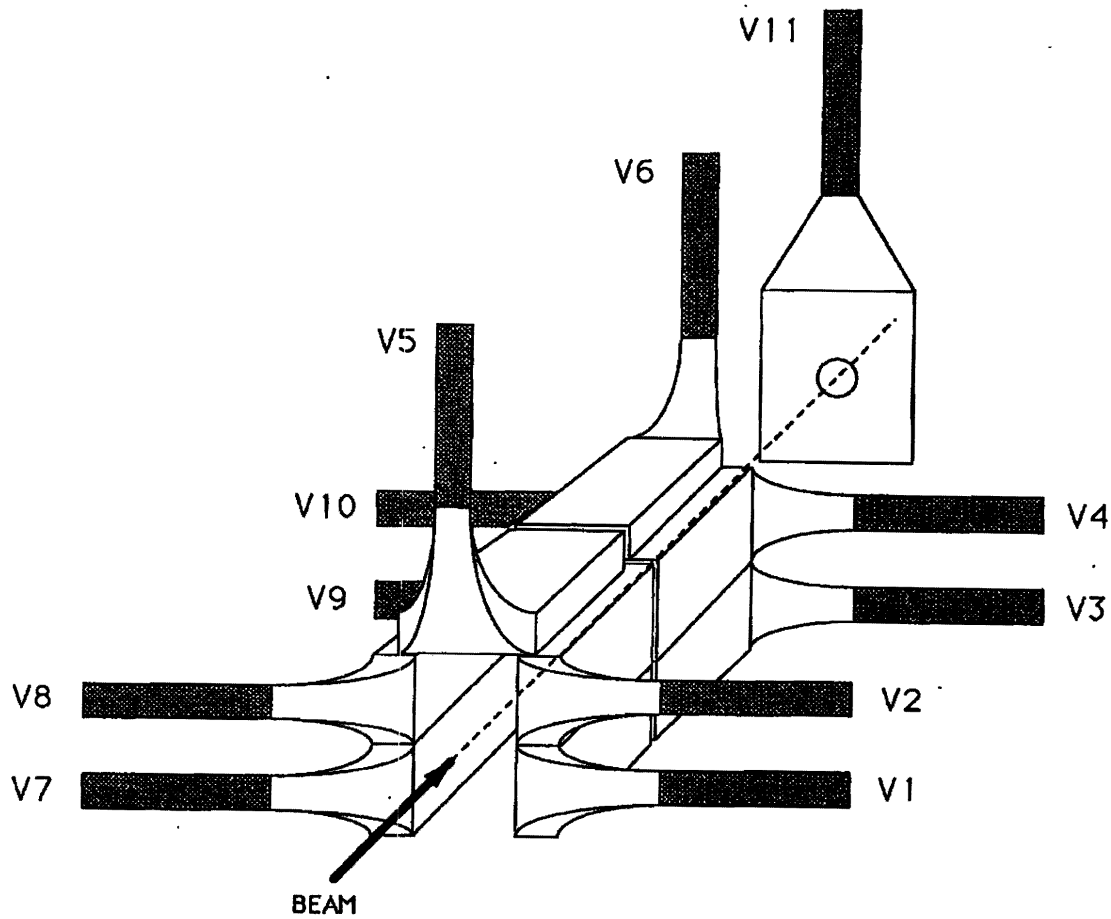

Figure 4.5 Veto counters around the CNI target assembly. Each veto counter consists of a lead-scintillator sandwich.

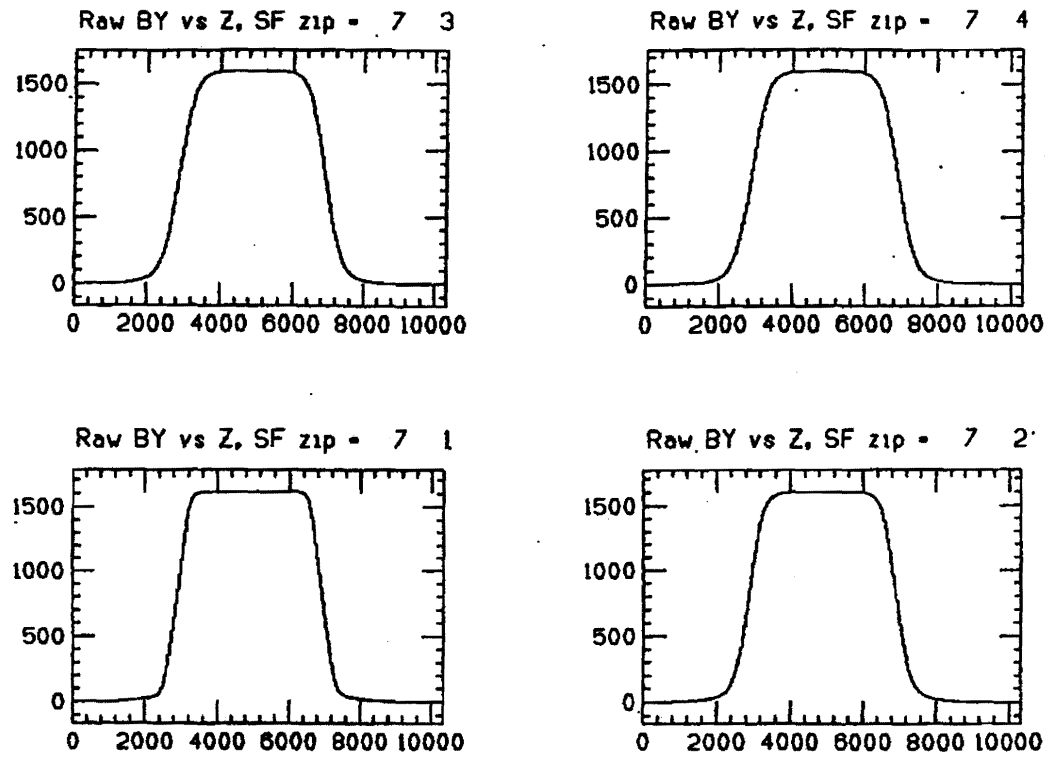

Figure 4.6 The magnetic field strength of BM-109 in the central region of the magnet gap. The flat-top occurs at 13.78 KGauss. The numbers on the axes are in un-normalized arbitrary units.

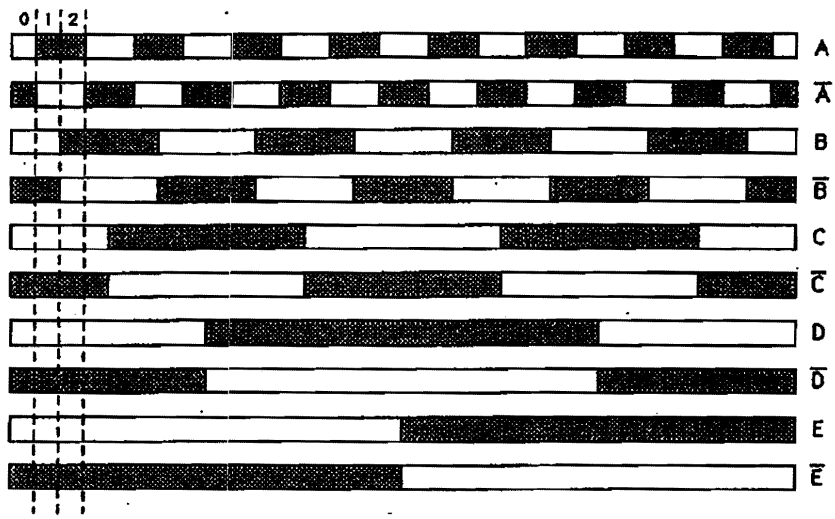

Figure 4.7 Cross-section of one of the hodoscopes of the GC. The shaded areas represent the scintillating material. Bins 0, 1 and 2 are shown as examples to illustrate the binning structure. 16 cm × 16 cm transmission counters are not shown.

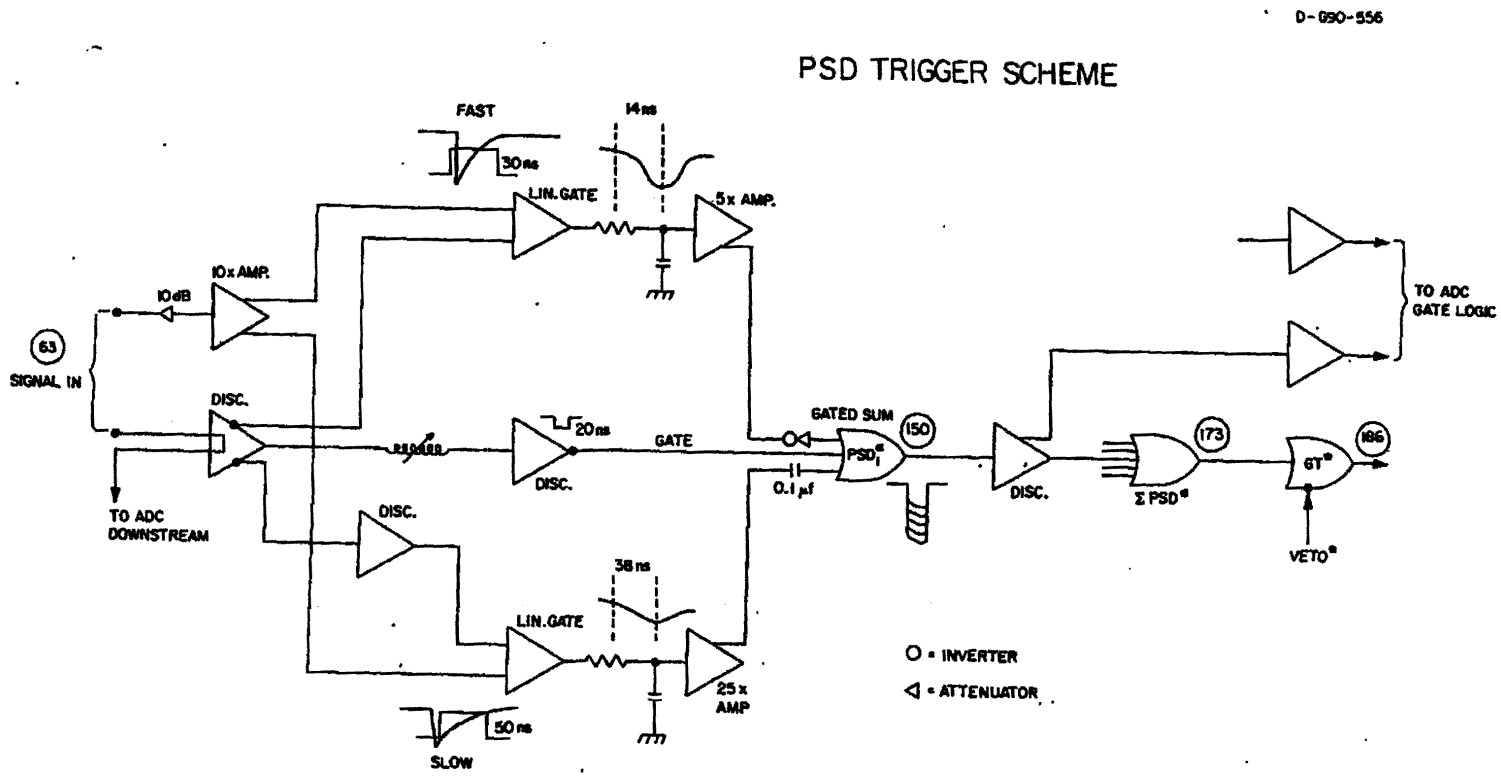

Figure 4.8 Simplified PSD trigger. The times of propagation of signals are indicated by the numbers in circles.

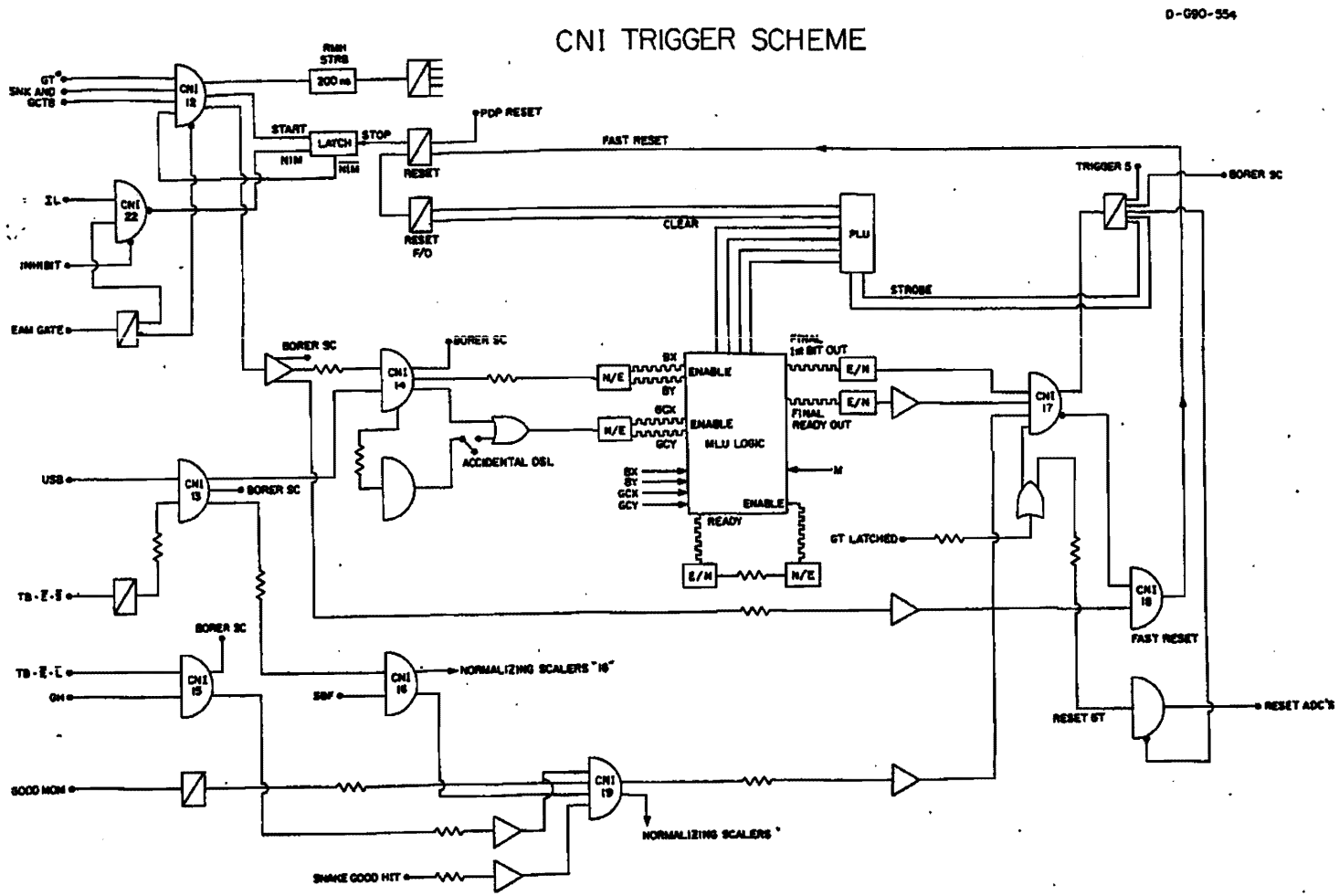

Figure 4.9 Schematics of the CNI trigger for the downstream part of the electronics.

CHAPTER V

KINEMATICS OF COULOMB-NUCLEAR INTERFERENCE AND EXPERIMENTAL CONSIDERATIONS

In this chapter purely, kinematical characteristics and the related experimental considerations are given for small-angle elastic nucleon-nucleon scattering processes. Features of the CNI polarimeter are discussed in light of these arguments [Penz78].

Kinematics of Elastic *pp* Scattering at Small Angles

One of the most significant parameters that must be measured is the invariant four-momentum transfer squared t in elastic nucleon-nucleon scattering.

$$\begin{aligned} t &= (\tilde{p}_o - \tilde{p}_i)^2 \\ &= (\tilde{p}_{recoil} - \tilde{p}_{target})^2 . \end{aligned} \tag{5.1}$$

The subscripts o and i stand for outgoing and incoming nucleons, respectively. The tilde indicates four-vector, $\tilde{p} = (E, \vec{p})$. Assuming that the target proton is at rest ($\vec{p}_t = 0$), and the scattering process is proper ($M = m_t$), we introduce the recoil kinetic energy $T_r = E_r - M$, (see Figure 5.1),

$$
\begin{aligned}
t &= (\tilde{p}_r - \tilde{p}_t)^2 \\
&= [(E_r, \vec{p}_r) - (m_t, \vec{0})]^2 \\
&= (E_r - M)^2 - |\vec{p}_r^{\,2}| \\
&= E_r{}^2 + M^2 - 2E_rM - E_r{}^2 + M^2 \\
&= 2M(M - E_r) \\
&= -2MT_r.
\end{aligned}
\tag{5.2}
$$

The above equation provides a simple relationship between the four-momentum transfer and the recoil kinetic energy of the target proton (Figure 5.2). It is relativistically exact and valid for any incident momenta. Thus the experimental error in the determination of t is directly proportional to the experimental error in T_r, assuming that M is known to a high degree of accuracy, i.e.,

$$|\Delta t| = 2M|\Delta T_r|. \tag{5.3}$$

The absolute measurement of T_r is difficult in the case of active targets (as is the case for CNI) due to straggling in the target material and the quenching effect in the scintillators. Thus, as an additional constraint, the scattering angle of the forward particle, θ_s, is measured with the forward spectrometer. In elastic scattering at small-angles, t can be approximated by (Figure 5.3)

$$-t \approx (p_i\theta_s)^2, \qquad \text{if} \quad \theta_s \ll 1. \tag{5.4}$$

If the momentum of the incident particle is known to a good accuracy, then the associated error in t will be

$$|\Delta t| \approx 2{p_i}^2\theta_s\Delta\theta_s \approx 2p_i\sqrt{|t|}\Delta\theta_s. \tag{5.5}$$

The error in four-momentum squared $|\Delta t|$, at constant p_i and t, grows as $\Delta\theta_s$ does. However, at higher beam momenta p_i, the error in t increases. As mentioned before, if t is determined from T_r only, such a dependence on p_i disappears.

The relationship $t = -2MT_r$ is valid whether the reaction is elastic or inelastic, provided that $M = m_t$. If the reaction is an inelastic one, then equation (5.4) is modified.

$$-t \approx (\frac{{m_o}^2 - {m_i}^2}{2p_i})^2 + (p_i\theta_s)^2 \tag{5.6}$$

where θ_s is now the polar angle of the center-of-mass motion of the produced system. If $({m_o}^2 - {m_i}^2)^2$ is small compared to $(2p_i)^2$, and m_o is well-determined from the measurement of the produced particle four-vectors, equation (5.5) is still a good estimate of $|\Delta t|$. However, θ_s is larger in inelastic scattering compared to the elastic ones since it must be calculated from the measured direction and momenta of several particles.

From kinematical considerations only we can conclude that the determination of t from T_r is more precise than the determination from θ_s when the incident momentum gets large. This is even more so as shown by equation (5.6) if the process is inelastic.

In elastic scattering, t can be calculated either from T_r or θ_s, provided that m_t and the four-vector $\tilde{p}_i$ are known. T_r and θ_s are thus related to each other in an elastic reaction, and they are also related to the recoil scattering angle, θ_r.

In inelastic scattering ($m_o > m_i$, but $M = m_t$), one of the essential parameters is the rest mass of the produced system. If m_t and $\tilde{p}_i$ are known, this mass is calculated

by four-vector balance from the measurement of the recoil four-vector. Expressed in the recoil measurement variables,

$$\begin{aligned} m_o{}^2 = p_o{}^2 = E_o{}^2 - p_o{}^2 &= (E_i + E_t - E_r)^2 - (\vec{p}_i - \vec{p}_r)^2 \\ &= E_i{}^2 + m_t{}^2 + E_r{}^2 + 2E_i m_t - 2E_i E_r - 2m_t E_r \\ &\quad - |\vec{p}_i^{\,2}| - |\vec{p}_r^{\,2}| + 2|\vec{p}_i||\vec{p}_r|\cos\theta_r \\ &= m_i{}^2 - 2T_r(E_i + M) + 2|\vec{p}_i|\sqrt{T_r(2M + T_r)}\cos\theta_r. \end{aligned} \tag{5.7}$$

Since $m_o{}^2$ is derived as the mass-squared needed to establish four-vector balance, m_o is generally called the *missing mass*. If M and $\tilde{p}_i$ are known with negligible errors, then $m_o{}^2$ can be determined from a measurement of T_r and θ_r. Differentiating equation (5.7), assuming $T_r \ll M$, we obtain

$$\begin{aligned} \Delta(m_o)^2 &= 2m_o\Delta m_o \\ &\approx [2(E_i + M) + |\vec{p}_i|\sqrt{2M/T_r}\cos\theta_r]\Delta T_r \\ &\quad + (2|\vec{p}_i|\sqrt{2MT_r}\sin\theta_r)\Delta\theta_r. \end{aligned} \tag{5.8}$$

In most practical cases, the first term is negligible and it is the magnitude of $\Delta\theta_r$ that determines $\Delta(m_o)^2$. An interesting feature of the above equation (5.8) is that the missing-mass error is dependent on the beam momentum $\tilde{p}_i$, unlike the in error t, and grows linearly with $\tilde{p}_i$.

The polar angle of recoil from equation (5.7) may be expressed as

$$\cos\theta_r = \frac{E_i + M}{p_i}\sqrt{\frac{T_r}{2M + T_r}} + \frac{m_o{}^2 - m_i{}^2}{2|\vec{p}_i|\sqrt{T_r(2M + T_r)}}. \tag{5.9}$$

The second term vanishes in the case of elastic processes (Figure 5.4). Since at high energies $E_i \approx p_i \gg M$, and since the low-energy recoils, as is the case for CNI, have kinetic energies in the order of several MeV, i.e. $T_r \ll M$, $\cos\theta_r$ is much smaller than

unity. Therefore $\theta_r \approx \pi/2$, i.e. the recoil protons scatter in close to perpendicular angles to the incident beam direction. $\cos\theta_r$ in the inelastic case, is larger due to the contribution from the second term of equation (5.9), but for smaller masses and high energies ($m_i \leq m_o \ll E_i$), θ_r is still close to $\pi/2$. This has a practical importance when performing recoil measurements with spectrometers, since it implies that the detectors can be positioned away from the beam direction, thus reducing the background from through-going beam particles.

Thus the critical inter-relations between T_r, θ_s and θ_r for elastic scattering are

$$\cos\theta_r = \frac{E_i + M}{p_i}\sqrt{\frac{T_r}{2M + T_r}}, \tag{5.10}$$

$$\cos\theta_s = \frac{p_i^2 - T_r(E_i + M)}{p_i\sqrt{(E_i - T_r)^2 - m^2}}. \tag{5.11}$$

There is an additional relation which requires co-planarity of the scattering and recoil particles, i.e. $\phi_{scattered} = \phi_{recoil} - \pi$. Naturally, the forward scattering angle $\phi_{scatterd}$ is measured for any polarimeter to be able to calculate asymmetries, but ϕ_{recoil} is much more difficult to measure since the recoil particles in general have energies of only a few MeV. In CNI, ϕ_{recoil} was not measured due to the geometry and nature of the active targets where most of the recoils stop and deposit all of their energy.

Experimental Method

In order to make the most restrictive selection of the *pp* elastic events, the following criteria are considered,

1. determination of slow recoil proton in the active target,
2. reconstruction of the forward proton track using the forward spectrometer,

3. no events in any of the veto counters.

The active trans-stilbene targets register the presence of a recoil proton when a certain pulse amplitude is generated which is above some suitable threshold. This means that $T_r \propto |t|/2M$ condition is satisfied. The advantages of this technique are

1. background rejection at the trigger and off-line level,
2. energy independence of recoil events, and
3. relative definition of T_r.

There are, however, other processes that take place in the active targets which tend to complicate the signature of pure pp elastic scattering.

1. Coulomb scattering from carbon: The differential cross-section for these events is given by

$$\frac{d\sigma}{dt} \approx \frac{4\alpha^2\pi}{t^2} Z^2 + \frac{\sigma^2_{TOT,C}}{16\pi} \exp\left(R_C/2\right)^2 t \tag{5.12}$$

where $\frac{\sigma^2_{TOT,C}}{16\pi} \approx 6 \times 10^3\,\mathrm{mb/GeV^2}$ and $(R_C/2)^2 \approx 67.6\,\mathrm{GeV}^{-2}$.

2. Quasi-elastic scattering from bound nucleons:

$$\frac{d\sigma}{dt} \approx \frac{\sigma^2_{TOT}}{16\pi} e^{bt} \left(1 - e^{Bt}\right) . \tag{5.13}$$

where $B \approx \frac{5}{2} \approx 25\,\mathrm{GeV}^{-2}$.

3. Inclusive processes on carbon:

$$\left(E\frac{d\sigma}{dp^3}\right)_A \approx A^\alpha \left(E\frac{d\sigma}{dp^3}\right)_{Nucleon} \tag{5.14}$$

where α is approximately 0.7.

The Coulomb scattering cross-section from carbon, at momentum transfer of 3×10^{-3} (GeV/c)^2, where Coulomb-nuclear interference is maximum, is about 50 times higher then that of pp cross-section. These events are rejected on the basis of the recoil energy-scattering angle relationship. Since the carbon nucleus is 12 times more massive than hydrogen, the recoil carbon nucleus produces a smaller pulse in the target for a given scattering angle, θ_s.

The quasi-elastic events are considerably depressed at low $|t|$ region. They generate a broad spectrum due to the Fermi motion of the target particles. This can be subtracted off-line.

The precision of track reconstruction depends on the quality of the forward spectrometer. The spectrometer defines the tracks and measures the momenta of the scattered protons. The elastic events must satisfy the momentum-loss constraint, i.e.,

$$p \approx p_o - \frac{{p_o}^2 {\theta_s}^2}{2m} \tag{5.15}$$

where $10^{-3} \leq (\theta_s p_o)^2 \leq 10^{-2}(\mathrm{GeV/c})^2$.

The factors that determine the precision of the forward spectrometer are the multiple scattering of the forward particles, the measurement accuracy of the wire chambers and the uniformity (momentum kick) of the analysing magnet.

The multiple scattering events are due to the elastic Coulomb interactions of the forward particles with the material in the beam. This can be calculated as follows,

$$\Delta\theta_{ms} = \frac{14.1}{p}\sqrt{L/L_R}(1 + 1/9 \log_{10} L/L_R). \tag{5.16}$$

where p is the particle momentum in GeV/c and $\Delta\theta_{ms}$ is in milliradians. L is the length of the material in the beam and L_R is the radiation length of the material. Since in Coulomb-nuclear interference the angles of scattering are in the order of fractions of milliradians, it is important to minimize the mass in the beam, e.g. He bags, vacuum pipes. The total amount of material in the beam for our measurement resulted in $\Delta\theta_{ms} \approx 0.21$ milliradians which is significantly larger than what was desired.

The measurement error, $\Delta\theta_{me}$, can be estimated in the following way;

$$\Delta\theta_{me} = 0.82\frac{S}{D} \tag{5.17}$$

where $\Delta\theta_{me}$ is in millirads, S is MWPC wire spacing in mm and D is the lever arm of the spectrometer in meters. For a 2mm MWPC at 50 meters the measurement error is about 0.033 milliradians, similar to what we expect from the CNI polarimeter.

The fractional accuracy of the analysing magnet is written as

$$\frac{\Delta p}{p} = 0.003\frac{p\Delta\theta}{BL}. \tag{5.18}$$

The momentum of the beam p is in GeV/c, $\Delta\theta$ is in milliradians and BL is expressed in Tesla meters. In the case of CNI, $\frac{\Delta p}{p}$ is estimated to be about 1%.

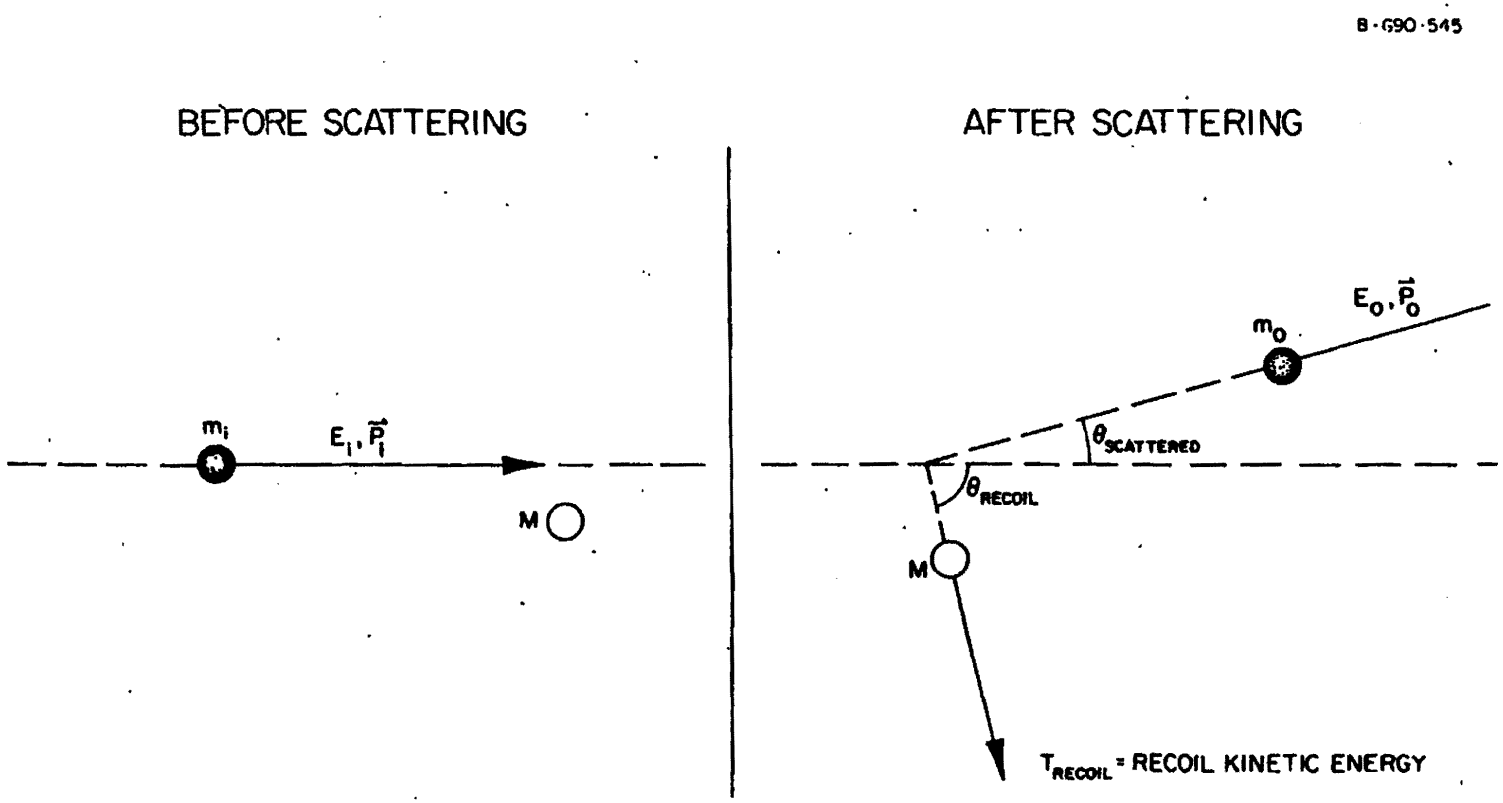

Figure 5.1 Schematic representation of small angle elastic scattering before and after the impact.

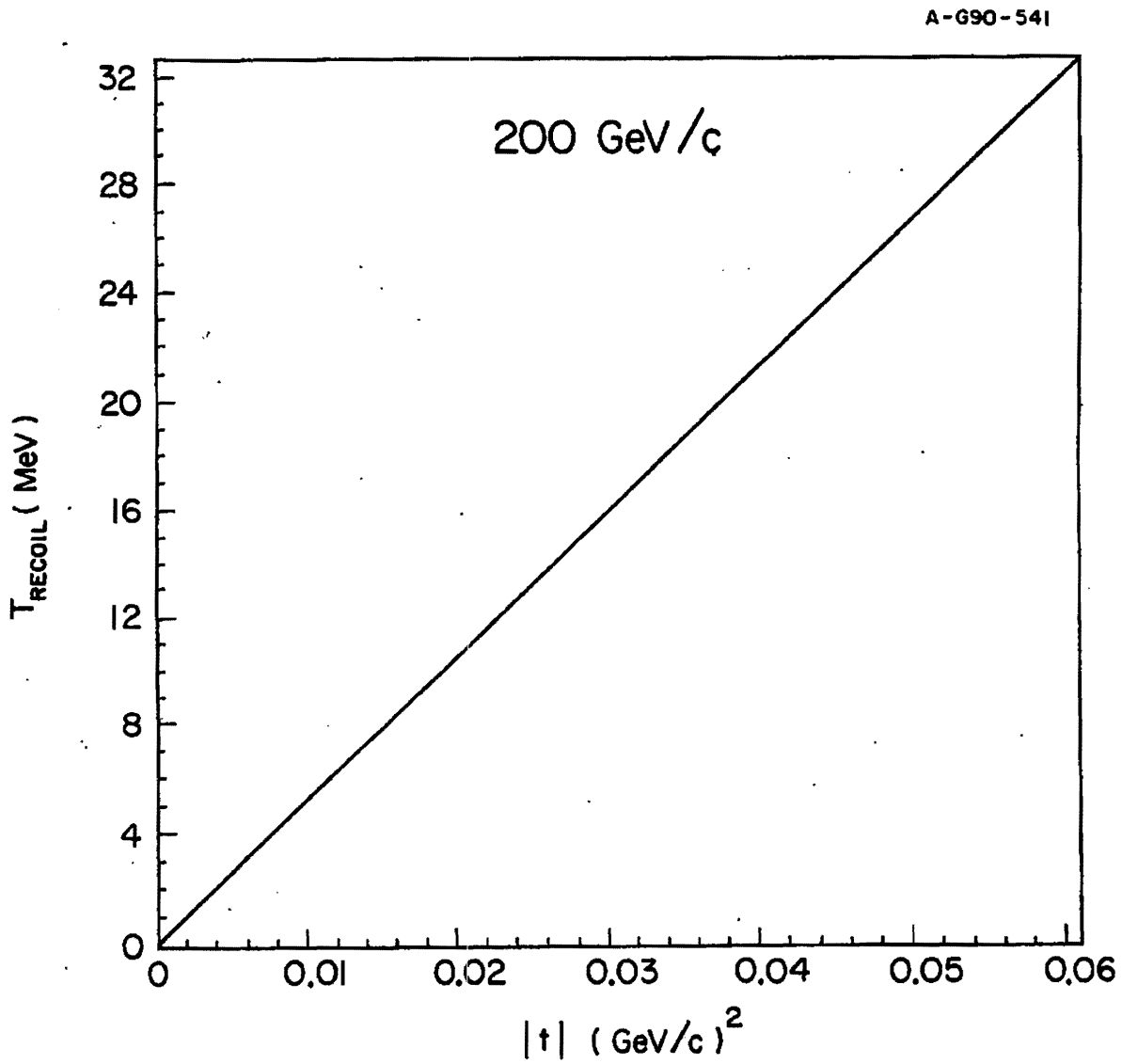

Figure 5.2 The kinetic energy of the recoil proton as a function of four-momentum transfer for elastic small angle scattering.

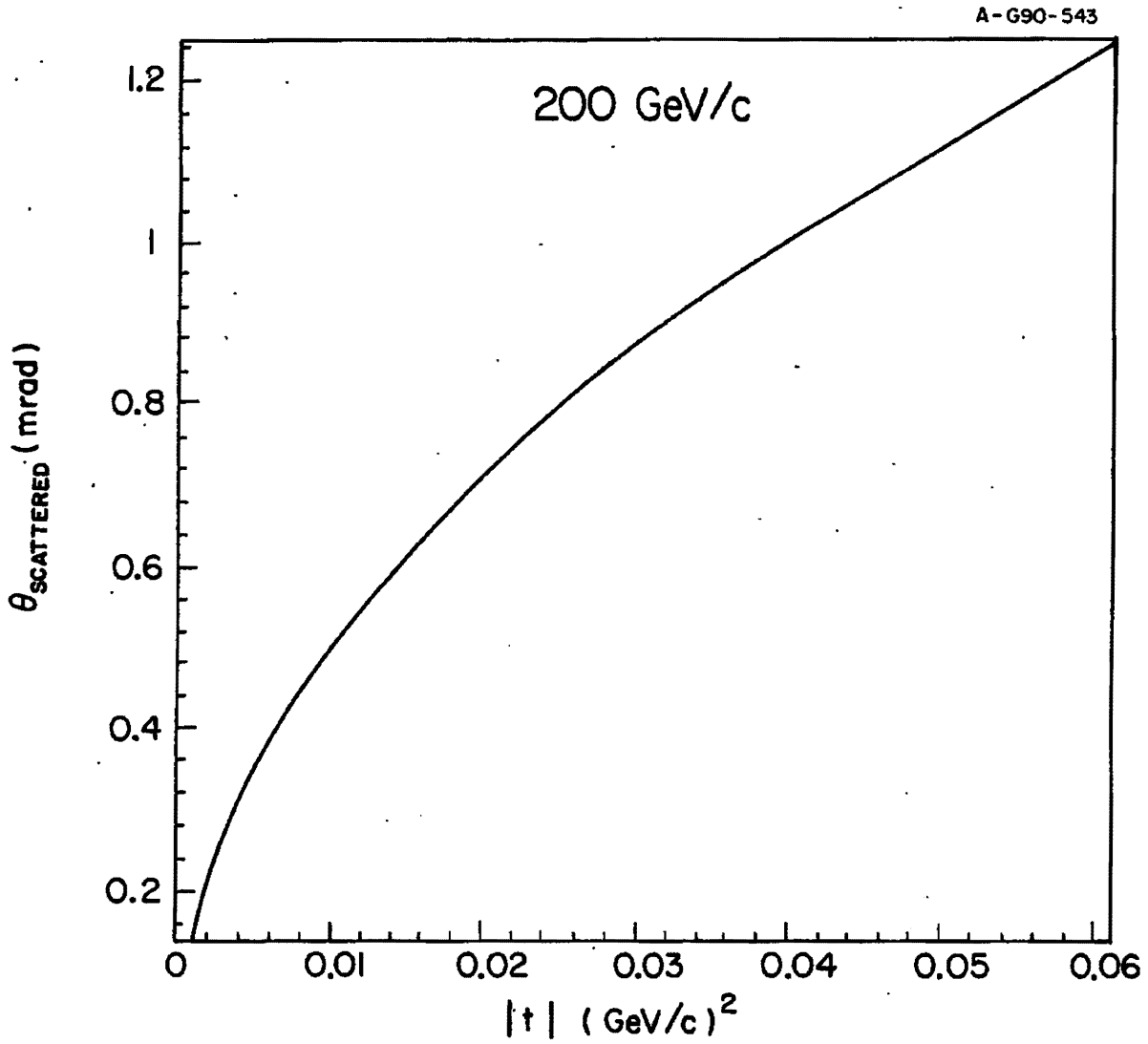

Figure 5.3 The scattering angle θ_s of the forward proton as a function of four-momentum transfer for elastic small angle scattering at 200 GeV/c.

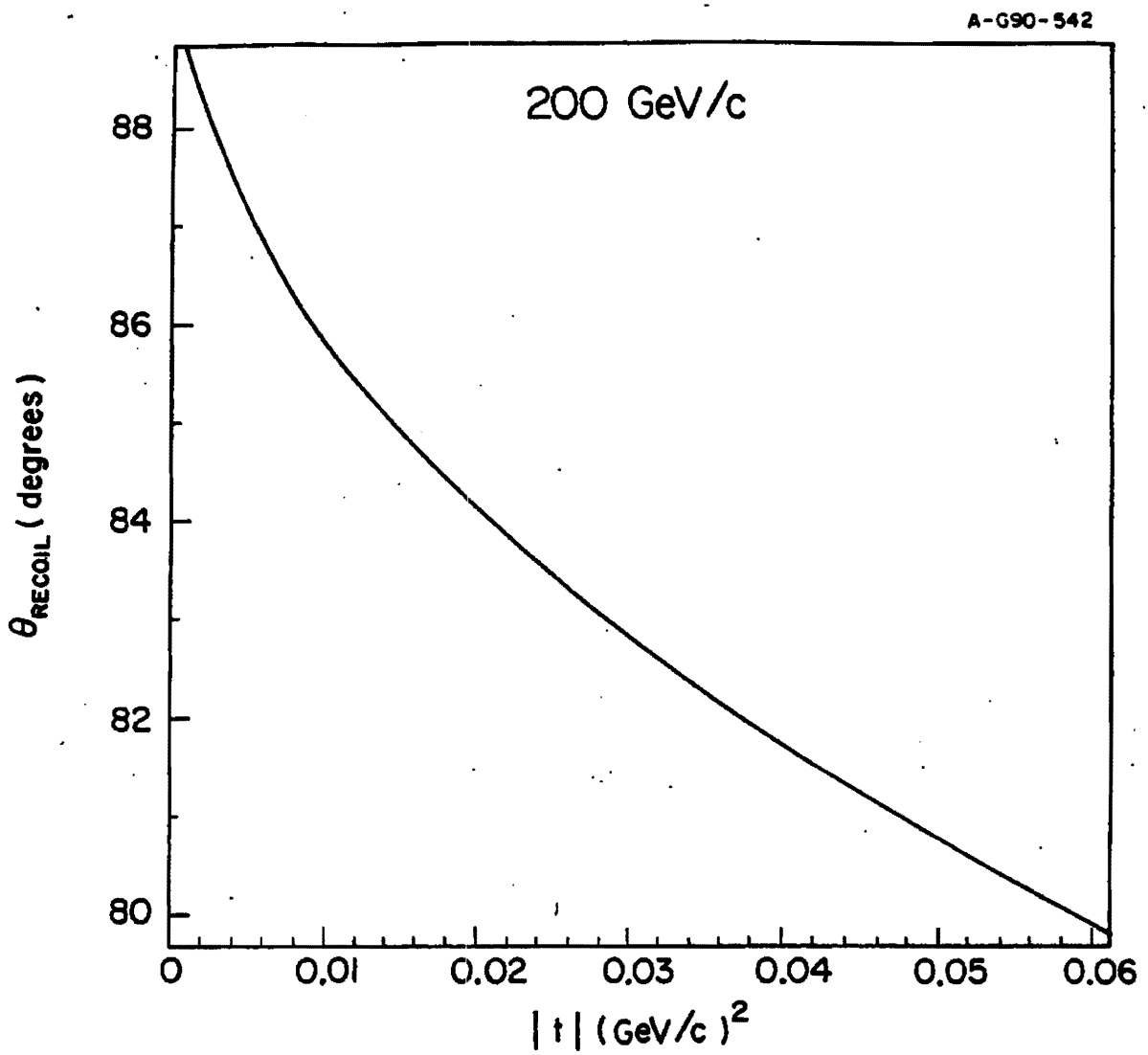

Figure 5.4 The recoil angle θ_r of the target proton as a function of four-momentum transfer for elastic small angle scattering at 200 GeV/c.

CHAPTER VI

ANALYSIS, RESULTS AND DISCUSSION

There is a limited number of measurements in the Coulomb-nuclear interference region and most of these measurements are done in lower energies at Los Alamos, Serpukhov and Saclay compared to Fermilab energies. The work described here is the first comprehensive measurement of the *pp* analysing power at high beam momenta (185 and 200 GeV/c) using a multi-scintillator active target in the CNI region. It is argued that a polarimeter based on the interference of Coulomb and nuclear forces can be a polarimeter of choice at higher energies because of the nature of the underlying process and the merits of the experimental setup. In this chapter the current results of the CNI measurements are given and discussed in some detail.

Data Analysis

The off-line data analysis is performed on various types of VAX computers and the analysis code consists of over 7000 lines of FORTRAN not including the general purpose utility programs. The raw data tapes were copied into 8 mm helical-scan video tapes and then data-summary-tapes (DSTs) were produced. About 45 % of the events survived this reduction process. After the final analysis, 25 % of the DST events proved to be acceptable. The number of good events is 243,365 for all of the targets, for the results reported here. The rejected events are mainly due to bad chamber efficiency, high multiplicity, indefinite snake state and inconsistent information from the hodoscopes.

Figure 6.1 shows the general structure of the analysis code. The main program calls several subroutines for different tasks. First, the chambers (wire spacings, z-locations, rotations, shifts) and the histograms (histogram numbers, size, etc.) are initialized. Then, on an event-by-event basis, several subroutines are run. The information from the hodoscopes, ADCs and the chambers is decoded; necessary calculations are performed and checked for consistency. After the particle's track is reconstructed, a table for asymmetry calculations is filled. This process is continued until all of the events are processed. The asymmetry calculations are carried out, employing different methods, by using the aforementioned table – a function of $|t|$ and ϕ bins, the beam polarization, the snake state and the target number. Several book-keeping routines are called for histograms, statistics, CPU consumption, etc. at the end of the program.

Vertex Reconstruction

Vertex reconstruction of the tracks determines two of the critical parameters of the measurement, i.e. scattered angle θ_s and the azimuthal angle ϕ for the scattered particle. In addition to the beam hodoscopes upstream of the target area and the GC at the end of the beam-line, there are 42 planes of MWPCs and two planes of MSDs to reconstruct the tracks. In off-line vertex analysis, the hodoscopes are mainly used to define a volume in which the tracks are reconstructed. This procedure saves significant time in computing. The reconstruction is done in three different stages; the incident track before the targets, the scattered track after the targets and the deflected track after the analysing magnet. The track is reconstructed for each segment and at the intersection points (target and the analysing magnet) the distance between the tracks is minimized. The maximum allowed distance is 2 millimeters in the x-direction. Figure 6.2 shows the z-vertex reconstruction of all of the events before and after cuts. The peak on the left for the upper distribution is

due to the events that originate from the beam hodoscopes and the MSDs just upstream of the target area. The lower distribution is the reconstructed z-vertex after the geometric and kinematic cuts.

The CNI trigger requires only that one of the targets be hit and until the event is fully processed the data acquisition system is latched. In this way the reconstruction of the z-vertex distribution for each target is possible. Figure 6.3 is the distribution of events as a function of the z-axis for individual targets (see Table 4.1). As can be observed from the distributions, the mean of the reconstructed (absolute) distribution for target one is −57.94 cm (−60.12 cm); target two is −20.16 cm (−20.12 cm); target three is 19.72 cm (19.88 cm); target four is 38.19 cm (39.88 cm); target five is 53.37 cm (59.88 cm) and target six is 79.13 cm (79.88 cm). The rms value of the distributions vary from 34 to 53 cm. Figure 6.4 shows the superimposed distribution of the z-vertecies for each target.

All the multiple-track events are rejected. The measured momentum in the forward spectrometer is compared against the momentum information provided by the tagging station for each event within the momentum bite (9%).

Selection of pp Elastic Events

The correlation between the four-momentum-transfer squared $|t|$ (or forward scattering angle θ_s) and the ADC counts of pulse amplitudes is used in identifying the elastic events. The elastic events present themselves as a distinct diagonal band on the $|t|$ vs ADC scatter plot. Scattering from the carbon nuclei and the straight-through events are observed as a horizontal band. Figure 6.5 shows this correlation between $|t|$ and the slow component of the ADC for target 3 where no cuts are applied except the minimum t cut.

As mentioned in Chapter V, there are other processes that take place when a proton strikes a target. Scattering from the carbon nuclei constitutes the primary source

of background. Straight-through particles also obscure the elastic pp events, especially in the low $|t|$-region. In addition, a broad distribution of quasi-elastic events contributes to the background. In order to extract the pure pp elastic events from the background, three different criteria are applied to the data set.

1. A priori, two parallel diagonal cuts, above and below the elastic-event band, are applied to eliminate most of the uncorrelated and quasi-elastic events .
2. The z-vertex cut, $|Z_{reconstructed} - Z_{measured}| \tan\theta_s < \mathrm{M}\sigma$, where $\mathrm{M}\sigma$ is 2.25 to 2.70 and σ is the standard deviation of the $(Z_{reconstructed} - Z_{measured})$ distribution, constrains the events that come from a given target .
3. Much like the case above, another constraint is constructed for the four-momentum transfer squared. If $|t_{measured} - t_{expected}| > \mathrm{N}\sigma$, where $\mathrm{N}\sigma = 0.006 - 0.007$, then the event is rejected.

Figure 6.6 is one of the distributions that is used in the application of cuts to the data set. $(Z_{reconstructed} - Z_{measured}) \tan\theta_s$ is shown for individual targets. As can be seen from the distributions, the outer tails of the distributions are due to the events that come away from the target location. The cut applied to this distribution is about one standard deviation wide.

The ADC spectra for target 6 are shown in Figure 6.7 for the slow component. In general, for each target, the background events are always seen in the lower ADC values. These events are mostly due to carbon scattering, minimally-ionizing and uncorrelated particles that are accepted by the trigger. These events at the lower end of the spectrum constitute the major source of background. As the $|t|$ value is increased, the events that come from the elastic pp scattering form a gaussian distribution and shift away from the background.

If one makes a binning of the $|t|$ vs ADC correlation, Figure 6.5, in equal $|t|$ intervals, the projection of the events onto the ADC axis exhibits the distributions that are obeyed by each specific type of event. The through-going particles show a Landau type distribution, whereas the pp recoil events obey gaussian statistics (Figure 6.8). As $|t|$ values increase, the gaussian distribution separates from the background events, enabling us to make a correlation beween the $|t|$ values and the expected ADC counts per hit. The central peaks of the gaussian distribution, in the relatively background-free momentum-transfer region, can be linearly fitted (Figure 6.9) to form a correlation between the expected $|t|$ and ADC values. Based upon this criterion, it is possible to further restrict the $|t|$ vs ADC correlation. From this linear fit, expected $|t|$ values are calculated for each measured ADC count. Figure 6.9 shows this fit for ten equally spaced t-bins (t bin is 0.005 $(\mathrm{GeV/c})^2$ wide). The first three bins are omitted from the fit so as not to bias the fit by the events that are at the very low t region which is most contaminated by background. Consequently, one has an expected t value for a measured ADC count, i.e. a comparison of the expected and the measured t values is possible. The distribution of $(t_{measured} - t_{expected})$ is shown in Figure 6.10. As mentioned earlier, this criterion is used to constrain the t distribution further.

After the above criteria are applied and the systematic checks are performed and a clean sample of events is selected. The left and right scattered particles are checked for the z-vertex reconstruction independently to ensure that there is no residual bias in the definition of the azimuthal angle ϕ. Similar checks are performed for the ADC values as a function of the azimuthal angle ϕ, the scattering angle θ, the polarization state of the beam, and the snake magnet state. From this sample of events, the pp analysing power in the Coulomb-nuclear interference region, A_N, is calculated as described below.

Calculation of Asymmetries

There are several ways of calculating asymmetries. The method described below has the advantage that, in taking the geometric mean of products, the normalization factors are automatically cancelled.

We have the following parameters that need to be considered in this calculation:

1. Polarization: There are seven bins of polarization states $P_i = (1, ...7)$. The beam contains both positive and negative polarization states simultaneously from −65% to +65%. Omitting the central bin, $P_i = 4$ (average zero polarization state), we define negative ($P_i = 1, 2, 3$) and positive ($P_i = 5, 6, 7$) polarization states of the beam (see Figure 3.13).
2. Snake magnet state: Snake magnets reverse the spin direction from up to down, or vice versa, every 10 spills. This reversal of spin direction eliminates the systematic errors in the apparatus.
3. Left-Right/Up-Down scattering: The azimuthal angle ϕ is measured by the forward spectrometer. Up-Down scattered particles are rejected at the trigger level.

The number of events N, as a function of the above three variables, is defined here as $N = N(L/R, +/-, \uparrow / \downarrow)$ =(Left/Right, Polarization, Snake state). For a single $|t|$ bin, we form two groups of numbers, each containing 4 numbers.

Group A. $N(L,+,\uparrow), N(L,-,\downarrow), N(R,+,\downarrow), N(R,-,\uparrow)$.

Group B. $N(R,+,\uparrow), N(R,-,\downarrow), N(L,+,\downarrow), N(L,-,\uparrow)$.

The asymmetry ϵ can be calculated from these numbers. If we take the products of the numbers in Group A and in Group B separately and call them A and B, respectively, i.e.,

$$A = N(L,+,\uparrow)N(L,-,\downarrow)N(R,+,\downarrow)N(R,-,\uparrow), \tag{6.1}$$

$$B = N(R,+,\uparrow)N(R,-,\downarrow)N(L,+,\downarrow)N(L,-,\uparrow). \tag{6.2}$$

The asymmetry, ϵ, is

$$\epsilon = \frac{A^{1/4} - B^{1/4}}{A^{1/4} + B^{1/4}} \tag{6.3}$$

It is possible to calculate many asymmetries from the numbers that constitute A and B, but not all of these asymmetries would have a significant or physical meaning. Therefore, six other asymmetries are calculated as a measure of control of the apparatus and a double-check of the results. First, calculate the *space* asymmetry for left and right scattered particles separately.

$$\epsilon_L = \frac{\sqrt{N(L,+,\uparrow)N(L,-,\downarrow)} - \sqrt{N(L,+,\downarrow)N(L,-,\uparrow)}}{\sqrt{N(L,+,\uparrow)N(L,-,\downarrow)} + \sqrt{N(L,+,\downarrow)N(L,-,\uparrow)}}, \tag{6.4}$$

$$\epsilon_R = \frac{\sqrt{N(R,+,\downarrow)N(R,-,\uparrow)} - \sqrt{N(R,+,\uparrow)N(R,-,\downarrow)}}{\sqrt{N(R,+,\downarrow)N(R,-,\uparrow)} + \sqrt{N(R,+,\uparrow)N(R,-,\downarrow)}}. \tag{6.5}$$

The difference between these two asymmetries should result in zero, given that there are no false asymmetries associated with left and right scattered particles.

The second asymmetry that one can calculate is the *snake* asymmetry for each snake state. The snake variable is kept fixed, and the polarization and space variables are varied.

$$\epsilon_\uparrow = \frac{\sqrt{N(L,+,\uparrow)N(R,-,\uparrow)} - \sqrt{N(L,-,\uparrow)N(R,+,\uparrow)}}{\sqrt{N(L,+,\uparrow)N(R,-,\uparrow)} + \sqrt{N(L,-,\uparrow)N(R,+,\uparrow)}}, \tag{6.6}$$

$$\epsilon_{\downarrow} = \frac{\sqrt{N(L,-,\downarrow)N(R,+,\downarrow)} - \sqrt{N(L,+,\downarrow)N(R,-,\downarrow)}}{\sqrt{N(L,-,\downarrow)N(R,+,\downarrow)} + \sqrt{N(L,+,\downarrow)N(R,-,\downarrow)}}. \tag{6.7}$$

Analogously, the difference between the two snake asymmetries should be zero if the snake rotation magnets do not introduce false asymmetries.

The third asymmetry that is calculated is the *tagging* asymmetry, i.e. the asymmetry that might come from the different signs of polarization in the beam. As in the other cases, the difference between ϵ_+ and ϵ_- should ideally be zero.

$$\epsilon_+ = \frac{\sqrt{N(L,+,\uparrow)N(R,+,\downarrow)} - \sqrt{N(L,+,\downarrow)N(R,+,\uparrow)}}{\sqrt{N(L,+,\uparrow)N(R,+,\downarrow)} + \sqrt{N(L,+,\downarrow)N(R,+,\uparrow)}}, \tag{6.8}$$

$$\epsilon_- = \frac{\sqrt{N(L,-,\downarrow)N(R,-,\uparrow)} - \sqrt{N(L,-,\uparrow)N(R,-,\downarrow)}}{\sqrt{N(L,-,\downarrow)N(R,-,\uparrow)} + \sqrt{N(L,-,\uparrow)N(R,-,\downarrow)}}. \tag{6.9}$$

In addition to the geometric mean method of calculating raw asymmetries as described above, one can construct other expressions to estimate asymmetries. Consider for a given t bin the number events that form Group A,

$$N(L,+,\uparrow) = N(+,\uparrow) \int_{-\Phi}^{\Phi} d\phi \int_{\theta-\delta\theta/2}^{\theta+\delta\theta/2} \frac{d\sigma}{d\Omega} \sin\theta d\theta \, (1 + A(\theta)P_+ \cos\phi) \tag{6.10}$$

$$N(R,-,\uparrow) = N(-,\uparrow) \int_{-\Phi}^{\Phi} d\phi \int_{\theta-\delta\theta/2}^{\theta+\delta\theta/2} \frac{d\sigma}{d\Omega} \sin\theta d\theta \, (1 + A(\theta)P_- \cos\phi) \tag{6.11}$$

$$N(L,-,\downarrow) = N(-,\downarrow) \int_{-\Phi}^{\Phi} d\phi \int_{\theta-\delta\theta/2}^{\theta+\delta\theta/2} \frac{d\sigma}{d\Omega} \sin\theta d\theta \, (1 + A(\theta)P_- \cos\phi) \tag{6.12}$$

$$N(R,+,\downarrow) = N(+,\downarrow) \int_{-\Phi}^{\Phi} d\phi \int_{\theta-\delta\theta/2}^{\theta+\delta\theta/2} \frac{d\sigma}{d\Omega} \sin\theta d\theta \, (1 + A(\theta) P_+ \cos\phi) \tag{6.13}$$

The azimuthal angle ϕ is integrated between the maximum and the minimum of the ϕ acceptance around the horizontal plane (see Figure 6.11). Similar expressions are written for Group B, but note that the sign in front of the the analysing power $A(\theta)$ is negative according to our convention. The following subgroups are formed from Group A and Group B.

Group A.1 $N(L,+,\uparrow) + N(R,-,\uparrow)$ Group A.2 $N(R,+,\downarrow) + N(L,-,\downarrow)$.

Group B.1 $N(R,+,\uparrow) + N(L,-,\uparrow)$ Group B.2 $N(R,-,\downarrow) + N(L,+,\downarrow)$.

The underlying intention in this particular method is to sum over the same snake states within each group and thereby remove the false asymmetries due to the snake magnets from the real asymmetry. For the calculation of the asymmetry we then make the following combination,

$$\epsilon = \frac{(A.1)\,(A.2) - (B.1)\,(B.2)}{\left[\sqrt{(A.1)\,(A.2)} + \sqrt{(B.1)\,(B.2)}\right]^2} \tag{6.14}$$

The equations (6.10)–(6.13) are easily integrated and substituting them to equation (6.14) gives the physical asymmetry

$$\epsilon = \frac{N(+)P_+ + N(-)P_-}{N(+) + N(-)} \left(\frac{\sin\Phi}{\Phi}\right) \frac{\int A(\theta) \frac{d\sigma}{d\Omega} \sin\theta d\theta}{\int \frac{d\sigma}{d\Omega} \sin\theta d\theta} \tag{6.15}$$

where the first multiplicative term on the right is the average beam polarization, the second term is due to the azimuthal acceptance, and the last term is the pp analysing power. If

we assume that the analysing power is constant then we have a simple relationship as shown below.

$$A = \frac{\Phi}{\sin\Phi}\frac{\epsilon}{P_b}. \tag{6.16}$$

Results and Discussions

The pp analysing power, A, is measured for the first time in the Coulomb-nuclear interference region using the 200 GeV/c polarized proton facility at the Fermi National Accelerator Laboratory (FNAL) . The effective four-momentum transfer squared ranged from 3.0×10^{-3} to $5.0 \times 10^{-2}\,(\mathrm{GeV/c})^2$. Figure 6.12 shows the results of this measurement. The errors shown in the figure and below are statistical only. The results can be summarized as follows,

1. $3.0 \times 10^{-3} \leq -t \leq 1.0 \times 10^{-2}\,(\mathrm{GeV/c})^2, \quad A = 2.47 \pm 0.40, \quad N = 58143$
2. $1.0 \times 10^{-2} \leq -t \leq 2.0 \times 10^{-2}\,(\mathrm{GeV/c})^2, \quad A = 3.80 \pm 0.52, \quad N = 38400$
3. $2.0 \times 10^{-2} \leq -t \leq 3.0 \times 10^{-2}\,(\mathrm{GeV/c})^2, \quad A = 3.22 \pm 0.60, \quad N = 25006$
4. $3.0 \times 10^{-2} \leq -t \leq 4.0 \times 10^{-2}\,(\mathrm{GeV/c})^2, \quad A = 1.85 \pm 0.82, \quad N = 13954$
5. $4.0 \times 10^{-2} \leq -t \leq 5.0 \times 10^{-2}\,(\mathrm{GeV/c})^2, \quad A = 1.93 \pm 1.54, \quad N = 4360$

The experimental results agree well with the theoretical predictions above $1.0 \times 10^{-2}\,(\mathrm{GeV/c})^2$. At the lowest t bin however, there is a possible disagreement. The analysing power of pC elastic scattering at this beam energy and momentum transfer is not well-known. If the pC analysing power is less than that of pp then it is conceivable that the pC scattering reduces the measured effect in this very low t range. The theoretical prediction for pC analysing power for these energies is comparable for that of pp,

but there are no experimental data. This t region, where the background from pC scattering is still present, can be best shown as a function of ADC slow component bins and $(t_{measured} - t_{expected})$. Figure 6.13, for target one, presents the effect of the background in the very low t region. The ADC counts are progressively binned in 25 counts each, and the first six plots show the $(t_{measured} - t_{expected})$ distribution for each bin. The last plot is for all the rest of the events in the remaining large ADC bin (150–1024). It can be observed that the signal to noise ratio after the third plot is better then 4:1. In the first three plots, however, the carbon events dominate the distributions.

The multiple scattering of the events from the material in the beam contributes to the overall broadening of the t distribution per t bin. The overall contribution from the Coulomb multiple scattering of protons with the material in the beam (see equation (5.16)) to the scattered tracks is about 0.21 milliradians. The average scattering angle for the first t bin is about 0.33 milliradians. Thus, this particular t bin is very sensitive to the multiple scattering of the events. This effect would tend to lower the observed asymmetry in the lowest t bin since the scattered particles are to some degree ambiguously defined in θ_n and ϕ.

The momentum spread of the beam is further dispersed by the analysing magnet. This smears the distribution of events detected at GC, thereby directly effecting the t and ϕ resolution. The momentum correction for each event at the level of MLUs was employed in the trigger but the smearing of the analysing magnet is nevertheless an intrinsic nature of the spectrometer. On the other hand, however, the analysing magnet reduces the background due to low-energy charged particles.

The diffuseness of the MLU cuts (Figure 6.11) has a large impact on the very low t region in terms of background. The events that scatter at very small scattering angles are sensitive to the sharpness of the cuts since they impact the GC at a very small

region. If the effective cut is fuzzy, then the ambiguity in selection of events occurs as a function of $theta_s$ and ϕ. The boarder effects of the GC also contribute to this in a lesser degree since the inconsistent events are omitted by the coding of the hodoscope at the trigger level. Figure 6.14 is the four-momentum transfer squared distribution before and after the cuts. The pC elastic scattering events, the contributions from the multiple Coulomb scattering events and the Landau fluctuations of the minimally-ionizing particles are clearly observed in the lower t region below $1.5 \times 10^{-2}\,(\mathrm{GeV/c})^2$. The t range from 1.5×10^{-2} to $4.5 \times 10^{-2}\,(\mathrm{GeV/c})^2$ contains the pp elastic scattering events. The sharper fall of the distribution at the very high end of the spectrum, above $4.5 \times 10^{-2}\,(\mathrm{GeV/c})^2$, indicate that the trigger effects appear.

As it is pointed out in Chapter II, the spin-flip pomeron amplitude may be nonzero and this is possible if the nucleon contains a dynamically enhanced component with a compact diquark. If there is such a process, this effect is expected to be no more than 5 – 10 % based on the lower energy data at 6 and 10 GeV/c. It is not clear how this percentage may differ from the above estimation at higher energies, say 200 GeV/c. The initial results presented here do not discount the possibility of nonzero spin-flip hadronic amplitudes at the level of 10 %. This point will need to be further studied and clarified as yet there are not enough statistics for a conclusive answer.

The polarization studies of elastic pp scattering were performed at a moderately low four-momentum transfer squared region at 100, 200 and 300 GeV/c beam momenta [Fide81, Snyd78]. They ~~both~~ used polarized targets, as opposed to a polarized beam as in our case. Fidecaro et al. studied the polarization effects in the range of $0.5 \leq -t \leq 4.0\,(\mathrm{GeV/c})^2$ at 200 GeV/c and found that the polarization changed sign around $0.67\,(\mathrm{GeV/c})^2$. Snyder et al. studied the same phenomena at 100 and 300 GeV/c in the range of $018 \leq -t \leq 2.0\,(\mathrm{GeV/c})^2$. To this day there has been no measurement of

polarization effects in the range of $0.05 \leq -t \leq 0.15\,(\mathrm{GeV/c})^2$. The pp differential elastic cross-section in this region is about $20 - 50$ mb/(GeV/c)^2. It is importance to cover this range in order to observe the hadronic polarization effects (see Chapter II). Figure 6.15 presents these data along with the current measurements. The first point, indicated as a square [Akch89], was measured during the 1988-89 fixed target period at FNAL. During that testing period the feasibility of a polarimeter based on the Coulomb-nuclear interference was established. The first scheme for the trigger was also tested. The total number of usable events was 36×10^3 out of 3.0×10^6 during a short period of data-taking.

Figures 6.16, 6.17 and 6.18 present the raw asymmetry control parameters as described in the previous section for each target. For figure 6.16 see equations (6.4) and (6.5); for figure 6.17 see equations (6.6) and (6.7); and for figure 6.18 see equations (6.8) and (6.9).

Run Summary

During the 1990 fixed-target run, the CNI polarimeter was alotted testing and data-taking periods at three different times. During the entire CNI running period we accumulated 135 runs over 85 tapes.

Period 1. 10 March–13 March, Test runs 1–16, (11 MT's),

Period 2. 13 May–15 May, Test runs 17–42, (18 MT's)

Period 3. 24 May–3 June, Data runs 43–135 (56 MT's).

Period 1 :

1. Global timing of trigger and check of logic is accomplished.
2. Chamber debugging and tuning take time.
3. Tuning of DAQ - many PDP crashes occur.

4. Target veto counters are tuned and their effectiveness is studied.
5. Timing of scalers for utility signals for CNI/$\Delta\sigma_T$ is done.
6. Tuning of Pulse Shape Discrimination (PSD) of target signals takes time.
7. No automatic Snake Magnet reversal takes place in this Period.
8. The straight track run is taken.
9. The live time fraction is 0.2 %.

Period 2 :

1. All downstream logic and timing are rechecked with the antiproton beam.
2. The final Good Target (GT) signal and $\sum$ Latch signals are in trigger.
3. The Multistrip Detector (MSD) is installed.
4. The SBF signal is introduced to trigger.
5. After $\Delta\sigma_T$ test runs, CNI comes back and runs straight tracks.
6. Problems with BM109 polarity are found (wrong sign).
7. Many PDP crashes occur due to bad memory location in the memory board.
8. Snake magnets are now automatic, but many software crashes take place and it is realized that the snake state was partial L-type !
9. Correlation between downstream trigger and target logic is poor.
10. BK chambers are in data-stream.

Period 3 :

1. Modifications to electronics are done to make it more compatible with $\Delta\sigma_T$.
2. Target analog signals are timed to ADC's.
3. The NW hodoscope is introduced to the overall trigger.
4. Initial stages of target electronics are retuned.

5. The E704 Vax Cluster crashes for 26 hrs.
6. Target thresholds are once more tuned.
7. The live time fraction is measured to be 27%.
8. Problems with polarization signals from tagging electronics are investigated, several bad runs take place.
9. Individual target PSD signals are retuned up to the balanced signal level.
10. Live time is measured to be >50%.
11. Snake Magnets are changed to N2 mode.
12. Gray Code limiter electronics gives problems, several bad runs take place.
13. Calibration runs are taken (Pedestals, straight tracks, etc.).

Period 3 is when most of the useful data are taken. There are several runs with bad polarization coding and, later, with bad GC read-out. These runs are discarded. 68 % of the time (148 hours) a magnetic tape was mounted on the tape drive and for most of that time (approx. 75 %) there was beam (approx. 110 hours).

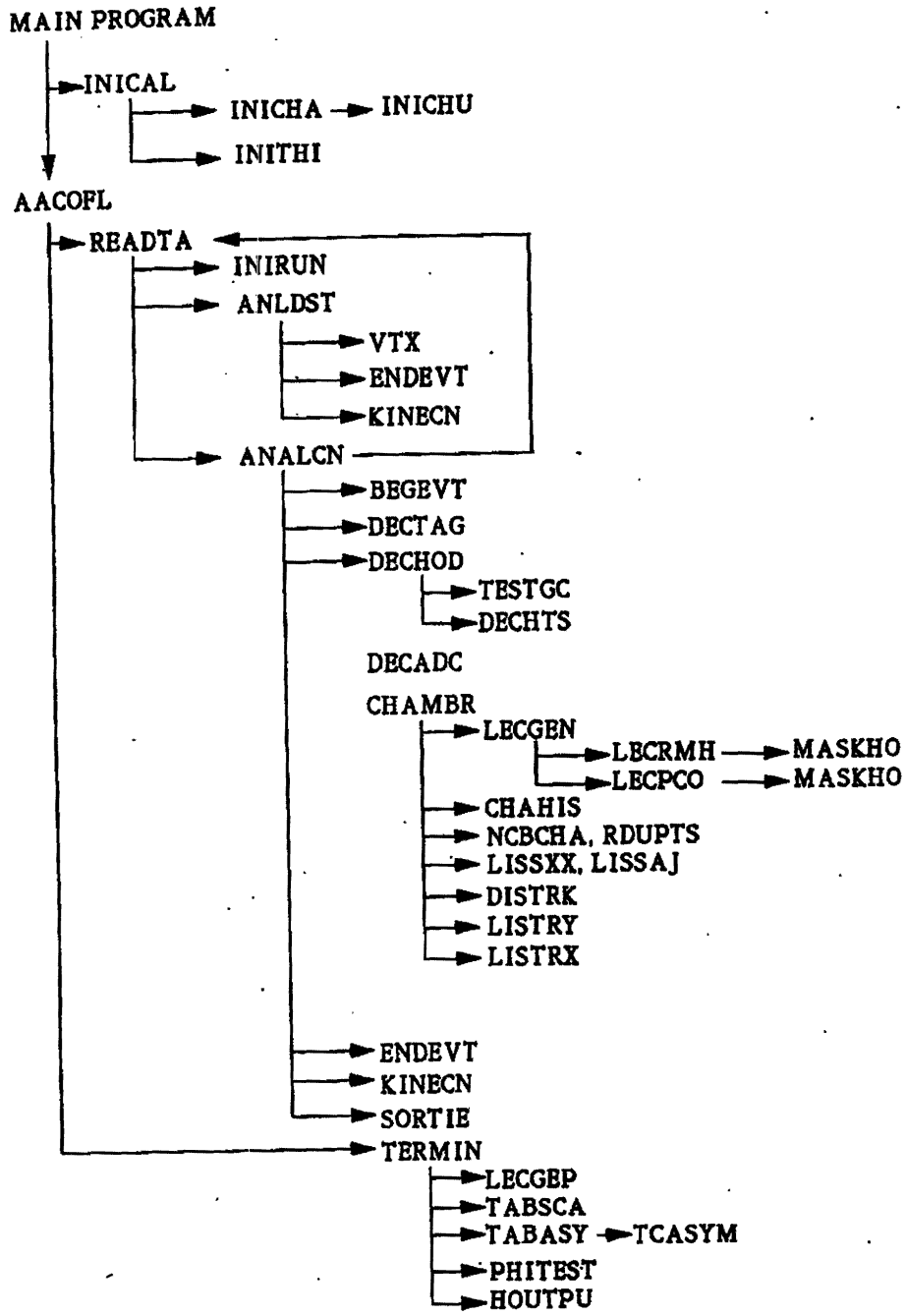

Figure 6.1 The general structure of the CNI off-line analysis code. The entire analysis code is written in FORTRAN and consists of over 7000 lines.

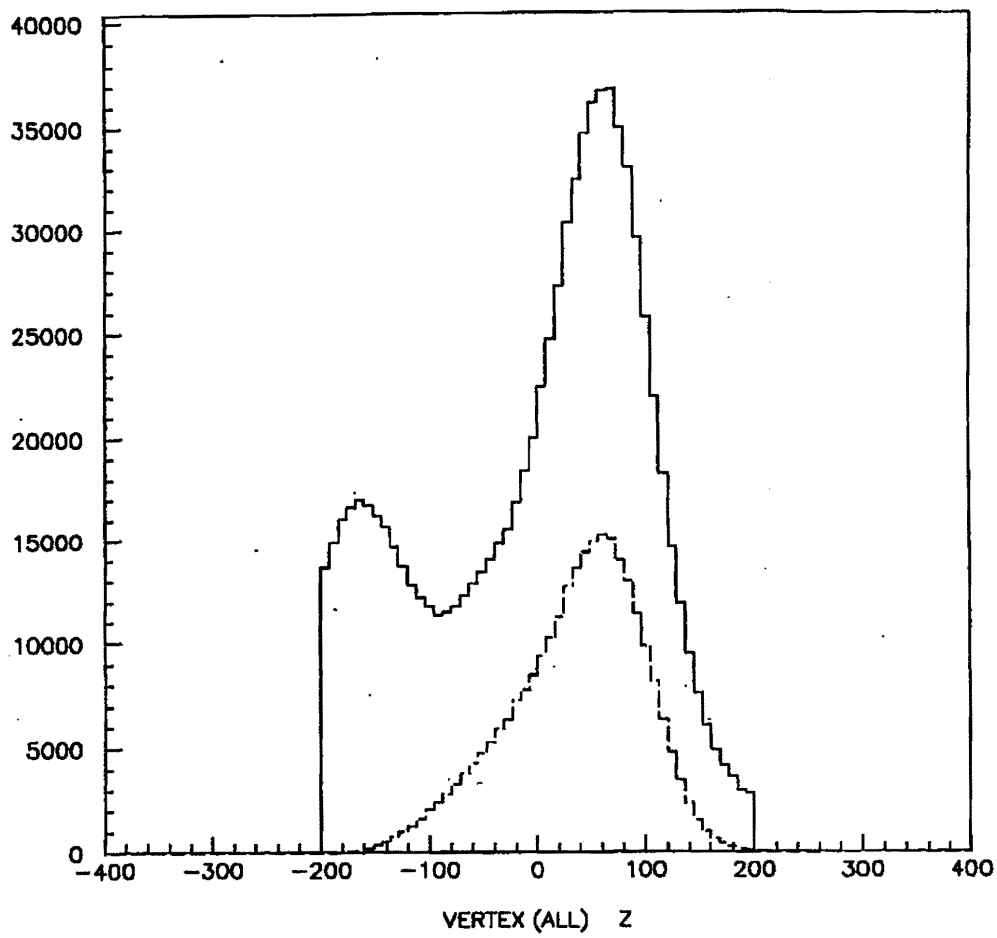

Figure 6.2 Z-vertex reconstruction of all events. The solid line is the z-vertex distribution of uncut events, and the dashed curve is the same distribution after the geometric and kinematic cuts. Z-vertex is in cm.

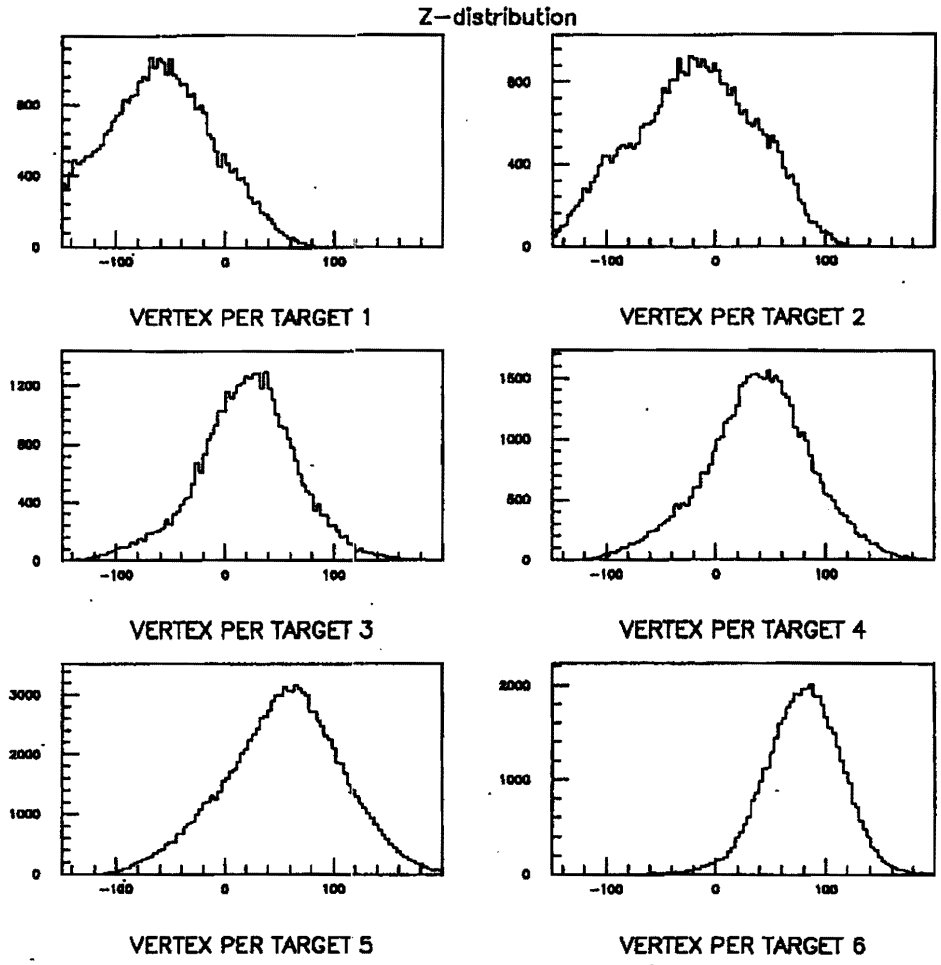

Figure 6.3 Z-vertex distribution of individual targets.

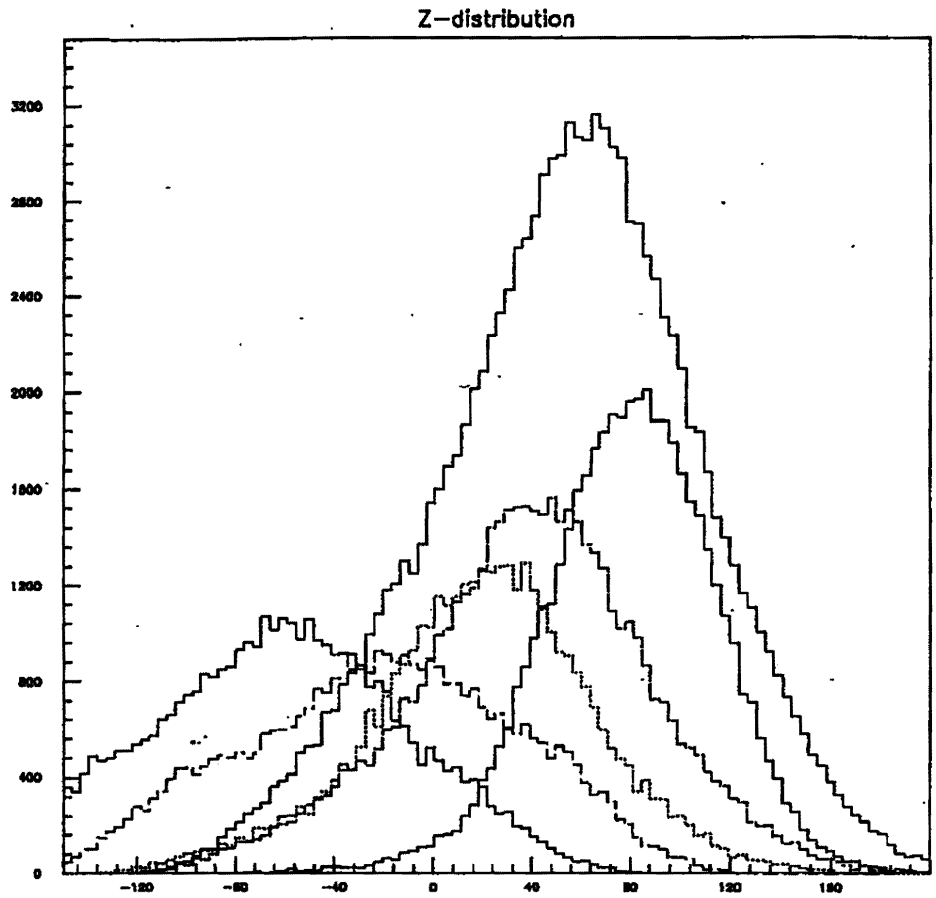

Figure 6.4 The superimposed z-vertex distribution of individual targets.

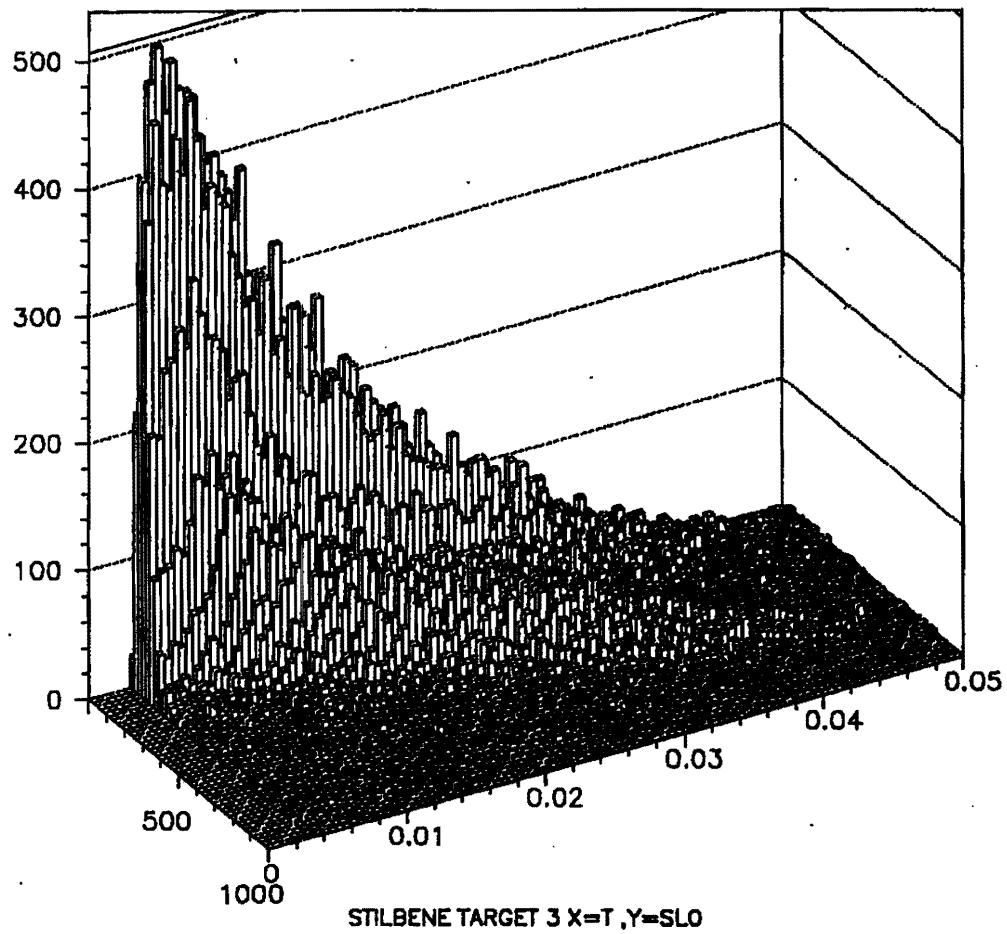

Figure 6.5 The correlation between the four-momentum transfer squared $|t|$ and the ADC slow component for target 3. The x-axis represents the ADC count; the y-axis is the four-momentum transfer squared in $(\mathrm{GeV}/c)^2$; and the z-axis represents the number of events. The diagonal band of events are due to elastic pp scattering. The background is observed as the high horizontal band.

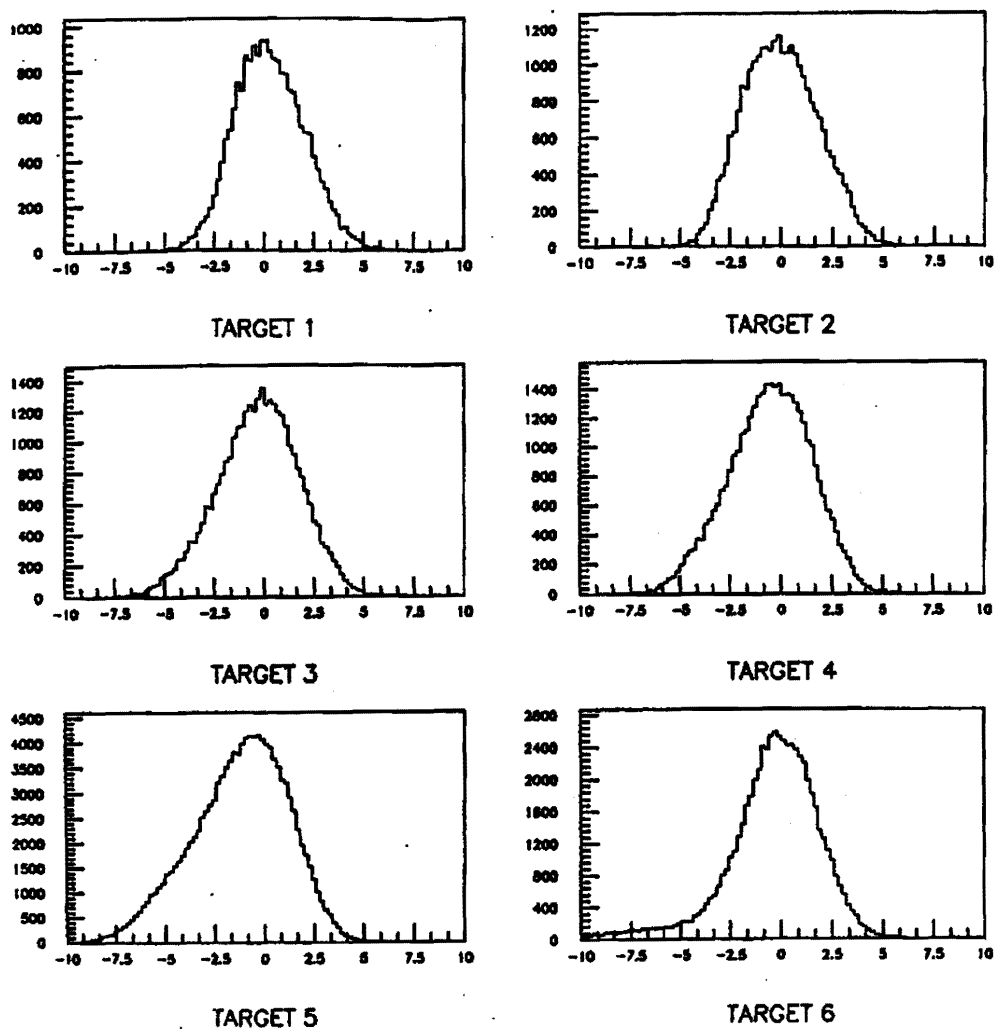

Figure 6.6 $(Z_{reconstructed} - Z_{measured}) \tan\theta_s$ distribution for each target.

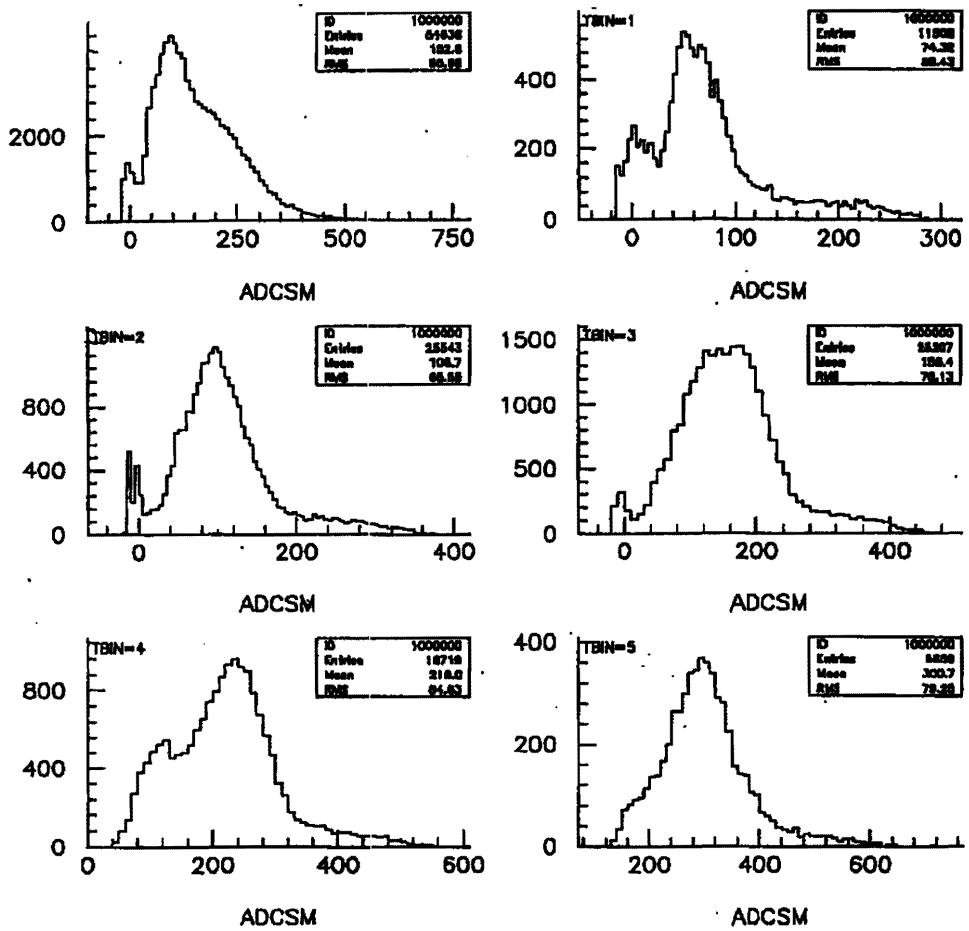

Figure 6.7 The ADC slow component spectrum for target 6 as a function of t binning. The first plot shows all of the events. The consequent plots are the ADC slow component spectra for each t bin $0.01\,(\mathrm{GeV/c})^2$ wide up to $0.05\,(\mathrm{GeV/c})^2$ in five t bins.

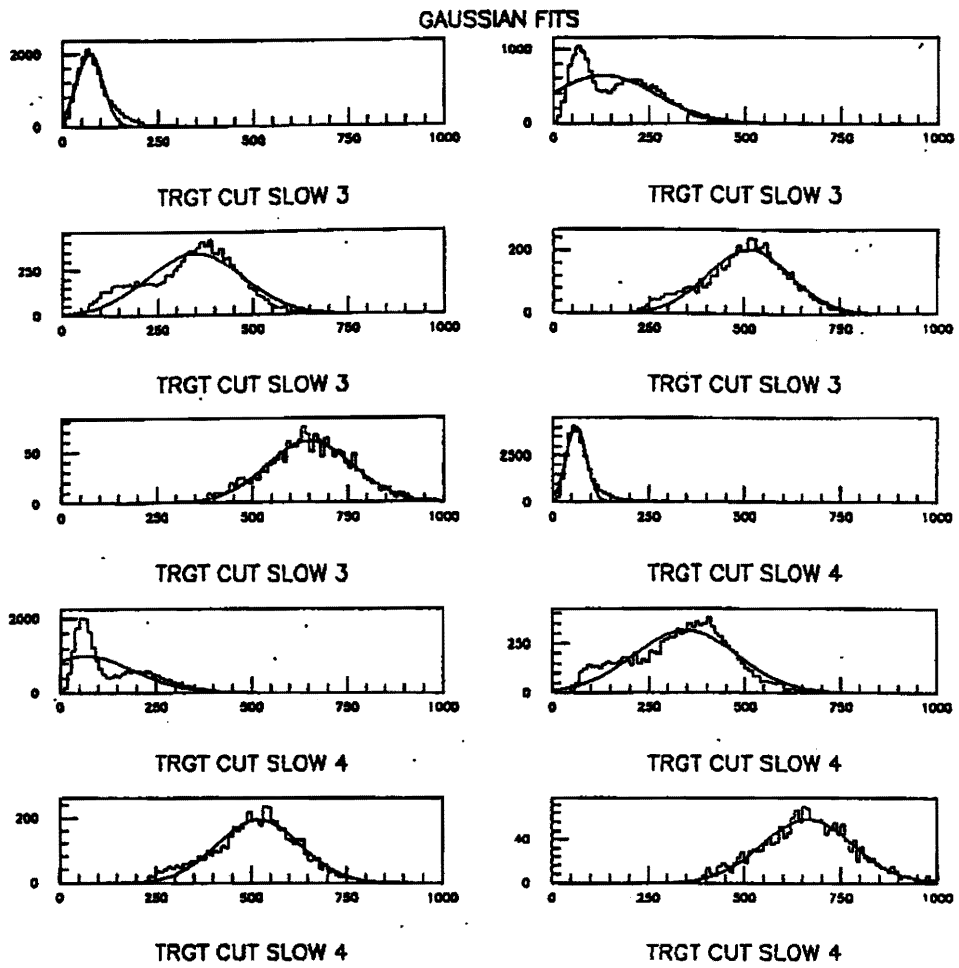

Figure 6.8 ADC slow component distribution of events for five different $|t|$-bins for target 3 and 4. The gaussian peak separates from the Landau distribution of minimally-ionizing particles as $|t|$ increases.

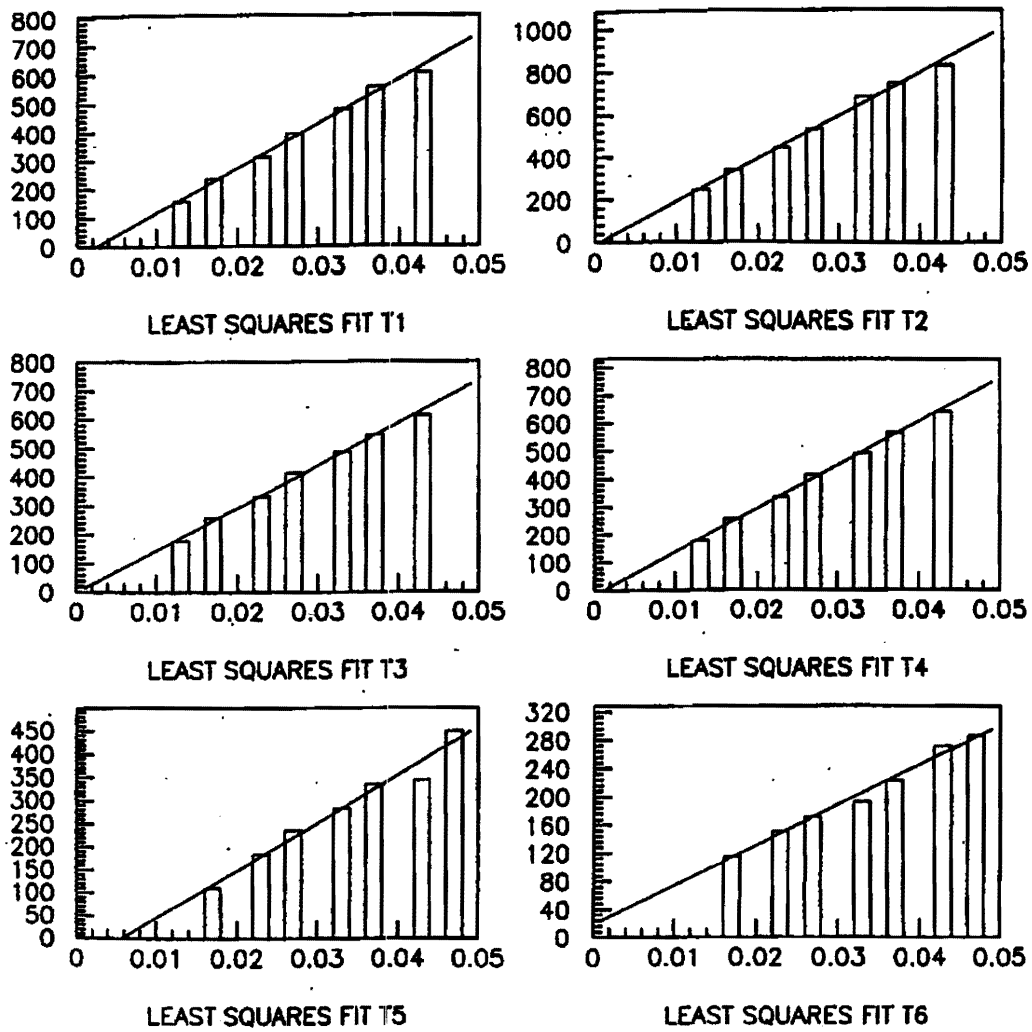

Figure 6.9 Linear fits of seven gaussian centroids for each target. These fits (in ten t bins, first three omitted) provide correlation between the expected $|t|$ and ADC counts for each event.

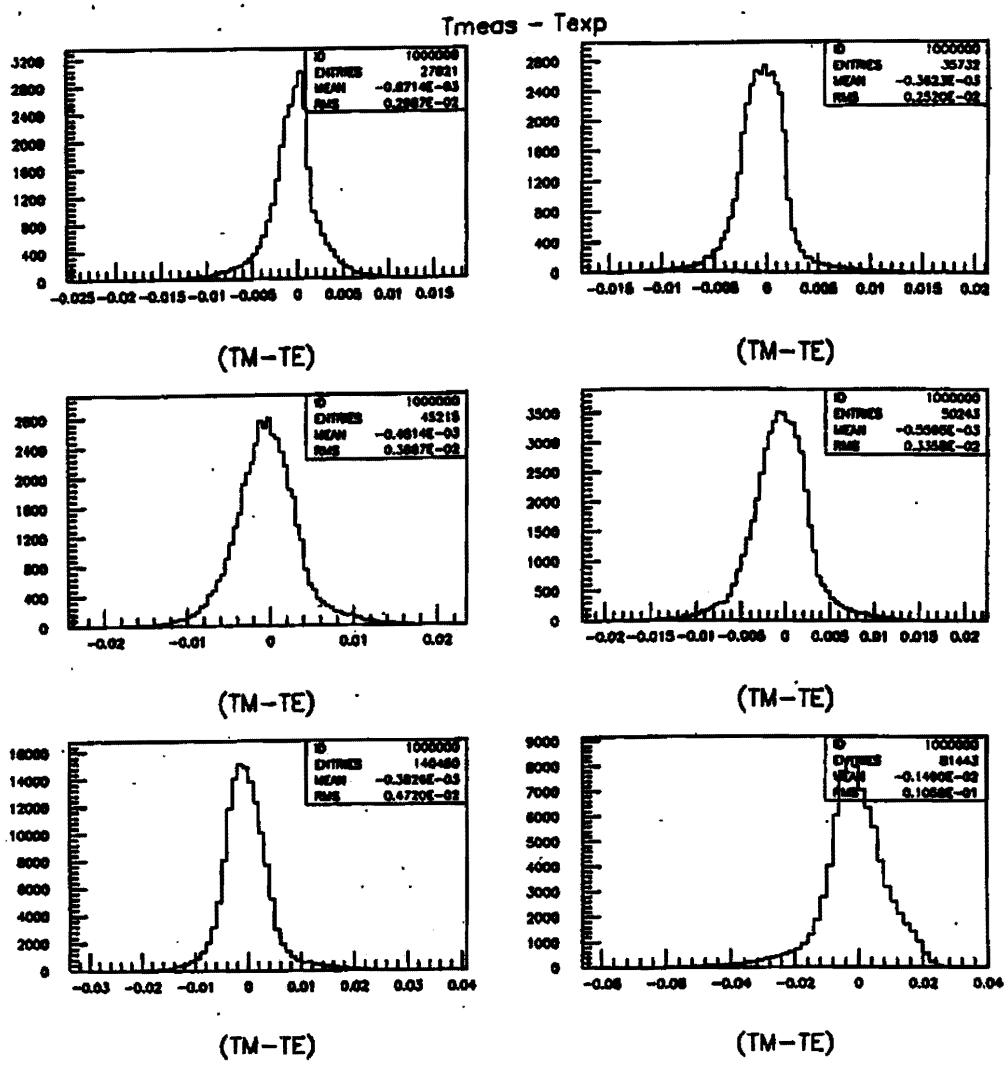

Figure 6.10 $(t_{measured} - t_{expected})$ distribution for each target. $t_{expected}$ is calculated from the linear fits shown in Figure 6.9.

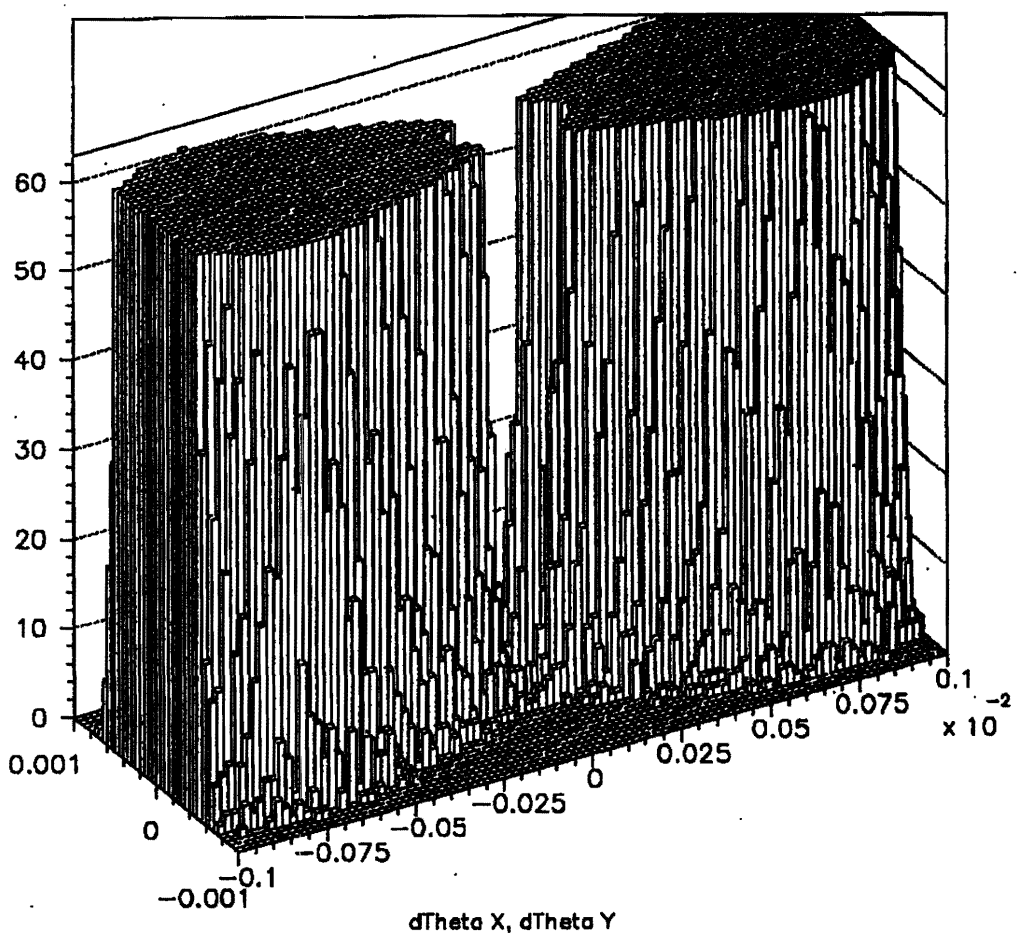

Figure 6.11 The *butterfly* cut as observed at GC. The events in the central part (beam), upper and lower quadrants are rejected at the trigger level.

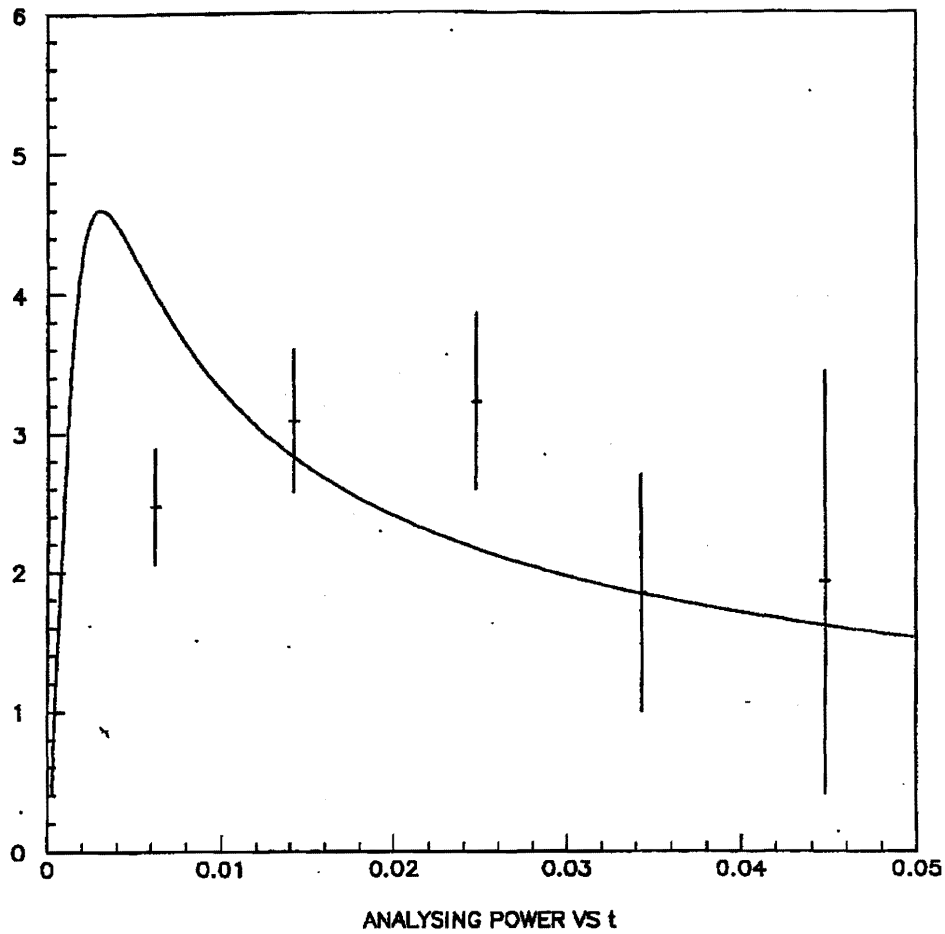

Figure 6.12 The analysing power, A_N, for pp elastic scattering in the Coulomb-nuclear interference region as a function of $|t|$. The solid curve is the theoretical prediction [Kope74]. The ordinate is in percentage polarization and the abscissa is in $(\mathrm{GeV}/c)^2$.

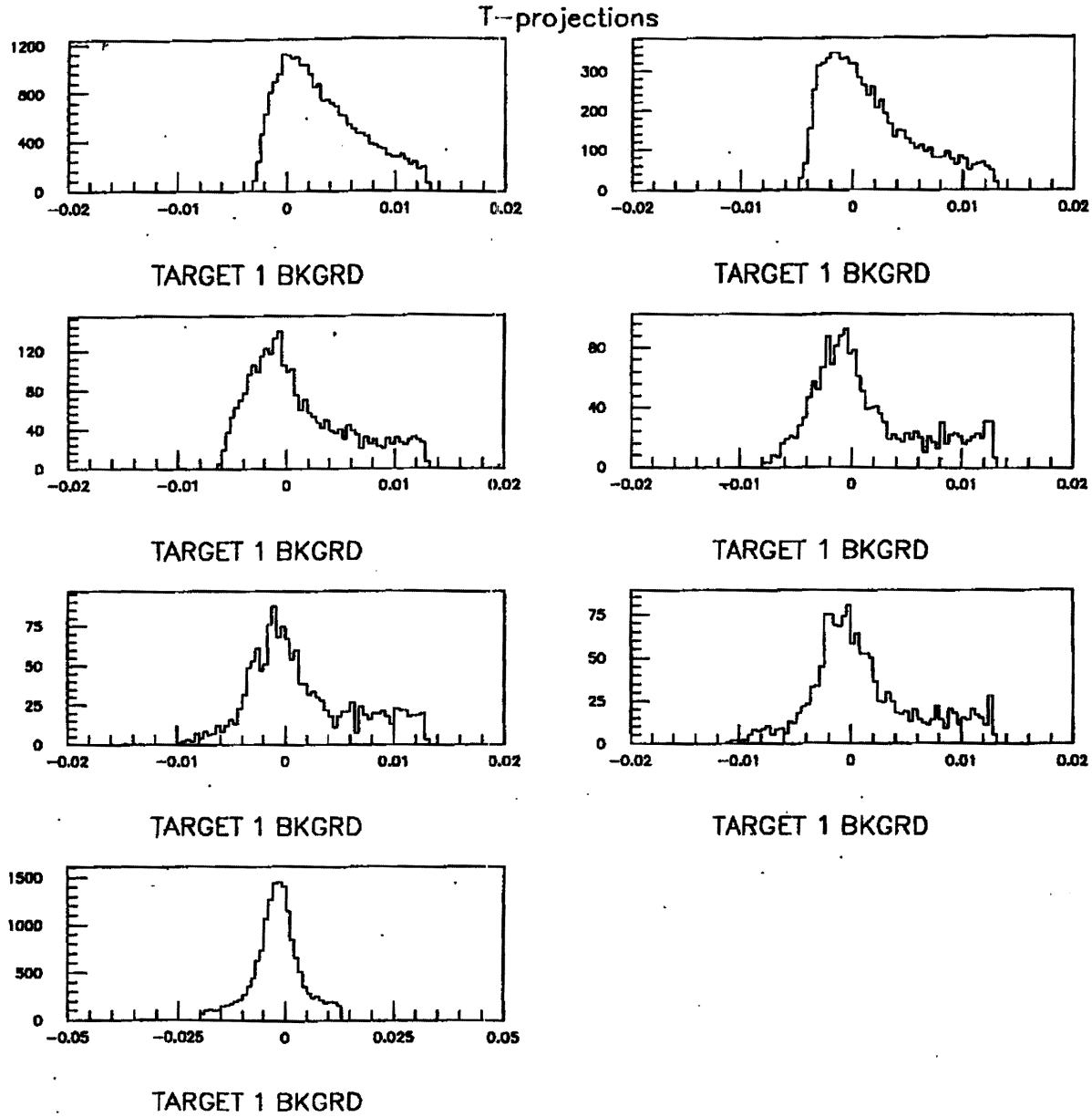

Figure 6.13 $(t_{measured} - t_{expected})$ distributions as a function of ADC bins for target one. Each ADC bin is 25 counts wide and the first six distribution are for ADC values from 0 to 150. The last plot covers the ADC range from 150 to 1024.

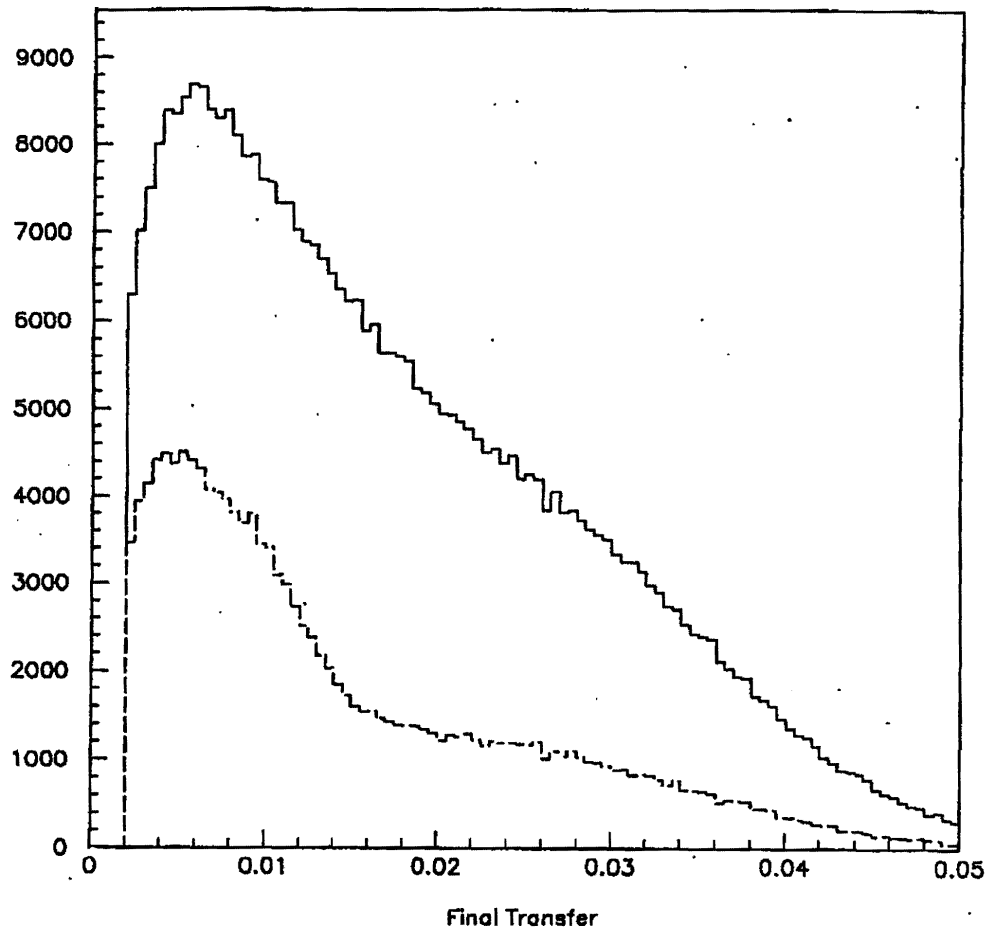

Figure 6.14 t distribution for all of the events before and after the cuts. The abscissa is in $(\mathrm{GeV}/c)^2$.

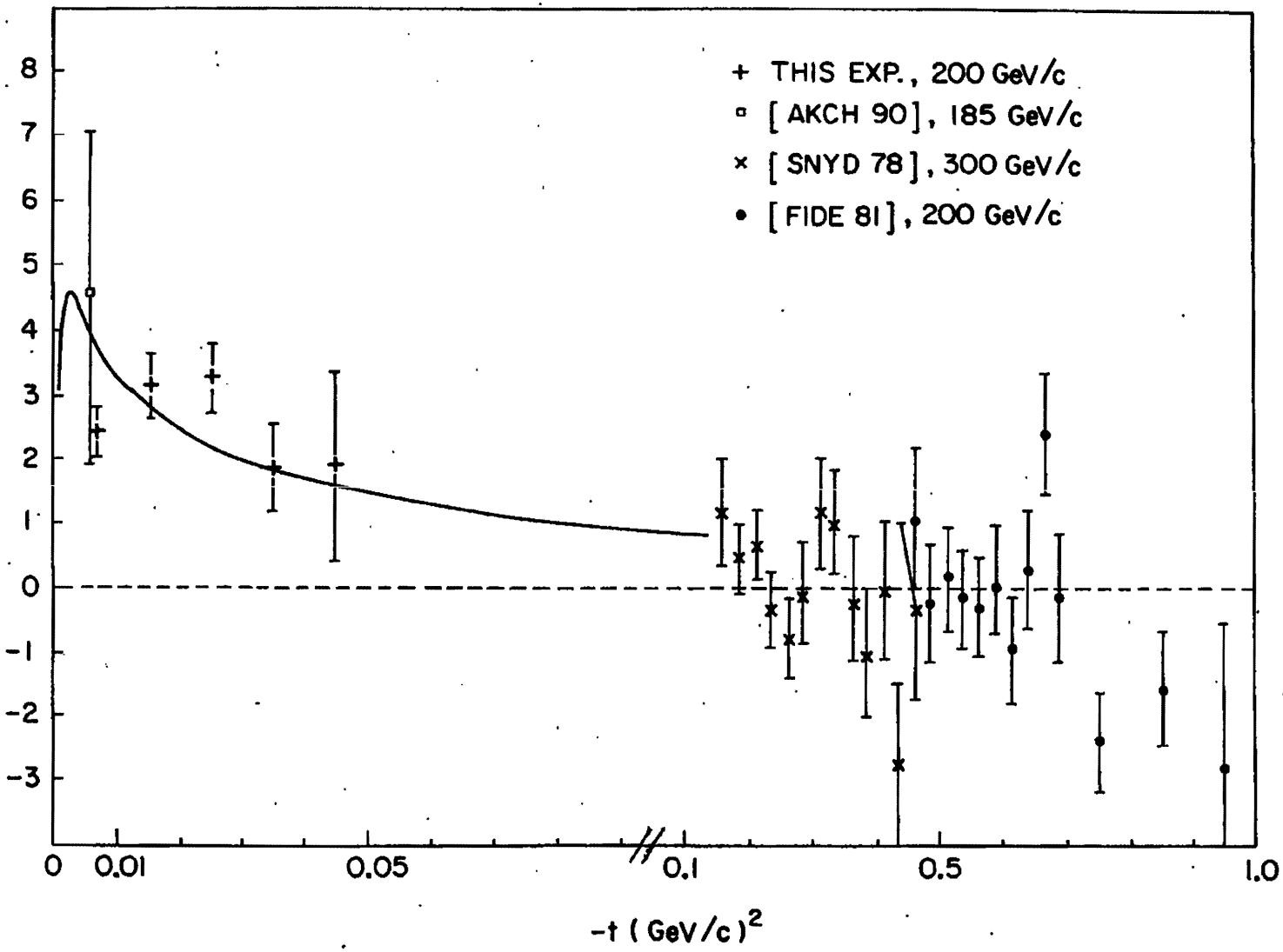

Figure 6.15 The compilation of polarization data for pp elastic scattering as a function of $|t|$ up to 1.0 $(\mathrm{GeV}/c)^2$. The solid curve is the theoretical prediction [Kope74] in the Coulomb-nuclear region. The ordinate is in percentage polarization and the abscissa is in $(\mathrm{GeV}/c)^2$.

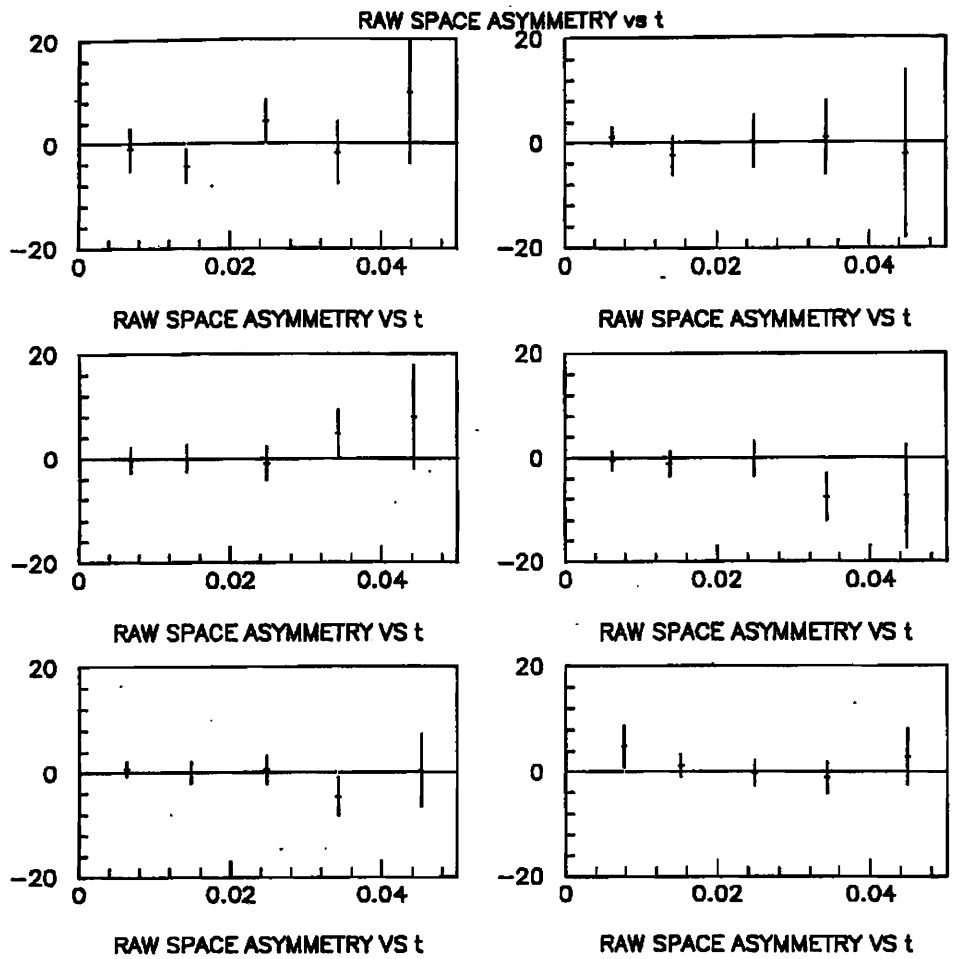

Figure 6.16 The raw *space* asymmetry for each target as a function of t.

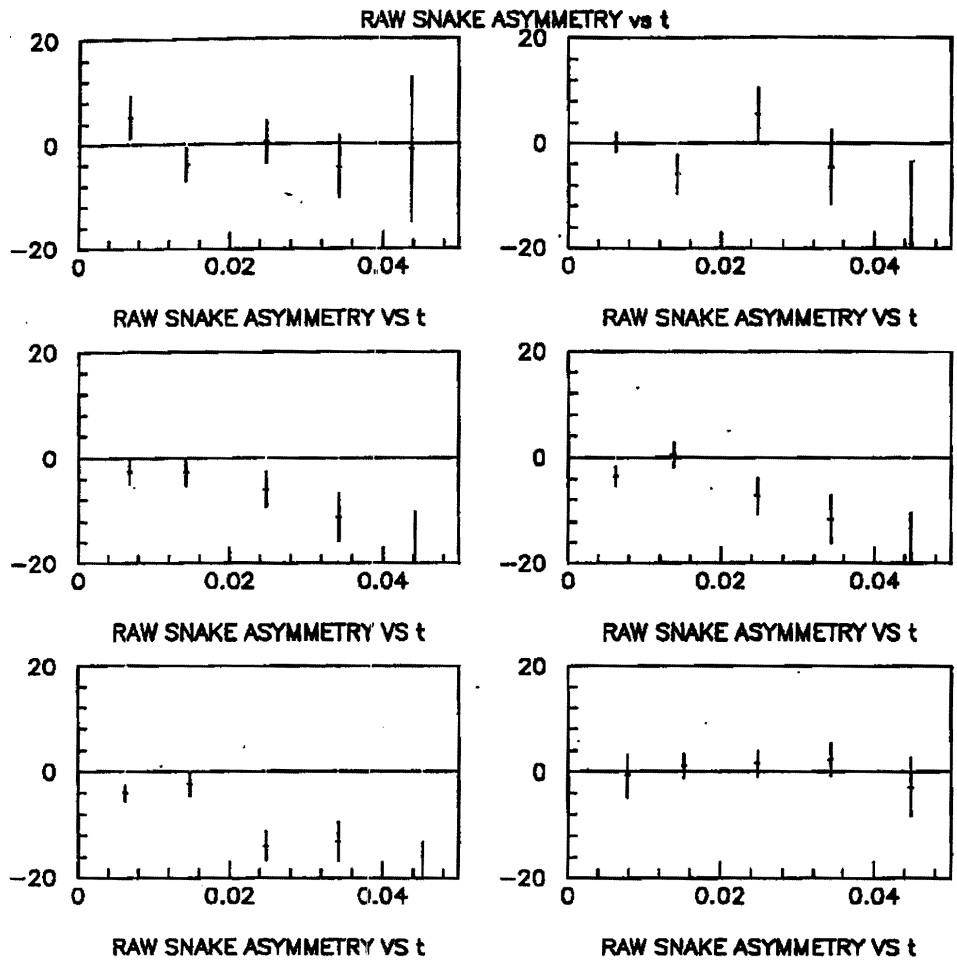

Figure 6.17 The raw *snake* asymmetry for each target as a function of t.

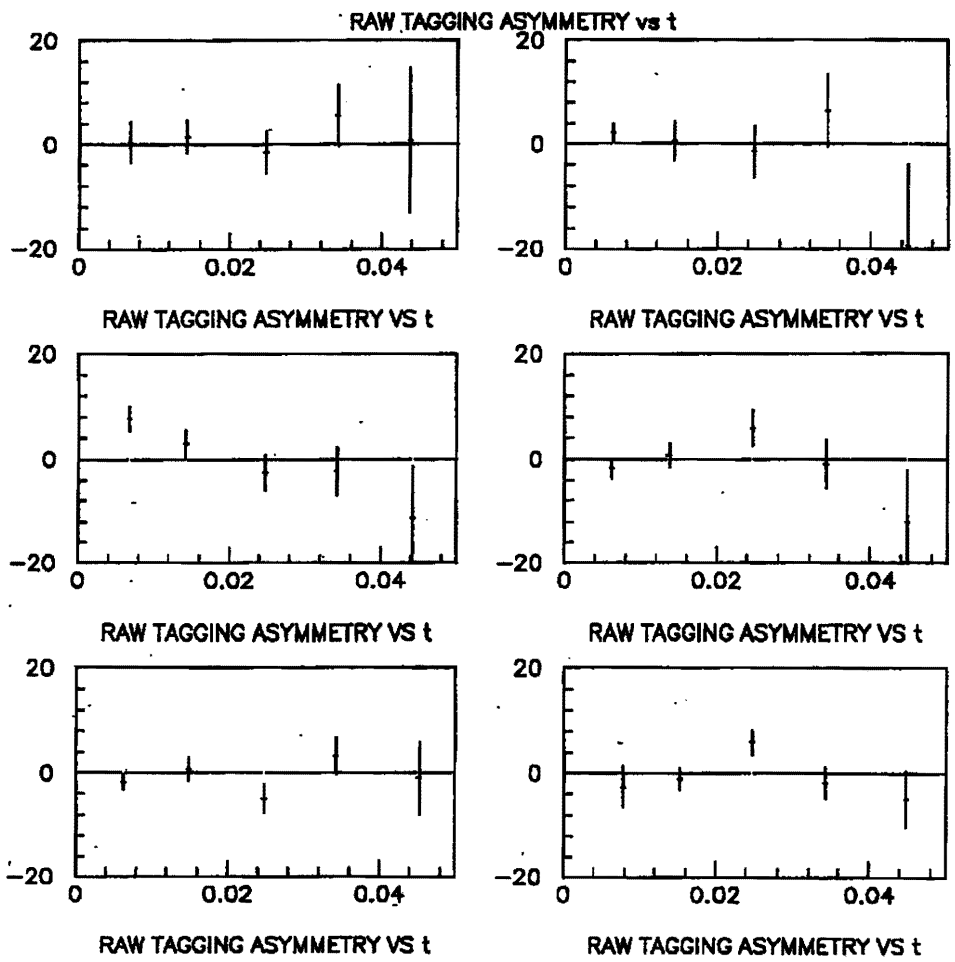

Figure 6.18 The raw *tagging* asymmetry for each target as a function of t.

REFERENCES

[Akch89] N. Akchurin et al., Phys. Lett. **29** (1989) 299-303.

[Akim65] Yu. K. Akimov, *Scintillation Counters in High Energy Physics*, Academic Press, New York, 1965.

[Algu76] M. J. Alguard et al., Phys. Rev. Lett. **37** (1976) 1261, ibid **41** (1978) 70.

[Anti80] J. Antille et al., Phys.Lett. **94B** (1980) 523.

[Apok89] V. D. Apokin et al., IHEP Serpukhov preprint 89-37, 1989.

[Arig85] M. Arignon et al., Nucl. Instr. Meth. **A235** (1985) 523-535. The hodoscope described here is a circular one, whereas the Gray Code Hodoscope used for CNI measurement has a rectangular geometry. The underlying principles of operations though are identical.

[Ashm88] J. Ashman et al., Phys. Lett. **206** (1988) 364.

[Azai83] H. Azaiez et al., *Miniturization of High Energy Physics Detectors*, Ed. A. Stefanini, p. 155, Plenum Publishing Co., 1983.

[Azai87] H. Azaiez, Ph.D. thesis, *Measures de Quelques Parameters de Spin aux Energies Intermediares dans les Regions D'Interference Coulomb- Nucleaire, 0 et 90 (cm)*, Universite Scientifique et Medical de Greonable.

[Barg57] V. Bargmann, L. Michel, V. L. Telegdi, Phys. Rev. Lett. **2** (1957) 435.

[Bark64] W. H. Barkas and M. J. Berger, *Tables of Energy Losses and Ranges of Heavy Charged Particles*, NASA SP-3013, 1964.

[Baum83] G. Baum et al., Phys. Rev. Lett. **51** (1983) 1135.

[Beth58] H. A. Bethe, Annal. Phys. **3** (1958) 190.

[Birk51] J. B. Birks, Proc. Phys. Soc. A64 (1951) 874.

[Birk54] J. B. Birks, Proc. Phys. Soc. B67 (1954) 657.

[Birk64] J. B. Birks, *The Theory and Practice of Scintillation Counting*, Pergamon Press, New York, 1964.

[Birs79] R. Birsa et al., INFN/AE-79/5.

[Blac53] F. A. Black, Phil. Mag. 44 (1953) 263.

[Boll61] L. M. Bollinger and G. E. Thomas, Rev. Sci. Instr. 32 (1961) 1044.

[Bonne88] B. E. Bonner et al., Phys. Rev. Lett. 61 (1988) 1918 .

[Broo74] F. D. Brooks and D. T. L. Jones, Nucl. Instr. Meth. 121 (1974) 69.

[Brow77] K. L. Brown et al., Stanford Linear Accelerator Center document SLAC-91, Rev.2, 1977; K. L. Brown et al., Fermi National Accelerator Laboratory document NAL-91, 1977; K. L. Brown et al., CERN Report 80-04, 1980.

[Butt78] N. H. Buttimore, E. Gotsman, E. Leader, Phys. Rev. D, 18, No.3 (1978).

[Care71] D. C. Carey, Fermi National Laboratory document NAL-64, 1971; D.C. Carey et al., Stanford Linear Accelerator document SLAC-246, 1982.

[Care90] D. C. Carey et al., Phys. Rev. Lett. 64 (1990) 4 .

[Chou52] C. N. Chou, Phys. Rev. 87 (1952) 904.

[Corc80] M. Corcoran et al., Phys. Rev. D 22 (1980) 2624

[Coon58] (unpublished) quoted by C. D. Swartz and G. Owen, *Fast Neutron Physics*, part I, eds. J. B. Marion and J. F. Fowler, Interscience, New York (1960) p.211.

[Crau70] R. L. Craun, D. L. Smith, Nucl. Inst. Meth. 80 (1970) 239-244.

[Cron63] J. W. Cronin and O. E. Overseth, Phys. Rev. 129 (1963) 1795.

[Dall89] S. Dalla Torre-Colautti et al., Nucl. Phys. A505 (1989) 561-582.

[Derb77] Ya. S. Derbenev and A. M. Kondratenko, 10th Int. Conf. on High Energy Accel., Vol 2, 70 (Protvino, 1977); Ya. S. Derbenev et al., Particle Accel. 8, (1978) 115.

[Faja80] L.-A. Fajardo-Paz, Ph.D. Thesis, Yale Univ. 1980

[Fide81] G. Fidecaro et al., Phys. Lett. B 105 (1981) 309.

[Garr56] A. Garren, Phys. Rev. 101 (1956) 419.

[Gros89] D. P. Grosnick, N. Akchurin et al., Nucl. Inst. Meth. A290 (1990) 269-292.

[Hirs48] J. O. Hirschfelder, J. L. Magee, Phys. Rev. 73 (1948) 207.

[Hosh68] N. Hoshizaki, Suppl. Prog. Theo. Phys. 42 (1968).

[Klem76] R. D. Klem et al., Phys.Rev. Lett. 36 (1976) 929.

[Klin80] R. V. Kline et al., Phys. Rev. D22 (1980) 553.

[Kope74] B. Z. Kopeliovich and L. I. Lapidus, Sov. J. Nucl. Phys., Vol.19, No.1 (1974).

[Kope89] B. Z. Kopeliovich and B. G. Zakharov, Phys. Lett. 226 (1989) 156-158.

[Kris89] A. D. Krisch et al., UICF Newsletter, No 45, (1989); A. D. Krisch et al., Phys. Rev. Lett. **63** (1989) 1137.

[Krol81] P. Kroll, Physics Data, **22** (1981) 1.

[Kuch68] F. T. Kuchnir and F. J. Lynch, IEEE Trans. Nucl. Sci. **NS-15** (1968) 107.

[Kuro79] K. Kuroda, A. Penzo, V. Solovianov, CERN, EP Internal Rep. 79-1.

[Kuro82] K. Kuroda, invited talk, The 5th International Symposium on High Energy Spin Physics, Brookhaven National Laboratory, Oct. 1982

[Loch67] M. P. Locher, Nucl. Phys. **B2** (1967) 525-531.

[Lueh90] F. Luehring, private communication.

[Mala83] E. Malamud et al., IEEE Trans. Nucl. Sci. **NS-30** (1983) 2775.

[Mora68] M. J. Moravcsik, *The Two-Nucleon Interaction*, Clarendon Press, Oxford, 1968.

[Nguv90] C. Nguyen, private communication.

[Over69] O. E. Overseth, in 1969 Summer Study - Particle Beams, (National Accelerator Laboratory, Batavia, 1969), Vol.1, p.19; O. E. Overseth and J. Sandweiss, ibid. Vol.1, p.27; P. Dalpiaz, J. A. Jansen, and G. Coignet, CERN/ECFA/72/4, Vol.1, 1972; S. Nurushev et al., High-Energy Physics with Polarized Beams and Polarized Targets, Lausanne, 1980, eds. C. Joseph and J. Soffer (Birkhauser Verlag, Basel, 1981).

[Penz78] A. Penzo, private communication and internal note.

[Prim51] H. Primakoff, Phys. Rev. **81** (1951) 899.

[Ratn76] L. G. Ratner, Czech. J. Phys. **B26** (1976) 34.

[Robe78] J. B. Roberts, AIP Conf. Proc. **42** (1978) 67.
[Ross 83] L. van Rossum, DPhPE 83-08 preprint (1983)
[Ross90] L. van Rossum, private communication.
[Schi79] A.M. Schiz, Ph.D. Thesis 1979, Yale Univ.
[Schw46] J. Schwinger, Phys. Rev. Vol.69 (1946) 681.

[Snyd78] J. H. Snyder et al., Phys. Rev. Lett. **41** (1978) 781.

[Solo66] L. D. Solov'ev, Sov. Phys. JETP, **22** (1966) 205.

[Stap 56] H. P. Stapp, Phys. Rev. Vol.**103**, No.2 (1956).

[Tayl51] C. J. Taylor et al., Phys. Rev. **63** (1951) 1034.
[Trox88] S.M. Troshin and N.E. Tyurin, Sov. J. Part. Nucl. 19 (1988) 429
[Unde80] D. G. Underwood, Nucl. Inst. Meth. **173** (1980) 351-355.

[West68] G. B. West and D. R. Yennie, Phys. Rev. Vol.**172**, No.5 (1968).

[Whal58] W. Whaling, *Handbuch der Physik*, **34**, Spring-Verlag, Berlin, 1958.

[Wolf56] L. Wolfenstein, Ann. Rev. Nucl. Sci. **6** (1956) 43.

[Wrig53] G. T. Wright, Phys. Rev. **91** (1953) 1282.

[Yoko80] A. Yokosawa, Phys. Rep. **64**, No.2 (1980) 47-86.

[Yosh88] T. Yoshida et al., 8th International High-Energy Spin Physics Symposium, ed. K. J. Heller, p.1360, Minnesota 1988.